

SYNTHESIS AND APPLICATION OF $Mg_xAlO_y-SiO_2$ CATALYSTS FOR THE
CONVERSION OF ETHANOL TO 1,3-BUTADIENE

Maynara Lurriele de Alcântara Santos

Tese de Doutorado apresentada ao Programa de Pós-graduação em Engenharia Química, COPPE, da Universidade Federal do Rio de Janeiro, como parte dos requisitos necessários à obtenção do título de Doutora em Engenharia Química.

Orientadores: Fabio Souza Toniolo
Henrique Poltronieri Pacheco

Rio de Janeiro

Abril de 2025

SYNTHESIS AND APPLICATION OF $Mg_xAlO_y-SiO_2$ CATALYSTS FOR THE
CONVERSION OF ETHANOL TO 1,3-BUTADIENE

Maynara Lurriele de Alcântara Santos

TESE SUBMETIDA AO CORPO DOCENTE DO INSTITUTO ALBERTO LUIZ
COIMBRA DE PÓS-GRADUAÇÃO E PESQUISA DE ENGENHARIA (COPPE) DA
UNIVERSIDADE FEDERAL DO RIO DE JANEIRO COMO PARTE DOS
REQUISITOS NECESSÁRIOS PARA A OBTENÇÃO DO GRAU DE DOUTOR EM
CIÊNCIAS EM ENGENHARIA QUÍMICA.

Examinada por:

Prof. Henrique Poltronieri Pacheco, D. Sc.

Prof. Fabio Souza Toniolo, D. Sc.

Michael P. Lanci, Ph.D.

Eugenio Furtado de Souza, D.Sc.

Prof. Christian Wittee Lopes, D.Sc.

RIO DE JANEIRO, RJ – BRASIL

ABRIL DE 2025

Santos, Maynara Lurriele de Alcântara Santos

Synthesis and Application of $Mg_xAlO_y-SiO_2$ Catalysts for the Conversion of Ethanol to 1,3-Butadiene/ Maynara Lurriele de Alcântara Santos. – Rio de Janeiro: UFRJ/COPPE, 2025.

XII, 119 p.: il.; 29,7 cm.

Orientadores: Fabio Souza Toniolo

Henrique Poltronieri Pacheco

Tese (doutorado) – UFRJ/ COPPE/ Programa de Engenharia Química, 2025.

Referências Bibliográficas: p. 105-119.

1. Etanol a 1,3-Butadieno. 2. Catálise Heterogênea. 3. Óxidos Mistos. I. Toniolo, Fabio Souza *et al.* II. Universidade Federal do Rio de Janeiro, COPPE, Programa de Engenharia Química. III. Título.

Acknowledgments

Este trabalho não teria sido possível sem a participação, o apoio e a colaboração de muitas pessoas e instituições, às quais sou profundamente grata.

À CAPES, pelo financiamento que viabilizou este projeto de doutorado.

Ao Programa de Engenharia Química da COPPE e à Universidade Federal do Rio de Janeiro, pelo suporte institucional e pelas instalações de pesquisa.

Aos meus orientadores, Dr. Fabio Toniolo e Dr. Henrique Pacheco, pelo acompanhamento, pelos questionamentos desafiadores, pelas horas de trabalho (às vezes, ao som de L'amour Toujours) e pela confiança depositada em mim.

Aos amigos do NUCAT, que estavam sempre tão engajados em deixar a rotina intensa dos trabalhos mais leve. Um agradecimento especial à Dora e ao Macarrão, que praticamente seguraram minha mão e mostraram os caminhos técnicos.

Aos amigos do Rio, pelo acolhimento e parceria no meu desbravamento da Cidade Maravilhosa e cada canto dela. Em especial, ao Mat, que esteve comigo desde o primeiro momento em que cheguei aqui (e antes disso, e depois disso).

Aos amigos de Maceió (e arredores), que, mesmo à distância, seguiram me revigorando com cada reencontro, com cada mensagem, com cada acolhida calorosa de cada retorno.

À minha família, pelo suporte incondicional em todas as formas possíveis. À minha mãe, especialmente, por suportar com coragem a distância, sem deixar de me apoiar.

A Deus, por sempre me guiar.

A todos que direta ou indiretamente contribuíram ou fizeram parte da realização deste trabalho – muito obrigada.

Toda compreensão súbita é finalmente a revelação de uma aguda incompreensão.

Clarisse Lispector

Resumo da Tese apresentada à COPPE/UFRJ como parte dos requisitos necessários para a obtenção do grau de Doutora em Ciências (D.Sc.)

SYNTHESIS AND APPLICATION OF $Mg_xAlO_y-SiO_2$ CATALYSTS FOR THE
CONVERSION OF ETHANOL TO 1,3-BUTADIENE

Maynara Lurriele de Alcântara Santos

Abril/2025

Orientadores: Fabio Souza Toniolo

Henrique Poltronieri Pacheco

Programa: Engenharia Química

A razão molar de Mg:Al:Si em uma série de catalisadores de óxidos mistos $Mg_xAlO_y-SiO_2$ demonstrou influência significativa na conversão de etanol a 1,3-butadieno, intermediário essencial na indústria de polímeros. Os materiais foram caracterizados quanto às propriedades estruturais, texturais, ácidas e básicas. Amostras selecionadas foram impregnadas com 0,1 de fração mássica de Ru ou Re para avaliar o efeito de promotores metálicos. Os resultados revelaram que a conversão do etanol e a distribuição de produtos estão intimamente relacionadas à densidade e à razão entre sítios básicos e ácidos. O catalisador com maior seletividade a BD (17,8%), MAS311, apresentou razão básica/ácida de 1,22. A adição de metais promoveu significativamente a seletividade a acetaldeído (38,7 % para o 0.1Ru/MAS311 e 7,8 % para o 0.1Re/MAS311), evidenciando maior atividade de desidrogenação; no entanto, a subsequente conversão a BD apresentou-se limitada pela reduzida densidade de sítios básicos ($1,82 \mu\text{mol m}^{-2}$ em MAS311 vs. $0,97 \mu\text{mol m}^{-2}$ e $0,69 \mu\text{mol m}^{-2}$ nos catalisadores com Ru e Re, respectivamente). Todos os catalisadores demonstraram elevada estabilidade estrutural e catalítica, confirmada por análise *operando* de DRX e testes prolongados de 72 h de reação. Os resultados evidenciam que, além da presença de sítios metálicos, o equilíbrio entre basicidade e acidez — com razão próxima à unidade — é determinante para a otimização da rota de valorização do etanol.

Abstract of Thesis presented to COPPE/UFRJ as a partial fulfillment of the requirements for the degree of Doctor of Science (D.Sc.)

SYNTHESIS AND APPLICATION OF $Mg_xAlO_y-SiO_2$ CATALYSTS FOR THE
CONVERSION OF ETHANOL TO 1,3-BUTADIENE

Maynara Lurriele de Alcântara Santos

April/2025

Advisors: Fabio Souza Toniolo

Henrique Poltronieri Pacheco

Department: Chemical Engineering

The molar ratio of Mg:Al:Si in a series of mixed oxide catalysts $Mg_xAlO_y-SiO_2$ showed a significant influence on the conversion of ethanol to 1,3-butadiene, a key intermediate in the polymer industry. The materials were characterized in terms of their structural, textural, acidic, and basic properties. Selected samples were impregnated with 0.1 mass fraction of Ru or Re to evaluate the effect of metallic promoters. The results revealed that ethanol conversion and product distribution are closely related to the density and the ratio of basic to acidic sites. The catalyst with the highest selectivity to BD (17.8 %), MAS311, exhibited a basic-to-acidic site ratio of 1.22. The addition of metals significantly promoted acetaldehyde selectivity (38.7 % for 0.1Ru/MAS311 and 7.8 % for 0.1Re/MAS311), indicating enhanced dehydrogenation activity; however, the subsequent conversion to BD remained limited by the reduced density of basic sites (1.82 $\mu\text{mol m}^{-2}$ in MAS311 vs. 0.97 $\mu\text{mol m}^{-2}$ and 0.69 $\mu\text{mol m}^{-2}$ in the Ru- and Re-containing catalysts, respectively). All catalysts exhibited high structural and catalytic stability, as confirmed by *operando* XRD analysis and extended 72-hour reaction tests. These findings highlight that, in addition to the presence of metallic sites, a well-balanced basic-to-acidic ratio—close to unity—is crucial for optimizing the ethanol valorization pathway.

Contents

Acknowledgments	iv
Contents	viii
List of Figures	x
List of Tables	xii
Introduction	1
1.1 Background and motivation.....	1
1.2 Objectives	4
1.3 Thesis outline.....	5
Literature Review	6
2.1 Ethanol upgrading.....	6
2.2 The role of 1,3-butadiene in decarbonization	12
2.3 From ethanol to 1,3-butadiene	16
2.3.1 Reaction mechanisms.....	16
2.3.2 Main catalysts	21
2.3.3 Dehydrogenating metals	32
Methodology	40
3.1 Catalyst synthesis.....	40
3.2 Catalyst characterization.....	43
3.2.1 X-ray Fluorescence (XRF).....	43
3.2.2 Inductively Coupled Plasma Optical Emission Spectroscopy (ICP-OES).....	44
3.2.3 X-ray Diffraction (XRD)	44
3.2.4 Thermogravimetric Analysis (TGA).....	45
3.2.5 N ₂ Physisorption	45
3.2.6 Temperature-Programmed Desorption (TPD)	45
3.2.7 Scanning Electron Microscopy (SEM)	46
3.2.8 Temperature-Programmed Reduction (TPR).....	46
3.2.9 Ultraviolet-Visible Diffuse Reflectance Spectroscopy (DRS UV-Vis)	47
3.2.10 X-ray Photoelectron Spectroscopy (XPS).....	47
3.3 Catalytic testing	48
Results and Discussion	50
4.1 Catalyst characterization.....	50
4.1.1 Chemical composition	50

4.1.2	Morphology and structure	52
4.1.3	Specific surface area	54
4.1.4	Crystallographic analysis	57
4.1.5	Surface acidity and basicity	66
4.1.6	Reduction profile	73
4.1.7	Electronic structure of metals	75
4.1.8	Surface chemistry analysis.....	77
4.2	Catalytic tests.....	80
4.2.1	Effect of reaction temperature on the performance of MAS111.....	80
4.2.2	Effect of the Mg:Al:Si ratio on catalytic performance.....	84
4.2.3	Effect of reaction temperature on the performance of MAS311.....	88
4.2.4	Catalytic Stability of MAS311.....	90
4.2.5	Effect of metal doping on catalytic performance of MAS311	91
	Conclusions	95
5.1	Suggestions for upcoming works.....	97
	Appendix	99
	References.....	105

List of Figures

Figure 1.1	Ethanol production over the last 10 years	2
Figure 2.1	Examples of products derived from ethanol	8
Figure 2.2	BioButterfly Project	11
Figure 2.3	Commonly accepted pathway for the conversion of ethanol to BD	18
Figure 2.4	Alcohol dehydrogenation	19
Figure 2.5	Ethanol dehydrogenation through ethoxide species formation on the surface	19
Figure 2.6	Aldol condensation for the formation of crotonaldehyde	20
Figure 2.7	Illustration of intensity of surface interactions between some metal groups and hydrogen	33
Figure 3.1	Domain diagram for $\text{Al}(\text{OH})_3$, $\text{Mg}(\text{OH})_2$, and hydrotalcite HT- NO_3 , with S on the y-axis defined as solubility	41
Figure 3.2	Influence of the thermal treatment temperature of hydrotalcites on the ethanol conversion reaction to higher value-added products	42
Figure 4.1	SEM images of the catalysts	52
Figure 4.2	Thermogravimetric curves and the first-derivatives of the corresponding plots	54
Figure 4.3	N_2 adsorption and desorption isotherms of the catalysts	56
Figure 4.4	N_2 physisorption cumulative pore size distribution results	57
Figure 4.5	X-ray diffractograms of the catalysts	58
Figure 4.6	X-ray diffractograms of one of the samples prior to the thermal treatment showing peaks of hydrotalcite (JCPDS 14-0191)	59
Figure 4.7	Simplified representation of the rehydration of Mg–Al oxides	59
Figure 4.8	<i>In situ</i> and <i>operando</i> XRD of the samples	61
Figure 4.9	Initial (black line) and final (red line) XRD spectra of the samples	63
Figure 4.10	Desorption profiles of a) CO_2 and b) NH_3 for catalysts pretreated at 773 K	67

Figure 4.11	Desorption profiles of a) CO ₂ and b) NH ₃ for catalysts pretreated at 623 K	67
Figure 4.12	Desorption profiles of a) CO ₂ and b) NH ₃ for 0.1Ru/MAS311 and 0.1Re/MAS311	70
Figure 4.13	Acid and basic sites density and correlation between them	71
Figure 4.14	TPR results for the metal-containing catalysts	74
Figure 4.15	UV-Vis spectra of a) 0.1Ru/MAS311 and b) 0.1Re/MAS311 catalysts	76
Figure 4.16	XPS complete spectrum range for 0.1Ru/MAS311 and 0.1Re/MAS311	78
Figure 4.17	XPS spectra of the O 1s region for 0.1Ru/MAS311 and 0.1Re/MAS311	79
Figure 4.18	Linear correlation between ethanol conversion and reactor space time demonstrates kinetic regime	81
Figure 4.19	Ethanol conversion and product distribution of MAS111 at different temperatures	81
Figure 4.20	Product selectivity as a function of ethanol conversion	83
Figure 4.21	Ethanol conversion and product distribution at 723 K	84
Figure 4.22	Proposed mechanism for the aldol condensation of AcH	85
Figure 4.23	Conversion and product distribution for the MAS113 catalyst	86
Figure 4.24	Correlation between product distribution and the acidity and basicity of the unsupported catalysts.....	88
Figure 4.25	Ethanol conversion and product selectivity for MAS311 at different temperatures	89
Figure 4.26	Stability test for MAS311 at 723 K	90
Figure 4.27	Ethanol conversion and product distribution of unsupported MAS311 and Ru- and Re-doped	91
Figure 4.28	Stability test for a) 0.1Ru/MAS311 and b) 0.1Re/MAS311 at 673 K	93

List of Tables

Table 2.1	Catalysts applied in the conversion of ethanol to 1,3-butadiene	30
Table 3.1	Reagents used in the catalyst synthesis	41
Table 4.1	Chemical composition of catalysts <i>via</i> XRF, EDS, and ICP analysis	51
Table 4.2	Quantification of acid and basic sites by NH ₃ - and CO ₂ -TPD	71
Table 4.3	XPS quantitative analysis (atomic %) for the elements	78
Table A.1	Ethanol conversion values (%) and product selectivity (%) for the MAS111 catalyst at different temperatures	100
Table A.2	Ethanol conversion values (%) and product selectivity (%) for all un-doped catalysts	101
Table A.3	Ethanol conversion values (%) and product selectivity (%) for the MAS311 catalyst at different temperatures	102
Table A.4	Ethanol conversion values (%) and product selectivity (%) for the metal-doped catalysts	103

Chapter 1

Introduction

1.1 Background and motivation

Ethanol production on an industrial scale initially aligned with the expansion of the automotive industry in the 1920s and found widespread application during the oil shortages of World War II. However, it was not until the late 20th century that ethanol achieved substantial prominence within the Brazilian industrial landscape. In the 1973 oil crisis, oil-producing countries in the Middle East imposed an embargo, causing global oil prices to quadruple in just a few months (BATISTA, 2024). In response, Brazil began investing heavily in biofuel production and infrastructure to reduce its dependency on imported oil and the associated instability of that period. In 1975, the Brazilian government launched the Proálcool program, which mandated the addition of ethanol to gasoline at fixed minimum concentrations, thereby lowering fuel costs for consumers. This program also included guarantees for state-owned Petrobras to purchase ethanol, as well as low-interest loans for bioethanol producers and fixed ethanol prices. Following the second oil crisis in 1979, the Brazilian automotive industry began manufacturing cars powered entirely by ethanol, later introducing flex-fuel vehicles that allow consumers to use various blends of gasoline and ethanol (ZANCANER; WRIGHT, 2020). This represents a significant development, as 33 % of Brazil's total energy consumption in 2023 was allocated to the transportation sector (EMPRESA DE PESQUISA ENERGÉTICA, 2024). Today, Brazil is one of the world's largest producers and consumers of ethanol, trailing only the United States in production and ranking third, behind the U.S. and Germany, in consumption. Together, Brazil and the United States account for approximately 80 % of global ethanol production in recent years. In 2024, Brazil produced 8.78 billion gallons of ethanol (RENEWABLE FUELS ASSOCIATION, 2024). Despite a drop in production in 2020 due to the COVID-19 pandemic (Figure 1.1), the recovery has been faster than initially anticipated.

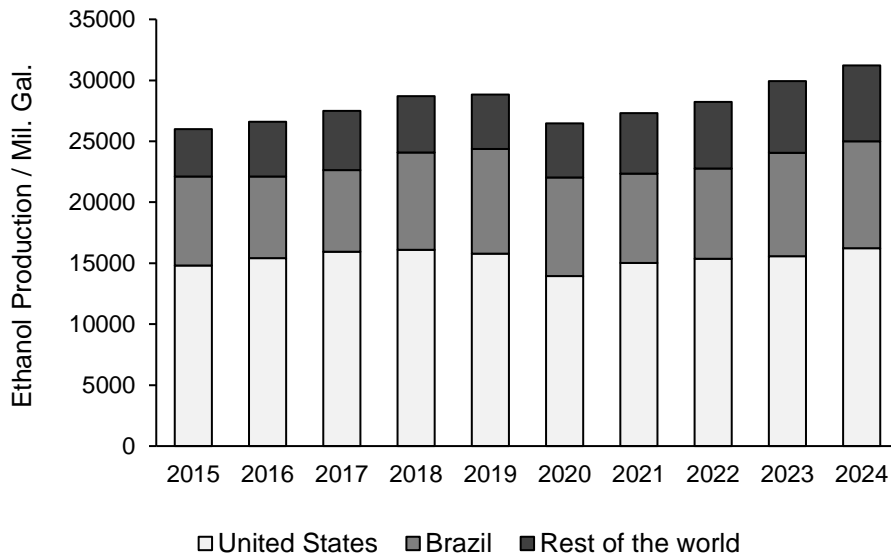


Figure 1.1 – Ethanol production over the last 10 years.

Conversely, the global growth of the electric vehicle industry could pose a significant challenge to the expansion of ethanol production, particularly by directly affecting market demand. Factors such as the increasing demand for low-emission transportation and government incentives for long-range, zero-emission vehicles, through subsidies and tax reductions, are prompting manufacturers to ramp up electric vehicle production worldwide. Global electric vehicle sales were 3.5 million higher in 2023 than 2022, representing a 35 % year-on-year growth, which resulted in nearly 14 million new electric vehicles being registered worldwide, bringing the total number of electric vehicles in operation to approximately 40 million (INTERNATIONAL ENERGY AGENCY, 2024b). Solely in Brazil, a record of more than 177,000 electrified vehicles were registered in 2024, surpassing the projected 160,000 units and representing an 89 % increase compared to the approximately 94,000 units reported in 2023 (ASSOCIAÇÃO BRASILEIRA DO VEÍCULO ELÉTRICO, 2025). This market, valued at approximately USD 578.71 billion in 2024, is projected to reach US\$ 2071.02 billion by 2032 (PALWE, 2024). This transition presents a challenge for the Brazilian ethanol industry, which is heavily reliant on ethanol consumption as fuel. According to projections by the Energy Research Company (EPE) for 2025, ethanol production is expected to reach 36.4 billion liters, while fuel demand—encompassing both hydrous and anhydrous ethanol—is anticipated to total 34.8 billion liters, underscoring the industry's strong dependence on the fuel sector (EMPRESA DE PESQUISA ENERGÉTICA, 2025a; 2025b).

Consequently, this shift urges the industry to find solutions to avoid potential surpluses due to changing dynamics in the automotive industry.

One potential solution under discussion is the conversion of ethanol into higher products. Ethanol can be transformed into various products, including gaseous hydrogen, methane, ethylene, propylene, 1,3-butadiene (BD), acetaldehyde (AcH), diethyl ether (DEE), 1-butanol (BuOH), acetone, ethyl acetate, and several aromatic compounds, among others. Due to this versatility, ethanol is considered a chemical platform, meaning that a wide range of products can be synthesized from it (RIITTONEN *et al.*, 2012). One of the primary products of interest in ethanol conversion is BD, a monomer mainly used in the production of synthetic rubbers and elastomers, including polybutadiene, styrene-butadiene rubber, nitrile rubber, and polychloroprene. Another important use of BD is its conversion into adiponitrile, a precursor for nylon-6,6 production (WHITE, 2007; SUN *et al.*, 2020). In 2023, the global market for BD was estimated to be worth around USD 40 billion, with forecasts predicting a compound annual growth rate (CAGR) of around 7 % over the coming decade (GRAND VIEW RESEARCH, 2023). However, since more than 95 % of BD is currently produced as a byproduct of ethylene production *via* steam cracking, its production is vulnerable to market fluctuations or trends in the oil industry, which could lead to shortages (EZINKWO *et al.*, 2014). Moreover, BD produced from ethanol derived from biomass would align with current industry trends favoring alternative and renewable resources. The CO₂ captured from the atmosphere during the growth of the raw material used to produce ethanol, predominantly sugarcane in Brazil (which comprises nearly 17 % of the total energy supply in Brazil in 2023 (EMPRESA DE PESQUISA ENERGÉTICA, 2024), combined with emerging bioenergy technologies in ethanol plants, including carbon capture and storage, contribute to decarbonization efforts and strengthen this sustainable BD production pathway (RESTREPO-VALENCIA; WALTER, 2019). These factors have recently rekindled longstanding interest in the heterogeneous catalytic conversion of ethanol into BD.

To make this promising process viable, the academic community is encouraged to conduct in-depth studies on the systems enabling this conversion and to identify catalysts that optimize performance. A key characteristic of the catalyst used in the ethanol-to-BD conversion is its acid-base properties: the quantity and strength of these sites directly influence the reaction's selectivity, as acid sites are crucial for dehydration and base sites for dehydrogenation, both essential steps in the process. To optimize the catalytic process,

it is vital to design the catalyst in a way that enhances activity, particularly for the rate-determining step—the dehydrogenation of ethanol to AcH. This can be achieved by incorporating metals that provide efficient dehydrogenation sites. The literature highlights a variety of bulk and, more commonly, supported catalysts with a broad range of active metals. Despite this progress, several gaps remain. Disagreements persist regarding the reaction mechanism; the lack of reliable techniques for material characterization, especially in *operando* conditions, complicates the detection of specific reaction intermediates; the presence of multiple concurrent reactions makes it difficult to study isolated reactions; and the extensive combinations of support/active phase still offer much unexplored potential.

1.2 Objectives

Within this framework, the primary purpose of this research is to synthesize and characterize Mg, Al, and Si oxide-based catalysts doped with Ru and Re metals, with the goal of evaluating their activity in the conversion of ethanol to 1,3-butadiene and other higher products. To achieve this overarching aim, the study is divided into the following specific objectives:

- To synthesize Mg, Al, and Si oxide catalysts *via* coprecipitation;
- To impregnate 0.1 % mass fraction of Ru or Re onto the previously synthesized oxides using the incipient wetness impregnation method;
- To characterize the catalysts, both pre- and post-impregnation, regarding their physicochemical properties: chemical composition by ICP-OES, XRF; phase identification and possible structure changes by *in situ* and *operando* XRD; textural property evaluation, including specific surface area, pore volume, and average pore diameter, through N₂ physisorption; qualification and quantification of acidic and basic sites through NH₃- and CO₂-TPD; metal reducibility profile *via* H₂-TPR; oxidation states of metals and investigate electronic transitions by UV-Vis spectroscopy; active phase analysis on the support materials using XPS;
- To conduct catalytic performance evaluation in a reaction setup to investigate the influence of catalyst properties on ethanol conversion and product selectivity,

especially 1,3-butadiene, and catalyst stability by monitoring deactivation behavior over extended reaction times.

1.3 Thesis outline

Following this Introduction, the thesis is structured into five main chapters, each addressing a critical aspect of the study. Chapter 2 delves into a comprehensive analysis of the reaction mechanisms underlying the conversion of ethanol to BD, highlighting the challenges and recent advancements in this catalytic transformation. It provides a critical overview of state-of-the-art catalysts reported in the literature. Chapter 3 details the experimental methodologies employed to achieve the research objectives, emphasizing on the systematic procedures developed for catalyst synthesis and characterization, as well as their subsequent application in the ethanol-to-BD reaction. Chapter 4 presents a discussion of the results obtained, offering insights into their implications. The chapter not only interprets the experimental data but also explores the relationship between catalyst properties, ethanol conversion, and product selectivity, offering valuable insights into the design and optimization of catalytic systems. Finally, Chapter 5 concludes the thesis by summarizing the key findings and drawing meaningful conclusions from the research. Additionally, this chapter proposes recommendations for future studies, identifying unexplored areas and opportunities for further advancements in the field of ethanol and catalyst development.

Chapter 2

Literature Review

2.1 Ethanol upgrading

In the quest for a more sustainable society, the gradual transition from petroleum-derived products to biomass-based alternatives for the production of chemicals and fuels is imperative. While both the combustion of fossil fuels and biomass-derived fuels emit carbon dioxide (CO₂), a major greenhouse gas, plants—the primary source of biomass for energy—may capture comparable amounts of CO₂ during their growth through photosynthesis. This dynamic place biomass as a potentially carbon-neutral energy source, although it is important to acknowledge that energy inputs are required for the cultivation, fertilization, and harvesting of raw materials (MORI, 2023; ENERGY INFORMATION ADMINISTRATION, 2025). To surpass fossil resources, the bioeconomy must demonstrate competitiveness with the modern petrochemical industry, which produces a wide variety of products—including plastics, surfactants, pharmaceuticals, and agrochemicals—using simple, biorenewable, and readily available chemical feedstocks. Traditionally, the petrochemical refinery has been the primary source of fuels and essential chemical feedstocks, but it currently faces several challenges, including increasing global demand, the high costs of recovery and refining, and highly volatile prices. Furthermore, fuels derived from petrochemical refineries are associated with significant adverse environmental impacts (CLEWS, 2016). Recent research efforts have increasingly focused on demonstrating the bioeconomy's potential to produce an equally diverse range of products from simple, cost-effective biomass-derived chemicals, which serve as foundational building blocks for the synthesis of more complex products (FARMER; MASCAL, 2015; LIE *et al.*, 2019; MASCAL, 2019). The development of advanced biorefineries is critical to achieving this vision. Comparative assessments of emerging biorefineries with established and highly optimized petrochemical plants and traditional refineries are essential for accelerating the integration of biorefineries as viable

technological and economic units. For instance, the aviation industry efforts have increasingly prioritized the development of integrated technologies that combine multiple production pathways for the synthesis of jet biofuel from biomass (KUMAR; LONG; SINGH, 2018; NG; FAROOQ; YANG, 2021; SADHUKHAN; SEN, 2021; ALHERBAWI; MCKAY; AL-ANSARI, 2023). In addition to their environmental advantages, these facilities offer significant social benefits (NAVA, 2021).

Ethanol is a versatile compound capable of serving as a platform molecule for the production of a wide array of economically and industrially significant products. Green ethanol offers distinct advantages over other biomass feedstocks, such as lignin, cellulose, hemicellulose, and fatty acids, due to its ability to be directly converted into drop-in chemicals. This capability allows ethanol to serve as a precursor for various petrochemical-derived compounds, including BD, ethylene, propylene, and higher hydrocarbons (GALLO; BUENO; SCHUCHARDT, 2014; HAÁZ *et al.*, 2018). These and other products that can be obtained from ethanol are illustrated in Figure 2.1. Although ethanol is widely used as a fuel, it shows limitations compared to higher alcohols, which offer superior properties such as higher energy density, lower volatility, and reduced corrosiveness (HARVEY; MERRIMAN; QUINTANA, 2016; EMIROĞLU; ŞEN, 2018). As a result, the synthesis of higher alcohols *via* the direct upgrading of ethanol through C–C coupling reactions has emerged as a promising renewable pathway. Furthermore, new opportunities are arising in the aviation sector, particularly through ethanol’s application as a sustainable aviation fuel (SAF). The production of long-chain hydrocarbons from fermentation-derived ethanol represents a viable strategy for generating fuel mixtures suitable for use as SAF. This process involves several key reaction steps, including the alkylation of ketones with organic alcohols, successive alcohol condensations *via* the Guerbet reaction, ketone oligomerization, and hydrodeoxygenation of the resulting products (WEI; SHAO; WANG, 2019; DOMÉNECH *et al.*, 2022; BARDON; MASSOL, 2025). Substantial investments are currently being directed toward the development of ethanol-to-jet fuel processing facilities. In 2024, SAF production volumes reached 1 million tonnes (1.3 billion liters), doubling the 0.5 million tonnes (600 million liters) produced in the previous year, according to the International Air Transport Association (IATA). However, this figure falls significantly short of earlier projections, which anticipated SAF production in 2024 to reach 1.5 million tonnes (1.9 billion liters). The outlook for 2025 is still optimistic:

SAF production is expected to increase to 2.1 million tonnes (2.7 billion liters), accounting for approximately 0.7 % of total global jet fuel production and represent 13 % of worldwide renewable fuel capacity, signaling a gradual yet significant advancement in the integration of SAF into the aviation fuel market (INTERNATIONAL AIR TRANSPORT ASSOCIATION, 2024). Moreover, this growth highlights the pivotal role of ethanol as a foundational resource for sustainable chemical and fuel production, offering a pathway to reduce dependence on petroleum-based resources while aligning with international sustainability objectives.

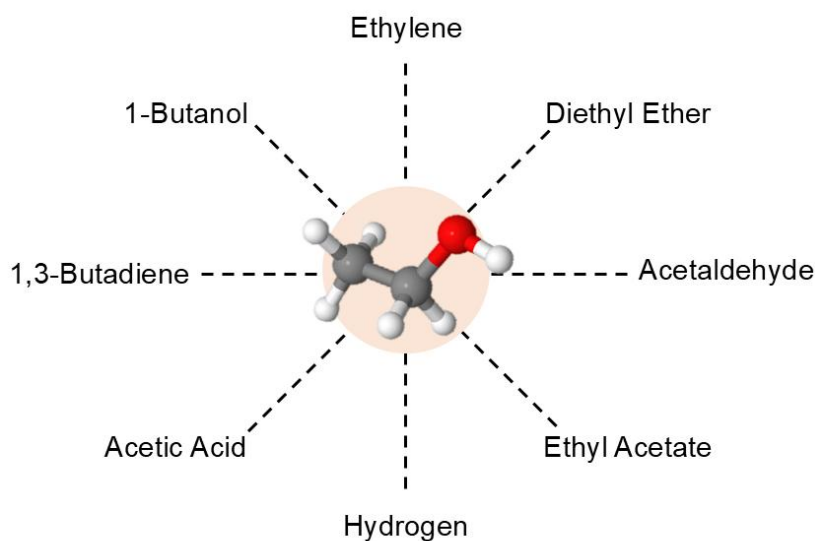


Figure 2.1 – Examples of products derived from ethanol.

Ethylene is a key precursor widely used in the production of polymers and other chemicals. Its production from ethanol offers a sustainable alternative to the conventional steam cracking of hydrocarbons from fossil feedstocks (FAN; DAI; WU, 2012). The feedstocks used in steam cracking vary from light alkanes to more complex mixtures, such as naphtha derived from crude oil. The process operates under high temperatures of around 1073 K, making it highly energy-intensive and a significant source of greenhouse gas emissions (GHOLAMI *et al.*, 2021; ROYLE *et al.*, 2024). The alternative ethylene production from ethanol has gained significant attention for several years now, being successfully implemented on an industrial scale by Braskem, a Brazilian petrochemical company with global operations. Since 2010, Braskem has utilized sugarcane-derived ethanol to produce renewable ethylene. Recently, the company allocated USD 87 million to expand its "green plastic" production facilities. This initiative represents an important step forward in the company's strategy to increase biopolymer production to 1 million

tonnes by 2030 and achieve carbon neutrality by 2050, highlighting the increasing societal and market demand for sustainable solutions (BRASKEM, 2023). The dehydration of ethanol to ethylene has been extensively studied, with acidic catalysts such as zeolites (TAKAHARA *et al.*, 2005; MASIH *et al.*, 2019; OUAYLOUL *et al.*, 2024) and aluminas (CHRISTIANSEN; MPOURMPAKIS; VLACHOS, 2013; WANG *et al.*, 2022b; HONG; GEBRESILLASE; SEO, 2024; ZHOU *et al.*, 2025) frequently employed in this reaction.

Regarding hydrogen production, petrochemical pathways remain economically favorable, even with advancements in water electrolysis and other emerging methods (BARRETO; MAKIHIRA; RIAHI, 2003; YU *et al.*, 2021). The petrochemical routes include partial oxidation of hydrocarbon fuels (primarily natural gas), steam reforming, dry reforming, thermal reforming, decomposition reactions, and coal gasification. Among these, steam methane reforming (SMR) is widely established as the most economically viable process for commercial hydrogen production (EWAN; ALLEN, 2005; MIYAMOTO *et al.*, 2011; HOSSAIN BHUIYAN; SIDDIQUE, 2025). Hydrogen is currently primarily applied in industrial processes for commercial chemical production, hydrocracking, and hydrotreating in refineries. However, future applications are largely focused on replacing conventional energy sources in transportation (ET ENERGYWORLD, 2021). Due to its potential as a clean fuel for the future, the production of green hydrogen through ethanol steam reforming has garnered significant attention (NI; LEUNG; LEUNG, 2007; OGO; SEKINE, 2020). Nickel, Co, and Cu are regarded as the most effective non-noble metal catalysts, with Ni being the most commonly used active metal due to its abundant availability and low cost (DAL SANTO *et al.*, 2012; OGO; SEKINE, 2020). A range of Ni-based catalysts supported on various inorganic oxides, including alumina, ceria, zirconia, and titania, has been extensively studied (PALMA *et al.*, 2014; TAHIR *et al.*, 2017; CHARISIOU *et al.*, 2019; SHTYKA *et al.*, 2021; XIAO *et al.*, 2021).

Butanol (BuOH) is a chemical commodity widely used as a solvent and in the production of several esters and ethers. It is also well recognized as advanced fuel, offering advantages over ethanol, such as higher calorific value (26.7 MJ/L), greater viscosity, lower hygroscopicity, and reduced corrosivity, which make it more suitable for pipeline distribution (SHANG *et al.*, 2019; ZHANG; SUN; YUAN, 2022). Traditionally, sustainable BuOH is produced through the ABE (Acetone-Butanol-Ethanol) fermentation

process from biomass-derived sugars. However, this method is associated with some disadvantages, including low BuOH yield and the formation of byproducts like acetone and ethanol. In contrast, its direct production *via* aldol condensation of ethanol over metal oxide and hydroxyapatite-derived catalysts is being explored as a promising alternative (KOZLOWSKI; DAVIS, 2013a; HO; SHYLES; BELL, 2016; YOUNG; HANSPAL; DAVIS, 2016; DIBENEDETTO; JONES, 2021; KIANI; BALTRUSAITIS, 2021).

Butadiene (BD) is one of the most important chemicals in the petrochemical industry. As reported by leading industry analysts (GRAND VIEW RESEARCH, 2023; TRANSPARENCY MARKET RESEARCH, 2024), the global market for BD was valued at approximately USD 40 billion in 2023, with projections indicating a compound annual growth rate (CAGR) of between 6 % and 7 % over the next decade. The primary driver behind this growth is the anticipated expansion of the global automotive industry in the coming years. BD plays a key role in the production of polymers and polymer intermediates, such as polybutadiene and styrene-butadiene, which are widely used in manufacturing rubber and plastics (BIN SAMSUDIN *et al.*, 2020). These materials have applications in the automotive sector, construction materials, electronics, and household appliance components. Furthermore, the global transition toward vehicle electrification is accelerating the demand for lightweight and fuel-efficient solutions, thereby driving the need for high-performance plastics and elastomers. As automotive manufacturers aim to comply with stringent environmental regulations and address consumer expectations for enhanced fuel efficiency, the outlook for the synthetic rubber market remains promising, supported by stable growth in global automobile production. This trend underscores the sustained demand for BD, a critical precursor for producing these advanced materials (GRAND VIEW RESEARCH, 2023; EHTAIBA; DOBASHI; GRAY, 2024). Currently, BD production relies on two primary methods. Approximately 97 % of global production is derived from the isolation of BD from hydrocarbon fractions generated during the steam cracking of paraffinic naphtha—a highly endothermic pyrolysis process conducted in the presence of steam and primarily intended for the production of ethylene and its higher homologs (SUN *et al.*, 2020; LI *et al.*, 2025). The second method involves the catalytic and oxidative dehydrogenation of n-butane and n-butenes, utilizing feedstocks sourced from petroleum (DAHLMANN; GRUB; LÖSER, 2011).

Although the production of BD *via* ethanol has been explored since the early stages of industrial interest in the compound—especially when Lebedev, in 1910, discovered its potential to form rubber-like polymers (LEBEDEV, 1910)—this route fell out of favor with the advent of cost-effective petroleum-based production following World War II. In recent years, however, there has been renewed interest from both industry and academia in ethanol-to-BD conversion, driven by its environmental, political, and economic significance. From an environmental perspective, a notable example is the launch of the BioButterfly project in 2012 (Figure 2.2) by Michelin, one of the world’s leading tire manufacturers, in collaboration with the research institute IFP Energies Nouvelles (IFPEN) and the energy sector group Axens. This initiative developed a new technology for producing bio-based BD from ethanol at a pilot scale. By 2024, Michelin, IFPEN and Axens had successfully inaugurated the first industrial-scale demonstrator of a plant producing bio-based BD in France. This facility is designed to validate each stage of the bio-based BD manufacturing process, demonstrating both its technological feasibility and economic viability. With a production capacity ranging from 20 to 30 metric tons per year, the demonstrator serves as a critical step toward the global commercialization of this innovative process (AXENS, 2024).

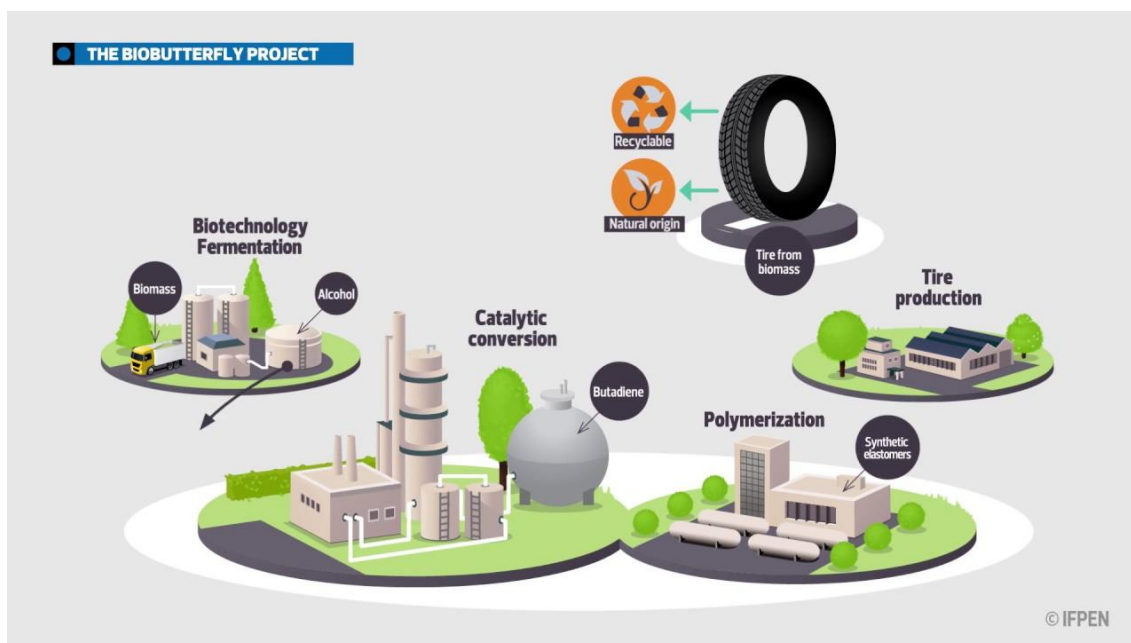


Figure 2.2 – BioButterfly Project (IFP ENERGIES NOUVELLES, 2019).

The growing focus on renewable and alternative resources for fuels and chemicals has created strong incentives to adopt bio-based monomers. These include governmental incentives, emerging fiscal policies, and strategic political initiatives aimed at enhancing

global market competitiveness and achieving energy independence (MAKSHINA *et al.*, 2012). In Brazil, the government has a long history of promoting biofuel production, particularly sugarcane ethanol. This began in 1975 with the launch of the National Alcohol Program (Proálcool), designed to address geopolitical challenges and reduce reliance on imported oil (BENITES-LAZARO; MELLO-THÉRY; LAHSEN, 2017). More recently, Brazil developed the National Biofuels Policy (RenovaBio), following its ratification of the Paris Agreement in 2016. This policy commits the country to increasing the share of biofuels in its energy matrix and aims to reduce greenhouse gas emissions by 37 % from 2005 levels by 2025, and by 43 % by 2030 (MINISTÉRIO DE MINAS E ENERGIA, 2017). Since its establishment, the program has been regularly monitored and updated, as demonstrated by the recent amendment to federal legislation expanding participation in the revenue from decarbonization credit trading to include independent producers of raw materials for biofuel production, a privilege previously limited to ethanol-producing plants. This amendment reinforces the commitment to meeting the established objectives for sustainable development (MINISTÉRIO DE MINAS E ENERGIA, 2024).

Meanwhile, advances in steam cracking technology have shifted operations toward shale gas as a feedstock, which has become economically advantageous. However, this shift has reduced BD production from these processes (ANGELICI; WECKHUYSSEN; BRUIJNINCX, 2013; RODGERS *et al.*, 2022). At the same time, the development and application of methanol-to-olefin (MTO) technology, which produces ethylene and propylene from methanol, further limits BD output (TIAN *et al.*, 2015). These industry transformations are expected to lead to a decline in global BD production, increasing its cost and spurring the pursuit of alternative production pathways.

2.2 The role of 1,3-butadiene in decarbonization

According to the International Energy Agency, the chemical industry currently accounts for 7 % of human-induced greenhouse gas emissions and 30 % of total industrial energy consumption (INTERNATIONAL ENERGY AGENCY, 2024a). However, the carbon content of many chemical products ties the industry to the use of carbon-based feedstocks, presenting a significant challenge for decarbonization. One effective strategy

to reduce emissions is the replacement of conventional fossil-based feedstocks with renewable carbon sources.

Ethanol is one of the most widely used renewable products, primarily produced from crops such as sugarcane and corn. Sugarcane-derived ethanol is considered sustainable because it can offset up to 86 % of CO₂ emissions compared to petroleum-based products, and the emissions resulting from land-use changes for sugarcane cultivation can be neutralized within just 2 to 8 years (MELLO *et al.*, 2014). Ethanol produced from sugarcane fermentation is estimated to be even more sustainable than corn-derived ethanol, with the emission ratio of corn-based ethanol to sugarcane-based ethanol being 3.3 g of CO₂ equivalent per MJ of ethanol (PEREIRA *et al.*, 2019). However, there are still several factors that must be considered when evaluating the overall emissions balance. Substantial amounts of fossil fuel inputs are required for plant cultivation, transportation, and ethanol distribution. Additionally, fertilizers, herbicides, and pesticides contribute net CO₂ emissions due to their production, distribution, and application (OLIVEIRA, 2008; LISBOA *et al.*, 2011). Life Cycle Assessment (LCA) is a tool used to evaluate the environmental impacts of a product, process, or activity by identifying and quantifying the energy and material flows involved, as well as the waste and emissions released throughout the process. This methodology has become the standard for estimating the greenhouse gas emissions over the life cycle of biofuels (MENDIBURU *et al.*, 2022). The LCA of ethanol is influenced by various factors, including agricultural practices such as the use of fertilizers, fuels, and agrochemicals that emit N₂O and other gases, as well as land-use changes. Emissions from transport also play a significant role, as the fuel used to transport biomass contributes to overall emissions. Lastly, the ethanol production plant itself consumes chemicals, energy, and fuels, further impacting the emissions profile (PEREIRA *et al.*, 2019).

When all emissions associated with the production and use of gasoline are considered, the fuel typically exhibits a carbon intensity of 94 g of CO₂ equivalent per MJ of energy provided, according to LCA. In comparison, corn and sugarcane ethanol have carbon intensities of 52 and 17.3 g of CO₂ equivalent per MJ, respectively (PEREIRA *et al.*, 2019; CAI; WANG, 2021; COOPER, 2022). When evaluating the LCA of Brazilian sugarcane ethanol, several unique factors must be considered. For instance, nitrogen-rich vinasse and filter cake are recycled, reducing reliance on synthetic nitrogen fertilizers and associated emissions. Historically, sugarcane straw was burned during

harvest, releasing embedded biogenic carbon as CO₂ and black carbon, a potent climate forcer. However, this practice is being replaced by mechanical harvesting, leaving straw in the field, which can be repurposed as cellulosic feedstock for ethanol production (CAI; WANG, 2021). These values of LCA demonstrate that ethanol use significantly reduces CO₂ emissions when compared to gasoline, both in terms of fuel consumption and during production, as a portion of these emissions is sequestered and reabsorbed during the growth of sugarcane (OLIVEIRA, 2008). Furthermore, new technologies are being developed and implemented in sugarcane mills for bioenergy generation that incorporate carbon capture and storage, capturing carbon from both the fermentation process and biomass combustion. When combined with the CO₂ absorbed from the atmosphere during the growth of the feedstock, bioenergy with carbon capture and storage has the potential to result in negative absolute emissions (KEMPER, 2015; RESTREPO-VALENCIA; WALTER, 2019).

The numerous benefits of ethanol make it a promising feedstock for the sustainable production of BD. Unlike other emerging renewable feedstocks, ethanol is already a significant global commodity. Thanks to government incentives promoting biofuels, the global supply of ethanol is already on an industrial scale (POMALAZA *et al.*, 2020). Studies examining the environmental impact of ethanol conversion to BD suggest that the process can be highly advantageous when optimal conditions are applied. Cavani and colleagues have reported that Brazilian sugarcane ethanol is more environmentally favorable than U.S. corn ethanol or ethanol produced in Europe from various sources (CESPI *et al.*, 2016). The Brazilian process also demonstrated clear advantages in reducing greenhouse gas emissions. Moreover, it was found that the one-step process, known as the Lebedev process, is less environmentally damaging than naphtha cracking and even the two-step ethanol conversion process, known as the Ostromislensky process (*vide* section 2.3).

Several factors must be carefully analyzed to effectively minimize the environmental impact of BD production from ethanol. However, under optimal conditions, this process holds significant potential for producing a sustainable product. Indeed, ongoing and increasing investment from the industry is driving the development of strategies to further enhance the sustainability of the process. In 2021, Synthos, a global leader in synthetic rubber development and production, partnered with Lummus Technology, a technology company, to explore and commercialize ethanol-derived BD.

This collaboration aims to facilitate the production of more sustainable and value-added synthetic rubber. In response to strong market demand for renewable materials, Synthos committed to building a plant with an annual capacity of 40,000 metric tons of BD—double the original planned capacity (LUMMUS TECHNOLOGY, 2022). Another major company recently moving in this same direction is Bridgestone, which, in late 2024, received a grant from the U.S. Department of Energy (DOE) Industrial Efficiency and Decarbonization Office that supports the design, construction, and operation of a pilot plant aimed at evaluating the economic and commercial feasibility of converting ethanol to BD using a catalytic system originally developed by Pacific Northwest National Laboratory (PNNL) (BRIDGESTONE AMERICAS, 2024).

It is worth noting that the ethanol-to-BD process presents several challenges, particularly in terms of economic viability, catalyst selectivity and stability, and overall process efficiency. A recent study by Cabreba Camacho *et al.* concluded that ethanol-derived BD is not economically competitive compared to naphtha-derived BD, with the probability of achieving a positive net present value (NPV) ranging from 11 % to 17 % for one-step processes and only 5 % for two-step processes (CABRERA CAMACHO *et al.*, 2022). However, the authors emphasized that the lower CO₂ emissions associated with the bio-based route could provide additional revenue through participation in the international carbon emissions trading market, potentially mitigating some of the economic drawbacks.

Effective catalyst design and optimization of process conditions are crucial to maintaining catalytic performance. Catalyst deactivation, primarily caused by sintering, leads to a loss of active surface area, reducing efficiency over time. Additionally, pore blockage by heavy hydrocarbons and adsorption of reaction products on active sites further contribute to performance deterioration (POMALAZA *et al.*, 2020; MORAD, 2024). The success and viability of the renewable ethanol-to-BD conversion industry depend on several factors, including the productivity of existing technologies to ensure economic efficiency. In this context, the academic community has consistently worked to deepen the understanding of this process, with a particular focus on the development of high-performance catalysts. These catalysts are essential for improving process efficiency and facilitating the broader industrial adoption of this technology.

2.3 From ethanol to 1,3-butadiene

Prior to the current predominant steam cracking process—in which the conversion of petroleum feedstocks into ethylene also yields valuable byproducts including BD—this compound was first discovered by the French chemist Caventou in 1863, was produced from either acetylene or ethanol (CAVENTOU, 1863). The ethanol-based production method was initially developed in Russia in the early 20th century, driven by the need for a cost-effective approach to producing synthetic rubber from low-cost alcohols. While Armstrong and Miller's 1886 work identified BD as a product of petroleum cracking (ARMSTRONG; MILLER, 1886), ethanol remained the primary feedstock for BD production during the early decades of synthetic rubber manufacturing.

In 1915, Ostromislensky demonstrated that large quantities of BD could be produced by passing a mixture of ethanol and AcH over catalysts such as alumina or clay (OSTROMISLENSKY, 1915). In contrast, in 1929, Lebedev proposed the production of significant amounts of BD through a one-step process utilizing only ethanol (LEBEDEV, 1929). This one-step reaction, known as Lebedev's process, requires a bifunctional catalyst that possesses both dehydrating and dehydrogenating activities. Although Lebedev's catalyst was patented, subsequent studies revealed that it consisted of a mixture of oxides, most likely Si and Mg oxides, with small amounts of other oxides serving as promoters. Several years later, research groups in the United States, building on Ostromislensky's work, developed a two-step mechanism: the dehydrogenation of ethanol to AcH, followed by the reaction of AcH with ethanol to form BD (TOUSSAINT; DUNN; JACHSON, 1947; CORSON *et al.*, 1950).

2.3.1 Reaction mechanisms

The mechanisms proposed for the one-step and two-step processes are generally considered to be similar, although this remains a subject of ongoing discussion and is not yet conclusively established. Lebedev initially suggested a one-step pathway involving radical species, which, through a complex sequence of reactions, would yield BD and other byproducts. However, this approach is now regarded as unlikely. On the other hand, Ostromislensky proposed a two-step route involving the formation of 1,3-butanediol, originating from the rearrangement of a hemiacetal intermediate derived from AcH (OSTROMISLENSKY, 1915). Yet, the feasibility of Ostromislensky's process has also

been questioned, as Toussaint *et al.* argued that the rearrangement of the hemiacetal into glycol is improbable (QUATTLEBAUM; TOUSSAINT; DUNN, 1947). Despite the limitations of the pathways proposed by both Lebedev and Ostromislensky, these early processes remain significant, as they have laid the groundwork for more recent and viable alternative approaches.

Toussaint *et al.* proposed a mechanism based on the aldol condensation between two AcH molecules produced during the dehydrogenation of ethanol (QUATTLEBAUM; TOUSSAINT; DUNN, 1947). The aldol condensation product undergoes dehydration to form crotonaldehyde, which is then hydrogenated and dehydrated to ultimately produce BD. At the time, Toussaint and colleagues suggested that the formation of crotonaldehyde was the rate-determining step of the process, as the direct addition of this reagent to the ethanol feed significantly enhanced BD formation, more so than the addition of AcH. However, Gorin *et al.*, while agreeing with the general mechanism proposed by the Toussaint group, argued that the rate-limiting step was the reduction to crotyl alcohol, rather than the formation of crotonaldehyde (GORIN; DANILINA, 1948).

The primary reaction mechanism pathway currently recognized for BD production from ethanol was first proposed by Kagan *et al.* and subsequently modified by several researchers (BHATTACHARYYA; GANGULY, 1962a). As illustrated in Figure 2.3, the proposed mechanism begins with a) the non-oxidative dehydrogenation of ethanol to form AcH, which then undergoes b) aldol condensation. The resulting acetaldol is subsequently c) dehydrated to form crotonaldehyde, which undergoes d) reduction with ethanol to yield crotyl alcohol, which is then e) dehydrated to form BD. There is no consensus on the rate-limiting step of the overall reaction, as this may vary depending on the system's properties. For basic catalysts with weak redox properties, ethanol dehydrogenation is generally considered the rate-limiting step. In contrast, with Lewis acid catalysts, the reduction step is believed to be the rate-limiting process (MAKSHINA *et al.*, 2014).

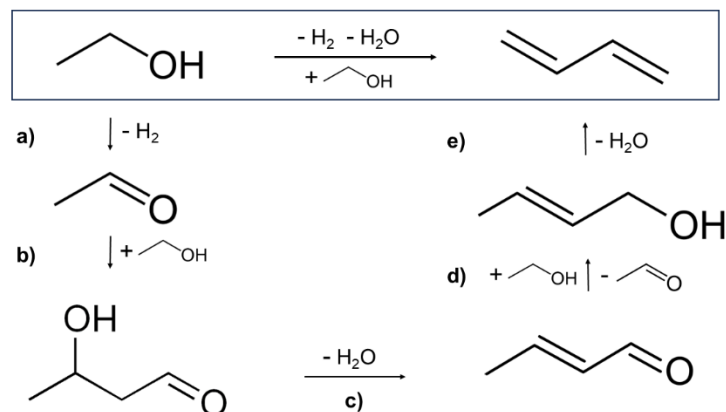


Figure 2.3 – Commonly accepted pathway for the conversion of ethanol to BD.

The catalytic dehydrogenation of ethanol involves the selective cleavage of O–H and C–H bonds, producing AcH and H_2 . This step is considered one of the most crucial in the process, as AcH is responsible for the formation of C_4 precursors, which are essential for the production of BD. In the studies conducted by Di Cosimo and colleagues, they explored how the surface properties of catalysts—specifically the arrangement of Mg and Al metals—affect the conversion and selectivity of this reaction (Figure 2.4) (DI COSIMO *et al.*, 1998, 2000). According to the authors, initially a) the ethanol is adsorbed onto a Lewis acidic site (Mg) and a neighboring Brønsted basic site (O), activating the α -hydrogen. Subsequently, b) a second neighboring basic site abstracts the α -hydrogen. The aldehyde carbonyl is formed, and finally, c) the aldehyde desorbs along with H_2 .

The literature suggests that, in the Lebedev process, the dehydrogenation of ethanol occurs *via* an ethoxide intermediate on the surface. When catalysts possess acid-base pairs at active sites, such as metal oxides, an elimination reaction occurs *via* the E2 route after the formation of the surface ethoxide. In this pathway, a strong nucleophile attacks the hydrogen, transferring its electron pairs to form the double bond without the formation of intermediates. Alternatively, the E1cb route can occur, where a carbanion species is formed (Figure 2.5). Recent findings have determined that AcH is a primary product in the ethanol conversion process, and it is involved in the subsequent steps leading to BD production (SUSHKEVICH *et al.*, 2014; GONZÁLEZ, 2020).

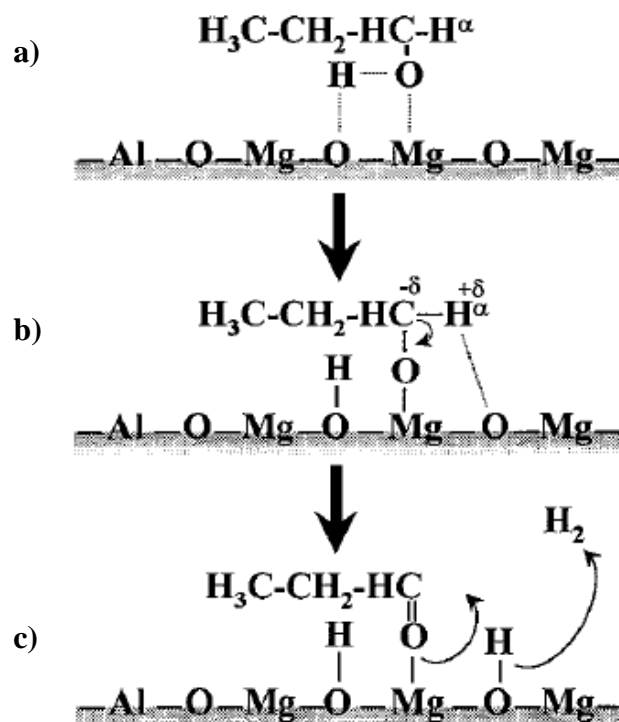


Figure 2.4 – Alcohol dehydrogenation. Adapted from DI COSIMO *et al.*, 2000.

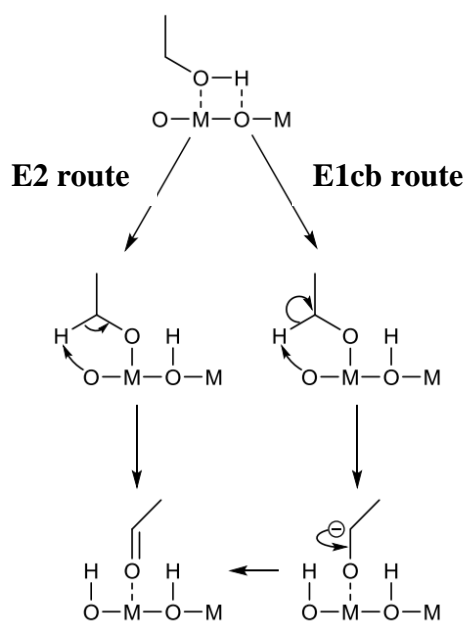


Figure 2.5 – Ethanol dehydrogenation through ethoxide species formation on the surface. Adapted from POMALAZA *et al.*, 2020.

The subsequent step, the aldol condensation of AcH, is crucial for chain growth through the formation of new C–C bonds. The discussion surrounding this stage in the literature primarily focuses on acetaldo, the immediate product of AcH coupling, which, however, is not detected in the effluent of catalytic tests. Many authors attribute this to the rapid conversion of this intermediate into crotonaldehyde (DE BAERDEMAEKER *et*

al., 2015; TAIFAN; BUČKO; BALTRUSAITIS, 2017). Additionally, more recent studies have utilized advanced characterization techniques to confirm the presence of acetaldo. Taifan *et al.* (TAIFAN; BUČKO; BALTRUSAITIS, 2017) employed DRIFTS to identify a band at 1273 cm^{-1} associated with acetaldo, while Gao *et al.* (GAO *et al.*, 2014), using ethanol pulse reaction techniques over MgO–SiO₂ catalysts, observed the sequential formation of AcH, acetaldo, crotonaldehyde, and BD. Rahman *et al.* employed Aspen Plus V12.1 to calculate the thermodynamic properties of reaction steps associated with several proposed mechanisms. However, the authors concluded that the findings related to the precise C–C coupling reaction remain inconclusive and warrant further scrutiny. They emphasized the need for future experimental investigations to elucidate the exact nature of the C–C coupling reaction, which is essential for determining the thermodynamically feasible reaction network for the process (RAHMAN *et al.*, 2024). Despite some ongoing debate regarding the molecular mechanism of this step, with various mechanisms proposed for different catalysts, the simplified process, depicted in Figure 2.6, suggests that: a) enolization of an AcH molecule occurs at acid-base pair sites, forming an active intermediate that b) reacts with a neighboring AcH molecule to form a new C–C bond, culminating in c) the dehydration of the aldol intermediate to crotonaldehyde.

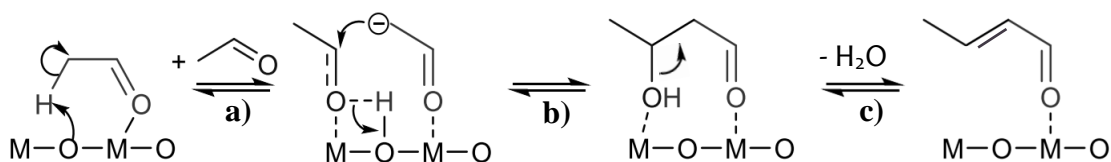


Figure 2.6 – Aldol condensation for the formation of crotonaldehyde. Adapted from POMALAZA *et al.*, 2020.

For BD production, early studies suggested the direct deoxygenation of crotonaldehyde using ethanol as a hydrogen source. However, more recent research has proposed that crotonaldehyde is first reduced to crotyl alcohol, which is then dehydrated to form BD. This conclusion emerged from observations that crotonaldehyde undergoes reduction to crotyl alcohol by H₂, and crotyl alcohol is subsequently dehydrated to BD under typical reaction conditions (MAKSHINA *et al.*, 2014). The presence of crotyl alcohol is now widely acknowledged and supported by several authors (MÜLLER *et al.*, 2016; TAIFAN; BUČKO; BALTRUSAITIS, 2017; YAN *et al.*, 2018), although, similar

to the aldol intermediate, it is sometimes not detectable in the reactor effluent of catalytic testing systems due to its rapid dehydration.

The mechanism of crotonaldehyde reduction to crotyl alcohol has sparked significant debate in the literature regarding the origin of the H₂ involved. Findings by Young and Davis suggest that the direct hydrogenation of C=C or C=O bonds in crotonaldehyde using H₂ as a hydrogen source occurs to a negligible extent, indicating that the reaction predominantly proceeds *via* MPV-like transfer hydrogenation mechanism, where alcohols serve as hydrogen donors (YOUNG; DAVIS, 2018). Some studies propose ethanol as the direct reducing agent (SUSHKEVICH *et al.*, 2014; TAIFAN; BUČKO; BALTRUSAITIS, 2017), while others suggest that ethanol acts as an *in situ* source of hydrogen species on the catalyst surface, facilitating the reduction of the carboxyl group of crotyl alcohol (HAYASHI *et al.*, 2016). In contrast, the dehydration of crotyl alcohol to BD is not extensively discussed, as it is considered a thermodynamically favorable step (BHATTACHARYYA; GANGULY, 1962a; MAKSHINA *et al.*, 2014; RAHMAN *et al.*, 2024), with conversion to the final product occurring promptly after the formation of crotyl alcohol.

Ongoing research by various groups continues to explore and debate the intricacies of the ethanol-to-BD conversion mechanism, with the goal of reaching a more widely accepted scientific consensus on the steps and key factors involved in the process. The renewed focus on the Lebedev process for BD synthesis from ethanol holds considerable economic and environmental significance, offering the potential to produce this compound from a renewable resource. Achieving this goal requires the development of highly efficient heterogeneous catalysts, with particular emphasis on optimizing selectivity. This is crucial, as the expensive and time-consuming purification steps currently necessary for BD production pose significant challenges and should be minimized.

2.3.2 Main catalysts

Literature highlights the critical role of basic and dehydrogenation-active components in catalysts used for the conversion of ethanol to BD. MgO serves as a classic example, functioning as a prototypical catalyst for the Guerbet reaction and frequently employed in the Lebedev process for BD synthesis (CORSON *et al.*, 1950). In purely basic systems, BD yield and selectivity are typically much lower compared to mixed acid-

base systems. However, the presence of acidic sites can enhance competing dehydration pathways. The primary catalysts investigated for the Lebedev process are MgO–SiO₂ or M/MO_x–SiO₂, where M represents a metal (e.g., Ag, Cu) used primarily for ethanol dehydrogenation, and MO_x refers to a metal oxide (CORSON *et al.*, 1950; SUSHKEVICH *et al.*, 2014). In these systems, MO_x predominantly catalyzes aldol condensation, SiO₂ provides the acidic sites required for dehydration, and transition metals facilitate the dehydrogenation of ethanol to AcH, thus optimizing the overall catalytic performance.

Catalytic systems based on MgO and SiO₂ have been under investigation since the 1940s, when it was hypothesized that these components were central to the catalytic system proposed by Lebedev, as described in one of his patents (NATTA, 1947). Since then, MgO–SiO₂ catalysts have been widely utilized and studied for ethanol conversion to BD, with particular focus on the relationship between their structural properties and catalytic performance. It is generally accepted that optimizing BD production requires a fine balance between the acidic and basic properties of the catalyst, achieved through precise tuning of these active sites (ANGELICI *et al.*, 2014; ZHANG; FAN; YU, 2022). Nevertheless, there remains limited consensus regarding the exact nature of these active sites and the specific roles they play in the reaction mechanism.

In 1972, Niiyama and colleagues (NIIYAMA; MORII; ECHIGOYA, 1972) investigated the mechanism of ethanol conversion to BD using an MgO–SiO₂ catalyst (75 % molar fraction MgO), examining the relationship between acid-base properties and catalytic activity. Since the rate-limiting step in this reaction is ethanol dehydrogenation, catalyzed by basic sites, the authors anticipated that increasing the MgO content would enhance the BD formation rate. However, this expectation was not met. When MgO was used as catalyst, crotonaldehyde was observed among the products, indicating that MgO possesses catalytic activity for aldol condensation but appears to lack the capacity to effectively promote the subsequent reaction steps required for BD production. The low overall activity of MgO was attributed to its limited dehydration activity in the final step, which relies on acidic sites. The authors concluded that both acidic and basic sites are essential to improve BD productivity. More recently, He and collaborators (HE *et al.*, 2018) employed TPD techniques to investigate the interaction of ethanol with MgO–SiO₂ catalysts synthesized *via* different methods. The most effective catalyst was prepared using the wet-kneading method, which exhibited high ethanol dehydrogenation activity.

This was demonstrated by a lower desorption temperature of AcH (381 K) and a higher AcH/ethylene ratio (1.2)—key indicators of superior catalytic performance. Similarly, the ammonia evaporation method used to synthesize MgO–SiO₂ catalysts for the conversion of ethanol to BD generated catalysts with a high fraction of magnesium silicate hydrates, which are linked to improved BD selectivity. An optimal Mg/Si molar ratio of 4 yielded a BD selectivity of 37 % and the catalyst maintained its performance without deactivation over 52 h of time-on-stream (TOS) (SAMSUDIN; JAENICKE; CHUAH, 2023).

The MgO/SiO₂ catalyst system was examined to determine the ideal chemical composition for ethanol conversion to BD and the findings revealed that the highest BD yield was attained using MgO/SiO₂ mixed oxide catalysts containing 85–95 % molar fraction of MgO, challenging Lebedev's earlier suggestion of 75 % molar fraction of MgO. NH₃-TPD analysis further demonstrated that the highest acid-site density occurs in catalysts with compositions ranging from equimolar proportions to those enriched in Mg (RESCHETILOWSKI *et al.*, 2020).

Da Ros and colleagues investigated the use of ZrZn/MgO–SiO₂ systems for the conversion of ethanol to BD. The incorporation of Zr and Zn into the catalyst system improved both the yield and selectivity of BD, achieving 38 % selectivity at 648 K and WHSV of 2.5 h⁻¹. However, this modification also led to notable selectivities for ethylene and DEE, reaching up to 35 % and 15 %, respectively. Characterization studies revealed that the addition of Zr and Zn into the MgO–SiO₂ system increased its Lewis acidity. The authors determined that the optimal introduction of an alkaline metal was 1.2 % mass fraction, as higher loadings led to reduced ethanol conversion and BD selectivity, while lower loadings promoted the formation of ethylene and DEE (DA ROS *et al.*, 2017).

Shylesh *et al.*'s study (SHYLES *et al.*, 2016) explored the conversion of ethanol to BD using an MgO–SiO₂ catalyst impregnated with Au nanoparticles. The results demonstrated that this catalyst exhibited high activity and selectivity for BD, with low selectivity for DEE, ethylene, and butenes. The authors attributed this behavior to the presence of both acidic and basic sites on the catalyst. *In situ* infrared spectroscopy of CO₂ adsorption revealed the presence of strong, medium, and weak basic sites. Medium basic sites predominated when the MgO content was low (10–30 % mass fraction), while the proportion of strong basic sites increased as the MgO content rose. As for acidic sites, only strong Lewis acid sites were identified, with no Brønsted acid sites detected. This suggests that the residual silanol groups on the support exhibit only weak acidity.

Due to the varying chemical nature of the active sites involved in the reaction steps, it is evident that catalysts for the conversion of ethanol into higher-value products must be multifunctional—regardless of the proposed mechanism. The key requirements for a catalyst in the ethanol upgrading reaction are dehydrogenation and dehydration properties, demanding acidic, basic, and redox sites. Early studies by Bhattacharyya and colleagues revealed that ZrO_2 and Al_2O_3 catalysts were as competitive as basic catalysts, achieving BD yields of up to 34 % (BHATTACHARYYA; GANGULY, 1962b; BHATTACHARYYA; AVASTHI, 1963). Reaffirming the importance of multifunctional catalysts in ethanol upgrading, Miyake *et al.* (MIYAKE; BREZICKI; DAVIS, 2022) investigated Ag and ZrO_2 catalysts supported on SiO_2 for ethanol conversion to BD at 573 K. The 1Ag/4 ZrO_2 / SiO_2 catalyst achieved a high BD selectivity of 65 %, with a 75 % ethanol conversion. The authors suggested that Ag was responsible for the initial dehydrogenation of ethanol to AcH, while ZrO_2 facilitated C–C coupling and subsequent dehydration reactions. These findings align with earlier work by Dagle and colleagues, who reported that the 1%Ag/4% ZrO_2 / SiO_2 -SBA-16 catalyst demonstrated excellent catalytic performance, achieving 99 % ethanol conversion and 71 % BD selectivity at 598 K. It was noted that Ag had a greater impact on ethanol conversion, while the ZrO_2 content and, consequently, the concentration of Lewis acidic sites had little effect on conversion. The authors also found that BD selectivity was directly related to the concentration of Lewis acidic sites, decreasing as the number of these sites increased, leading to greater dehydration of ethanol to ethylene and DEE (DAGLE *et al.*, 2018). Furthermore, Larina and colleagues discovered that ZnLaZrSi oxide catalyst systems, prepared with different SiO_2 , showed minimal influence of the porous structure properties of the SiO_2 supports on catalytic performance. However, the quantity and strength of Lewis acidic sites had a significant effect on BD selectivity (LARINA *et al.*, 2020).

As highlighted by Angelici *et al.*, a critical aspect of designing optimal catalysts lies in understanding the ideal catalytic functions (acid/base/redox) and the relationship between catalyst structure and its catalytic activity (ANGELICI; WECKHUYSSEN; BRUIJNINCX, 2013). This was previously observed by Kitayama and colleagues, who developed an MgO– SiO_2 catalyst impregnated with Ni (KITAYAMA; SATOH; KODAMA, 1996). By varying the MgO composition while keeping the Ni content constant (10 % mass fraction of NiO), changes were observed in both the basicity and specific surface area of the catalyst. With approximately 30 % mass fraction of MgO, BD

yields reached up to 53 %. Moreover, it was found that BD formation exhibited selectivity of 90 % or higher in ternary oxides, but not in binary oxides (NiO/SiO₂, NiO/MgO). These results confirm the crucial role played by both acidic and basic sites in the conversion of ethanol to BD.

Zhang's group, through UV diffuse reflectance studies, suggested that the addition of SiO₂ to MgO resulted in an increase in structural defects, coordinatively unsaturated O²⁻ ions, and Mg–O–Si interactions (ZHANG *et al.*, 2015; FAN *et al.*, 2017). DFT calculations revealed that ethanol predominantly adsorbs on the MgO surface. The calculated activation energies showed that step-type surfaces are more active than terraces or even corner sites for the dehydrogenation of ethanol to AcH. The authors also explored the mechanism of AcH aldol condensation to 3-hydroxybutanal on Mg²⁺–O²⁻ pairs with different coordinations using periodic quantum chemical methods. On low-coordination Mg²⁺ sites, AcH is adsorbed near the surface, facilitating the abstraction of the α -hydrogen by adjacent O²⁻ or OH. Proton transfer from the α -hydrogen of adsorbed AcH to the MgO surface, along with back-proton transfer to form the desired 3-hydroxybutanal, faces higher energy barriers than the C–C coupling step. This indicates that the proton transfer process is the rate-limiting step in the aldol condensation on MgO. The study concluded that a strong Lewis acid–weak/medium base pair leads to optimal performance. Baltrusaitis collaborated with Taifan on further studies to explore the surface of catalysts used in ethanol conversion reactions (TAIFAN; BUČKO; BALTRUSAITIS, 2017; TAIFAN; YAN; BALTRUSAITIS, 2017). Using DFT, they examined the reaction pathways of ethanol to BD on the MgO surface. The authors identified four critical steps in the process. The dehydration of ethanol to form ethylene has a lower energy barrier than the dehydrogenation step to produce AcH, suggesting the presence of competing reactive pathways. Aldol condensation to form acetaldo is preceded by a free energy barrier of 16.1 kcal/mol, but it is thermodynamically limited by an endergonic free reaction energy of 12.9 kcal/mol. The calculation also reveals another viable route *via* Prins condensation, which has a free energy barrier of 28.8 kcal/mol, with a negative free reaction energy of -22.7 kcal/mol. Finally, the thermodynamic stability of 1-ethoxyethanol prevents the reaction from progressing through the hemiacetal rearrangement. Based on the presented calculations, the authors proposed that multiple mechanisms appear plausible (TAIFAN; BUČKO; BALTRUSAITIS, 2017). In a second study, the authors combined DFT calculations with

in situ DRIFTS to explore the surface of an MgO/SiO₂ catalyst and propose a mechanism for this reaction. The authors reported that the presence of hydrogen-containing molecules in the gas phase, such as ethanol, is a crucial factor in several stages of the process, including AcH condensation and crotonaldehyde reduction. AcH showed high reactivity in forming crotonaldehyde. However, excessive aldehyde intermediates led to strongly bound and stable surface species even at high temperatures, attributed to surface acetate and/or 2,4-hexadienal or polymerized AcH. Crotonaldehyde was reduced by ethanol to produce crotyl alcohol *via* the MPV mechanism. Crotyl alcohol, in turn, was highly reactive and produced two distinct species on the surface, which were subsequently desorbed as BD. The study concluded that complex reactive interactions occur between surface hydroxyl groups, gaseous reagents, and surface-bound reactive intermediates during the conversion of ethanol to BD (TAIFAN; YAN; BALTRUSAITIS, 2017).

In addition to MgO–SiO₂, another key system for this type of reaction is Al₂O₃/ZnO. Both have demonstrated high effectiveness in their pure forms as well as when doped with other metals. MgO and ZnO contribute through basic sites, where dehydrogenation occurs, while SiO₂ and Al₂O₃ provide acidic sites for the dehydration step. It is also evident that the yield of the desired product is significantly influenced by the acid-base site ratio and the nature of the dopants used to enhance the activity of these catalytic systems (OHNISHI; AKIMOTO; TANABE, 1985; MAKSHINA *et al.*, 2012).

Recent studies have reported that combining metal oxides (ZrO₂, MgO, Y₂O₃, or Ta₂O₅) supported on SiO₂ with dehydrogenating promoters (Zn, Ag, or Cu) can form an effective catalyst for the direct conversion of ethanol to BD. Wang and colleagues, when examining a series of MgO–SiO₂ catalysts, found that product selectivity is highly dependent on the ZnO content used as a promoter, as it affects the interaction between MgO and SiO₂ and the acid-base balance of the catalyst surface. Their results showed that MgO–SiO₂ catalysts with low ZnO content are more efficient for C–C coupling and exhibit high selectivity for BD (nearly 58 % when the conversion was over 80 % and ZnO content was 0.2 % mass fraction), while higher ZnO levels favor AcH formation *via* dehydrogenation. The authors proposed that excessive ZnO concentrations may disrupt the Mg–O–Si interfacial bond in these catalysts, which is critical for C–C coupling (WANG *et al.*, 2020). ZnO has been demonstrated to significantly enhance the performance of MgO–SiO₂ catalysts in the ethanol-to-BD conversion process, outperforming other promoters such as Ga₂O₃ and In₂O₃. This improvement is attributed

to ZnO's ability to increase the surface concentration of both reactants and reaction intermediates, thereby facilitating more efficient catalytic interactions, promoting higher conversion rates and greater BD yield (SZABÓ *et al.*, 2020).

Another study evaluated the performance of the multifunctional hierarchical nanostructured ZnZr-Silica-1 catalyst for ethanol conversion to BD, achieving selectivity of up to 61.4 % and conversion of 89.8 % at 623 K over 0.38 h (WANG *et al.*, 2022a). The authors reported a BD yield of 55.1 % with a moderate strong acid-to-total acid ratio of 0.46 and a low strong base-to-total base ratio of 0.64. This result suggests that a specific ratio of strong acid to minimal strong base enhances the conversion of ethanol to BD. Moreover, the catalyst showed superior stability compared to previously reported systems, with minimal variation in ethanol conversion (90.6 % –73.7 %) even after 80 h of reaction, while other systems in the literature exhibited lower conversions in shorter reaction times (POMALAZA *et al.*, 2018; YAN *et al.*, 2018). The authors concluded that the hierarchical nanostructure enhanced resistance to carbon deposition, as it facilitated better diffusion of AcH, which would otherwise deposit on active sites and cause deactivation. Additionally, this structure inhibited secondary reactions that typically lead to coke formation (WANG *et al.*, 2022a). This study highlights the significant influence of catalyst structure, alongside acid-base properties, on catalytic performance in the ethanol-to-BD conversion reaction.

Similar to MgO, hydrotalcites are widely studied heterogeneous basic catalysts. Hydrotalcites, which are layered double hydroxides, are well-known for their role as basic catalysts in various reactions. These materials have a layered structure containing anions and water molecules between positively charged metal hydroxides, with the chemical formula $[M^{2+}_{1-x}M^{3+}_x(OH)_2][(An^-)_{x/n} mH_2O]$. M^{2+} represents a divalent metal ion, such as Mg, Co, Cu, or Ni, while M^{3+} is a trivalent metal ion, such as Al, Fe, or Cr. Notably, Mg–Al hydrotalcites, where the M^{2+} and M^{3+} sites are composed of Mg and Al, are commonly studied examples. Through thermal treatment to decompose carbonates and remove water, these hydrotalcites can be transformed into mixed metal oxide structures (Mg_xAlO_y). These transformations have been the subject of extensive research, particularly due to the presence of acid-base pairs ($Mg^{2+}-O^{2-}$) that impart specific catalytic properties (CAVANI; TRIFIRÒ; VACCARI, 1991; TICHIT *et al.*, 2003; BRITO *et al.*, 2009).

Ordóñez's group has investigated the application of Mg_xAlO_y mixed metal oxide catalysts in the conversion of ethanol to higher products. Initially, these oxides were synthesized through various preparation methods and used in the catalytic condensation of ethanol. The catalyst exhibited activity for both dehydration reactions (due to the presence of acid sites) and hydrogenation/dehydrogenation reactions (attributed to medium-strength basic sites) (LEÓN; DÍAZ; ORDÓÑEZ, 2011). Subsequently, mixed oxide catalysts derived from Mg_3AlO_x hydrotalcites were analyzed, revealing that ethanol predominantly produced BuOH and BD, though substantial amounts of undesirable ethylene were detected at high temperatures. This suggests the existence of a temperature range where basic sites are active, but acid sites are not. The authors proposed the following mechanism: AcH is formed from ethanol *via* dehydrogenation, a reaction involving the dissociative adsorption of ethanol on acid-base pairs. Mg^+-O^{2-} surface pairs catalyze this process, requiring cationic sites adjacent to oxygen positions. The condensation of adsorbed AcH molecules to form BuOH requires the formation of a carbanion intermediate, a step that involves both acid-base pairs and a high density of basic sites. The intermediate species ultimately produce either BuOH or BD (ORDÓÑEZ *et al.*, 2011). In a more recent work, the group explored the optimal distribution of acid and basic sites in mixed oxides containing Cu nanoparticles (QUESADA *et al.*, 2018b). For the study, three types of catalysts were synthesized: Mg–Al mixed oxide, Cu supported on this oxide, and a physical mixture of the oxide with Cu/SiO₂. The catalyst containing 1 % mass fraction of Cu in the mixed oxide demonstrated production rate up to 12 times higher than of the pure oxide at 523 K. At 723 K, it exhibited a maximum production rate of 1600 mmol ks⁻¹ g⁻¹, corresponding to a 37.1 % of conversion and 25.0 % BuOH selectivity, highlighting that the incorporation of the metal significantly enhanced the dehydrogenation step of the reaction. Additionally, DRIFTS results indicated that the species formed during the reaction were consistent across all materials, suggesting that the improved performance was linked to an increased turnover frequency at the active sites and due to mechanistic changes. In a reducing atmosphere, the authors investigated the role of hydrogen in the dehydration step and found that its presence particularly affected the behavior of the mixed oxide catalyst, suggesting competitive adsorption of molecular hydrogen on strong acid sites associated with OH groups. In the material from the physical mixture, this effect was absent, likely due to preferential adsorption of the hydrogen molecule on Cu nanoparticles (QUESADA *et al.*, 2018b).

The industrial interest in upgrading ethanol to higher products is significant, and this is clearly reflected in the extensive body of literature dedicated to exploring this reaction. As summarized in Table 2.1, several systems have been studied for BD production, with their respective results in terms of ethanol conversion (X_{EtOH}), BD selectivity (S_{BD}), and BD yield (Y_{BD}). However, despite the breadth of research, the complexity of this system means that there remain numerous topics to be explored in the field, ranging from advancing the understanding of reaction mechanisms to developing innovative catalytic materials. A prevailing consensus in the literature underscores the fundamental characteristic of catalysts for this reaction: the necessity of achieving an optimal ratio of acidic and basic sites to favor the production of the desired product (KOZLOWSKI; DAVIS, 2013b; CHIEREGATO *et al.*, 2015; POMALAZA *et al.*, 2020). Consequently, researchers have focused on combining materials that provide such complementary sites. Among these, catalytic systems based on MgO and SiO₂ have garnered significant attention, particularly in efforts to elucidate the correlation between their physicochemical properties and catalytic performance (ZHANG *et al.*, 2015; TAIFAN; YAN; BALTRUSAITIS, 2017; WANG *et al.*, 2020; VIEIRA *et al.*, 2022). A critical step in ethanol conversion is aldol condensation, which facilitates carbon chain growth. Evidence in the literature suggests that this step is strongly influenced by interactions between acidic and basic site pairs (KIKHTYANIN *et al.*, 2017; POMALAZA *et al.*, 2020). Thus, mixed oxide catalysts are widely employed for this purpose (DI COSIMO *et al.*, 2000; QUESADA *et al.*, 2018a; MÜCK *et al.*, 2021). Building on this foundation, novel catalytic systems continue to be developed, with the aim of enhancing selectivity toward the desired product and improving process efficiency.

Table 2.1 – Catalysts applied in the conversion of ethanol to 1,3-butadiene.

Catalyst	Mg:Si	Reaction Conditions	X _{EIOH} / %	S _{BD} / %	Y _{BD} / %	Reference
SiO ₂ –MgO	1:1	698 K, 1 atm, 0.5 mL mg ⁻¹ min ⁻¹	49	33	17	ANGELICI <i>et al.</i> , 2014
SiO ₂ –MgO	1:1	698 K, 1 atm, 0.5 mL mg ⁻¹ min ⁻¹	50	12	6	ANGELICI <i>et al.</i> , 2014
ZrZn/MgO–SiO ₂	1:1	648 K, 1 atm, 0.62 h ⁻¹	40	35.9	10.14	DA ROS <i>et al.</i> , 2017
HTO ^a /SiO ₂ -2.5	N/A ^b	523 K, 1 atm, 0.39 h ⁻¹	13.4	14.3	1.92	KUMAR <i>et al.</i> , 2022
HTO ^a /SiO ₂ -5	N/A ^b	523 K, 1 atm, 0.39 h ⁻¹	14.6	43.3	6.32	KUMAR <i>et al.</i> , 2022
MgO–SiO ₂	2:1	573 K, 1 atm, 0.5 g _{EIOH} g _{cat} ⁻¹ h ⁻¹	7	31	2.17	SZABÓ <i>et al.</i> , 2022
MgO–SiO ₂	2:1	673 K, 1 atm, 0.5 g _{EIOH} g _{cat} ⁻¹ h ⁻¹	72	24	17.28	SZABÓ <i>et al.</i> , 2022
Au/MgO–SiO ₂	1:2	523 K, 1 atm, 1.1 h ⁻¹	25	61	15.25	SHYLESH <i>et al.</i> , 2016
Cu/MgO–SiO ₂	1:2	523 K, 1 atm, 1.1 h ⁻¹	25	37	9.25	SHYLESH <i>et al.</i> , 2016

^a Oxide derived from Mg–Al hydrotalcite. ^b not available.

Table 2.1 – Continuing: catalysts applied in the conversion of ethanol to 1,3-butadiene.

Catalyst	Mg:Si	Reaction Conditions	X _{EtOH} / %	S _{BD} / %	Y _{BD} / %	Reference
Mg ₃ AlO _x	n.a. ^c	673 K, 1 atm, 0.33 mL mg ⁻¹ min ⁻¹	51	12.5	6.38	ORDÓÑEZ <i>et al.</i> , 2011
MgO/SiO ₂	76:24	698 K, 1 atm	56	63	35.28	VIEIRA <i>et al.</i> , 2022
MgO/SiO ₂	84:16	698 K, 1 atm	56	74	41.44	VIEIRA <i>et al.</i> , 2022
ZnO/MgO-SiO ₂	3:1	673 K, 1 atm, 1.0 g _{EtOH} g _{cat} ⁻¹ h ⁻¹	29.2	63.8	18.63	KYRIIENKO <i>et al.</i> , 2021
ZnO/MgO-SiO ₂	1:3	673 K, 1 atm, 1.0 g _{EtOH} g _{cat} ⁻¹ h ⁻¹	22.5	36.1	8.12	KYRIIENKO <i>et al.</i> , 2021
9.3%Zn-3%Hf/SiO ₂	N/A ^c	613 K, 1 atm, 1.0 h ⁻¹	69	38	26.22	GONZÁLEZ, 2020
0.3%Ag-4%ZrO ₂ /SiO ₂	N/A ^c	593 K, 1 atm, 0.3 h ⁻¹	30	74	21.6	SUSHKEVICH <i>et al.</i> , 2014
0.3%Ni-4%ZrO ₂ /SiO ₂	N/A ^c	593 K, 1 atm, 0.3 h ⁻¹	10	68	6.8	SUSHKEVICH <i>et al.</i> , 2014

^c not applicable.

2.3.3 Dehydrogenating metals

In order to enhance the performance of catalysts in ethanol conversion reactions, the addition of various metals and metal oxides to the catalyst surface can be employed to fine-tune its properties and improve efficiency. Supported metal catalysts have been shown to significantly enhance ethanol conversion and lower reaction temperatures, largely due to the dehydrogenation capacity of specific metals. These metals typically facilitate the dehydrogenation of primary alcohols and the hydrogenation of unsaturated aldehydes, while adjacent Lewis' acid-base pairs provide active sites for the aldol condensation of AcH and subsequent dehydration (CHIEREGATO *et al.*, 2015; PACHECO *et al.*, 2019).

For atoms to adsorb effectively onto metal surfaces, the metal must have partially filled d-bands capable of accepting electrons. However, the number of vacant states must be carefully balanced. If there are too many, gases may chemisorb too strongly, hindering their subsequent desorption. Conversely, if there are too few, chemisorption may not occur at all. Metals within groups 8, 9, and 10 typically possess an optimal number of vacant d-orbitals, making them well-suited for maximum catalytic activity (Figure 2.7). Additionally, the spatial arrangement of metal atoms on the catalytic surface strongly influences the hydrogenation process by minimizing the energy of reaction transition states. When the activation energy is decreased, the system can operate at lower temperatures. Metals in groups 8, 9, and 10 meet these criteria due to their radial configurations, which promote efficient catalysis (BOND, 1957; LIVINGSTONE, 1973). A metal's ability to dehydrogenate a primary alcohol depends on its capacity to adsorb atomic hydrogen, which is linked to the properties of its d-orbitals. The energy of hydrogen adsorption generally correlates with the position of the d-band center relative to the Fermi level. An upward shift in the d-band center enhances the metal's reactivity and strengthens the hydrogen-metal interaction (HAMMER; NØRSKOV, 2000).

Too strong interaction					Weak interaction			
21 Sc Scandium 44.956	22 Ti Titanium 47.867	23 V Vanadium 50.942	24 Cr Chromium 51.996	25 Mn Manganese 54.938	26 Fe Iron 55.845	27 Co Cobalt 58.933	28 Ni Nickel 58.693	29 Cu Copper 63.546
39 Y Yttrium 88.906	40 Zr Zirconium 91.224	41 Nb Niobium 92.906	42 Mo Molybdenum 95.95	43 Tc Technetium 98.907	44 Ru Ruthenium 101.07	45 Rh Rhodium 102.906	46 Pd Palladium 106.42	47 Ag Silver 107.868
57-71	72 Hf Hafnium 178.49	73 Ta Tantalum 180.948	74 W Tungsten 183.84	75 Re Rhenium 186.207	76 Os Osmium 190.23	77 Ir Iridium 192.217	78 Pt Platinum 195.085	79 Au Gold 196.967
89-103	104 Rf Rutherfordium [261]	105 Db Dubnium [262]	106 Sg Seaborgium [266]	107 Bh Bohrium [264]	108 Hs Hassium [269]	109 Mt Meitnerium [278]	110 Ds Darmstadtium [281]	111 Rg Roentgenium [280]

Figure 2.7 – Illustration of intensity of surface interactions between some metal groups and hydrogen (PACHECO, 2019).

Building upon these principles, various metals have been explored as dehydrogenation agents in a range of reaction systems. Zheng *et al.* investigated highly dispersed Ni–MgAlO catalysts for the conversion of ethanol into higher-chain alcohols (PANG *et al.*, 2016). The optimal catalyst, Ni₄MgAlO, exhibited 55.2 % selectivity for BuOH (and 85 % for total C₄–C₈ alcohols), with an ethanol conversion of 18.7 % at a reaction temperature of 523 K. Characterization results confirmed that metal sites promoted ethanol dehydrogenation, consistent with earlier studies (RIOUX; VANNICE, 2005; SHIMIZU *et al.*, 2009). The hydrogen formed *in situ* was retained on the catalyst surface, facilitating subsequent hydrogenation of crotonaldehyde. Both ethanol conversion and BuOH selectivity were enhanced in this process. This finding underscores a key distinction from non-metal catalysts: BuOH selectivity is influenced not only by acid-base pairs but also by the metal’s ability to facilitate hydrogen transfer and hydrogenation. Xiao *et al.* (XIAO *et al.*, 2023) conducted a study to examine the influence of Cu, Ni, and Al on the performance of catalysts for ethanol to BD reaction. Four different supported Cu catalysts were synthesized: Cu/Al₂O₃, Cu/NiO, Cu/Ni₃AlO_x, and Cu/Ni₁AlO_x. The results demonstrated that Ni-containing catalysts exhibited superior reactivity (with ethanol conversions up to 41.1 %), while Al-containing catalysts provided enhanced stability during ethanol conversion, likely due to their ability to stabilize active Cu species and prevent the agglomeration of metal particles. Characterization studies revealed that Cu species served as active sites for ethanol dehydrogenation and hydrogenation, while the Ni–Al–LDH-derived support offered appropriate acid–base

sites for aldol condensation, similar to what has been reported on the literature (LI *et al.*, 2022; WANG *et al.*, 2022c). Busca's group studied ethanol dehydrogenation (GARBARINO *et al.*, 2020). In one experiment, Cu supported on ZnAl_2O_4 was synthesized and compared with the unsupported material. At low temperatures and conversion rates, the metal-free catalyst predominantly produced DEE (with 57 % selectivity) alongside AcH (29 % selectivity). This behavior indicates the presence of sites that promote both dehydration and dehydrogenation. As the reaction temperature increased, DEE selectivity decreased, while AcH selectivity peaked up to 55 % at 723 K. For the supported material, a markedly different selectivity profile was observed: AcH selectivity remained high, decreasing only slightly from 96 % to 92 % with increasing temperature. This suggests that Cu species may have both poisoned the acid-base sites on the support responsible for DEE production and enhanced ethanol dehydrogenation to AcH (GARBARINO *et al.*, 2020). In another study, the same group examined the Au/ZnZrO_x system as a catalyst for low-temperature ethanol dehydrogenation. Modifying ZrO₂ with ZnO improved selectivity for ethanol dehydrogenation products, such as AcH and acetone, while also providing more anchoring sites for metal addition than standalone ZnO or ZrO₂ nanoparticles. Adding 1 % mass fraction of Au to the support significantly altered the catalyst, eliminating Brønsted acid sites and achieving 100 % selectivity for AcH and hydrogen formation at temperatures below 573 K. A broader temperature range of up to 473 K was achieved by dispersing low Au content in $\text{Zn}_1\text{Zr}_{10}\text{O}_x$, which resulted in higher dispersion (WANG *et al.*, 2016).

Notably, Wass *et al.* reported a family of homogeneous Ru-based catalysts that could significantly advance the study of catalytic performance (DOWSON *et al.*, 2013). The optimal Ru catalyst, incorporating a bis(diphenylphosphanyl)methane ligand, facilitated ethanol upgrading with over 93 % selectivity for BuOH at 22 % ethanol conversion. This high BuOH selectivity on the Ru catalyst is primarily attributed to the precise control over the base-catalyzed aldol reaction of AcH, which resulted in the exclusive formation of C₄ products. However, catalytic activity diminished over time as the Ru complex catalysts decomposed into metal nanoparticles during the reaction. This decrease in catalytic performance is likely due to the ligands' poor tolerance to water, which leads to their decomposition during the reaction. The findings by Nielsen and colleagues also indicated promising results for the use of Ru complexes in hydrogen production (from isopropanol) and ethyl acetate synthesis (from ethanol) (NIELSEN *et*

al., 2011, 2012). Both studies reported high turnover frequencies for the Ru-based catalyst, even under mild conditions, making it highly suitable for industrial applications. For instance, the authors reported turnover frequencies of up to 2,048 h⁻¹ for the dehydrogenation of isopropanol to acetone and up to 15,400 h⁻¹ for the conversion of ethanol to ethyl acetate. Furthermore, Re complexes have also been employed in the homogeneous catalytic upgrading of ethanol, as demonstrated by King and colleagues (KING *et al.*, 2021). The authors observed that Re chelate complexes were effective for the conversion of ethanol to isobutanol, achieving selectivity of up to 35 %.

Studies on homogeneous catalysis involving Ru species have demonstrated its effectiveness as a dehydrogenation agent in the conversion of alcohols to aldehydes. However, these metals are still relatively underexplored in heterogeneous catalysis. Pacheco *et al.* (PACHECO *et al.*, 2019) investigated heterogeneous catalytic systems with Mg-based oxide catalysts and Ru as a promoter to better understand the roles of the metal and oxides in the various parallel reactions occurring within the system. Characterization results showed that incorporating Al³⁺ cations into the MgO structure (Mg_xAlO_y and Ru/Mg_xAlO_y) significantly increased the specific surface area to 293 m² g⁻¹, compared to a maximum of 57 m² g⁻¹ for catalysts without this cation. At the same time, the density of basic sites was reduced from 1.48 μmol m⁻² to 0.38 μmol m⁻². The addition of Ru to the oxide supports led to a 40 % increase in ethanol conversion for Mg_xAlO_y and a dramatic 650 % increase for MgO. This suggests that Ru efficiently promoted the dehydrogenation of ethanol to AcH. Furthermore, Ru may have also facilitated the decomposition of AcH into methane and CO, and subsequently, CO—when in the presence of a suitable hydrogenation catalyst—could undergo hydrogenation or hydrogenolysis to form methane. This could explain the observed reduction in AcH yield with the addition of Ru.

According to Dagle *et al.*, the performance of supported Lebedev catalysts is highly influenced by the dispersion of their promoter (DAGLE *et al.*, 2018). When equimolar amounts of Ag-modified ZrO₂ were dispersed on SiO₂, the authors identified a clear correlation between the size of the Ag nanoparticles and ethanol conversion. Catalysts with ethanol conversion rates ranging from 29 % to 40 % exhibit lower Ag dispersion, approximately 20 %. Conversely, catalysts achieving ~80 % conversion display higher Ag dispersion, ranging from 30 % to 50 %. Rousseau *et al.* further noted that high dispersion of Ag particles induced partial charge on the particles, a key feature identified as crucial for the dehydrogenation of ethanol (AKHADE *et al.*, 2020).

Chen *et al.* investigated the crucial step of β C–H bond cleavage in the dehydrogenation of ethanol over pure ZrO₂ and Ru-impregnated ZrO₂ catalysts (CHEN; WU; HO, 2011). Overall, the Ru/ZrO₂ catalyst exhibited superior performance in ethanol conversion compared to the pure ZrO₂. The Ru/ZrO₂ surface significantly reduced the activation energy for O–H bond cleavage, lowering it from 3.00 kcal/mol to 1.62 kcal/mol. Additionally, the higher energy barrier for β C–H bond cleavage on ZrO₂ (59.07 kcal/mol) compared to Ru/ZrO₂ species (23.02 kcal/mol) indicates that the Ru atom plays a critical role in activating the C–H bond. The excellent performance of Ru/ZrO₂ in ethanol dehydrogenation may stem from the catalytic effect of the deposited Ru atoms, which help minimize distortion of the ZrO₂ surface and enhance interactions with the adsorbates. Using *in situ* FT-IR, Yuan *et al.* (YUAN *et al.*, 2022) studied the role of atomic Ru in the conversion of ethanol to C₄₊ alcohols in a system where the metal was supported on Mg–Al layered double oxides. Their results confirmed that Ru actively participated in ethanol adsorption, activation, and dehydrogenation, consistent with catalytic outcomes, and demonstrated the remarkable ability of atomic Ru in the condensation process. MgO, Al₂O₃, and hydroxyapatite were the supports chosen by Lisi *et al.* to disperse Ru and Ni for the study of their behavior in the conversion of ethanol to BuOH (CIMINO; LISI; ROMANUCCI, 2018). The performance of unsupported catalysts was enhanced by adding metal (Ru or Ni), leading to a simultaneous increase in both specific surface area and basicity. The higher specific surface area created by metal dispersion provided more active sites for ethanol coupling. Notably, the addition of metal altered the number and nature of basic sites, increasing from 0.064 mmol/g to 0.28 mmol/g. The metal reduction occurring within the reaction's operational temperature range also suggests that the metal's redox properties contribute to promoting the hydrogenation/dehydrogenation steps in the reaction pathway.

Transition metal catalysts for hydrogenation and dehydrogenation reactions are not limited to just Ir, Rh, or Ru, but also include Re. Rhenium exhibits a wide range of oxidation states, from -3 to +7, and can easily transition between them, making it a promising candidate for catalytic applications. Notably, Re has several stable oxidation states (+3, +4, +6, +7), as well as its metallic form, Re⁰, all of which have been reported in hydrogenation reactions (DAVENPORT; KOLLONITSCH; KLEIN, 1968). Re oxides are commonly used as catalysts in both oxidation and reduction processes. Additionally, Re₂S catalysts have been employed in the hydrogenation of organic compounds and in

the dehydrogenation of alcohols to form aldehydes and ketones (MILLENSIFER, 2010). Some researchers even contend that Re-based catalysts are underappreciated, particularly when compared to the extensive focus placed on Pt, Pd, or Ni as hydrogenation catalysts (BROADBENT *et al.*, 1959; GOTHE *et al.*, 2021).

The catalytic dehydrogenation of propane using Re-modified catalysts was investigated by Guo and colleagues (GUO *et al.*, 2005). They observed a reduction in strong acid sites upon impregnation of 6 % mass fraction of Re onto HZSM-5, resulting in a significant improvement in propane dehydrogenation, achieving 90 % conversion, compared to the Ga/HZSM-5 catalyst, which had only 85 % conversion. Re strongly interacts with the Al in the zeolite structure, causing its dealumination, and promotes the exchange of protons from Brønsted acid sites with Re ions, as Brønsted acid sites are the primary strong acid sites. Recently, Chanklang *et al.* studied the hydrogenolysis of glycerol to 1,3-propanediol over H-ZSM-5 catalysts modified with Re and Ir oxides (CHANKLANG *et al.*, 2022). They found that glycerol conversion and 1,3-propanediol yield were strongly influenced by the catalyst composition (Re/Ir) and the amount of metal dopant. Moreover, the addition of Re to the catalyst enhanced the dispersion of Ir. The literature also reports a study on CuO doped with high-valency Re, supported on TiO₂ nanotubes, for the photoelectrocatalytic reduction of CO₂ (LU *et al.*, 2021). High-valency Re doping significantly improved the catalytic activity and selectivity of the Re–CuO/TiO₂ nanotube catalysts. These findings suggest that Re doping promotes C–C coupling, leading to the selective conversion of CO₂ into ethanol.

In its ReO_x form, Re is frequently used as a dopant for other noble metals that are primarily employed for H₂ dissociation, such as Au, Pd, Pt, Ir, or Rh (WANG *et al.*, 2019; FIGUEREDO *et al.*, 2021). However, Re can also serve as the sole active metal in certain hydrogenation reactions. Liu and colleagues investigated the combination of ReO_x/SiO₂ with other noble metals and its application in the hydrogenation of stearic acid. They found that the selectivity for the primary product, stearyl alcohol, was 93 % for the pure oxide and 94 % when the catalyst was Ir–ReO_x, despite the increased conversion with the addition of Ir (LIU *et al.*, 2018). In bimetallic catalysts comprising a noble metal and ReO_x, the noble metal is typically responsible for the dissociative chemisorption of H₂ and the addition of –H to the substrate. ReO_x, on the other hand, plays a key role in the adsorption of oxygenated substrates, while also assisting in protonation or dehydration steps, acting as a Lewis or Brønsted acid (AMADA *et al.*, 2011; CHIA *et al.*, 2011;

VARGHESE *et al.*, 2019; LI *et al.*, 2020). Rhenium serves as an effective active site for various hydrogenation processes; the remarkable efficiency of catalysts utilizing Re species as the primary active centers can be achieved through appropriate pretreatment procedures. However, due to Re's low electronegativity (1.9) and strong oxophilic nature, the reduction of Re species is typically incomplete, resulting in a limited fraction of Re^0 present on the catalyst surface. Consequently, $\text{Re}^{\delta+}$ species, characterized by their favorable redox properties, predominantly function as the active centers for the majority of hydrogenation reactions (LUO; LIANG, 2024a).

In 1990, Ryashentseva and colleagues demonstrated that mixed Re oxide and perovskite catalysts exhibited high catalytic activity for benzene hydrogenation (RYASHENTSEVA, 1990). The authors noted that the metallic phase of Re did not appear to significantly affect activity, but suggested that Re^{6+} or Re^{4+} sites, formed on the partially reduced surface, could be the active species in catalysis. The activity of these sites was found to depend on the geometric structure and chemical composition of the nearby ions. More recently, this hydrogenation capability was also observed for carboxylic acid hydrogenation (TOMISHIGE; NAKAGAWA; TAMURA, 2020). The authors proposed that in Re–Pd/SiO₂ catalysts, Re was the primary catalytically active component. Tests with Pd/SiO₂ showed minimal activity, while Re/SiO₂ monometallic catalysts exhibited some activity, and Re–Pd/SiO₂ bimetallic catalysts displayed significantly higher activity than Re/SiO₂ with the same amount of Re. The high catalytic activity of Re_2S_7 for hydrogenation was first reported in the 1950s (BROADBENT; SLAUGH; JARVIS, 1954). However, advancements in the use of Re as a catalyst appear to have slowed, as the current literature on its application in dehydrogenation reactions remains sparse, leaving substantial potential for further exploration and investigation to address this gap.

The literature on the ethanol-to-BD conversion reaction has extensively explored the appropriate reaction conditions; however, significant gaps remain concerning the optimal properties of the catalytic materials employed. Early studies on Lebedev's process concluded that both acidic and basic sites are essential for enhancing BD productivity (NIIYAMA; MORII; ECHIGOYA, 1972; ANGELICI; WECKHUYSEN; BRUIJNINCX, 2013; SHYLES *et al.*, 2016), prompting ongoing efforts to deepen our understanding of this balance. Nevertheless, the precise quantification and characterization of this "site balance" remain inadequately addressed. Furthermore, while

some metals have been widely investigated for improving ethanol conversion processes, particularly in optimizing the dehydrogenation step, there remains limited exploration of certain promising metals, such as Ru and Re. Despite their demonstrated potential in various catalytic reactions (MILLENSIFER, 2010; CHANKLANG *et al.*, 2022) and their favorable properties for this system, especially as dehydrogenating agents (NIELSEN *et al.*, 2012; PACHECO *et al.*, 2019; KING *et al.*, 2021), these metals have been largely overlooked or insufficiently studied. This body of literature suggests substantial opportunities for further investigation, which this work aims to address by exploring the influence of the acidic-basic properties of catalysts, specifically by synthesizing a new $Mg_xAlO_y-SiO_2$ material with varying molar ratios for use in catalytic ethanol conversion. Additionally, to optimize the dehydrogenation step, the impregnation of promising dehydrogenating metals, Ru and Re, will be investigated, and their catalytic performance in ethanol conversion will be evaluated.

Chapter 3

Methodology

3.1 Catalyst synthesis

The ternary oxide catalysts evaluated in this study were prepared *via* coprecipitation, based on an adaptation of the methodology proposed by DI COSIMO *et al.* (DI COSIMO *et al.*, 1998), which involves the combination of metal salts in an aqueous phase with alkaline solutions to produce an insoluble metal hydroxide and/or carbonate. This precipitation process can be triggered by variations in system conditions, such as changes in temperature, pH values, evaporation, and salt concentration, which influence crystal growth and aggregation (DERAZ, 2018). The method typically follows these steps: (i) a homogeneous solution is prepared by dissolving the precursors of the active components in an appropriate solvent; (ii) the solution undergoes modifications in system parameters, such as pH adjustment or evaporation, to initiate the precipitation process; (iii) the precipitate is then collected *via* filtration and gradually dried to a temperature near the boiling point of the medium; (iv) once the solid is in powder form, thermal treatment is applied to convert the salt or hydroxide forms of the active components into oxides through reaction with air at the appropriate temperature.

The catalysts were prepared from an aqueous solution containing the nitrate salts, $\text{Mg}(\text{NO}_3)_2 \cdot 6\text{H}_2\text{O}$ and $\text{Al}(\text{NO}_3)_3 \cdot 9\text{H}_2\text{O}$, and a solution of TEOS ($\text{Si}(\text{OC}_2\text{H}_5)_4$) diluted in ethanol, with a volumetric ratio of TEOS to ethanol of 1 to 5. The amounts of each reagent were stoichiometrically determined, varying according to the desired Mg:Al:Si ratio in the final material. Both solutions were added dropwise and simultaneously to a beaker containing 300 mL of distilled water, while maintaining continuous magnetic stirring. Additionally, an aqueous solution of KOH and K_2CO_3 was introduced concurrently to ensure that the pH of the main solution remained near 10, facilitating the precipitation process. It is well documented in the literature that a pH around 10 is optimal for the synthesis of Mg-Al hydrotalcites, as deviations from this value tend to favor the precipitation of $\text{Al}(\text{OH})_3$ or $\text{Mg}(\text{OH})_2$, as illustrated in Figure 3.1 (TAMURA *et al.*, 2006;

NISHIMURA; TAKAGAKI; EBITANI, 2013). The reagents used in the synthesis are listed in Table 3.1.

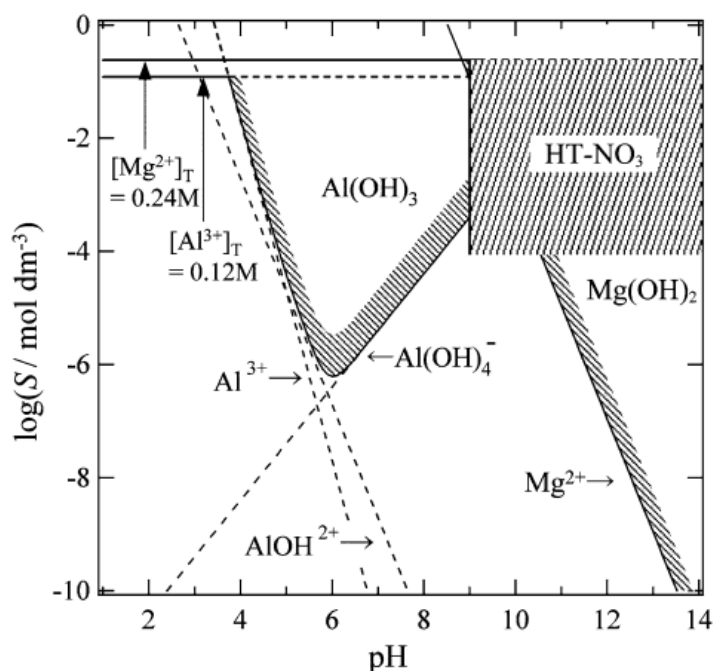


Figure 3.1 – Domain diagram for $\text{Al}(\text{OH})_3$, $\text{Mg}(\text{OH})_2$, and hydrotalcite HT- NO_3 , with S on the y-axis defined as solubility TAMURA *et al.*, 2006.

Table 3.1 – Reagents used in the catalyst synthesis.

Reagent	Formula	Manufacturer	Purity /	Molar mass
			%	/ g mol^{-1}
Magnesium nitrate	$\text{Mg}(\text{NO}_3)_2 \cdot 6\text{H}_2\text{O}$	Sigma-Aldrich	99	256.41
Aluminum nitrate	$\text{Al}(\text{NO}_3)_3 \cdot 9\text{H}_2\text{O}$	Sigma-Aldrich	98	375.13
Tetraethylorthosilicate (TEOS)	$\text{Si}(\text{OC}_2\text{H}_5)_4$	Sigma-Aldrich	98	208.33
Ethanol	$\text{C}_2\text{H}_5\text{OH}$	Sigma-Aldrich	≥ 99	46.07
Potassium carbonate	K_2CO_3	Sigma-Aldrich	≥ 99	138.21
Potassium hydroxide	KOH	Sigma-Aldrich	≥ 85	56.11

Once all the reagent solutions had been added, the system was kept under stirring at 333 K for 40 min. After this period, the precipitate was vacuum-filtered and abundantly washed with distilled water to remove residual K from the carbonate. The filtered and washed material was then transferred to an oven, where it was maintained at 393 K overnight to remove surface water. Following the drying process, the material underwent

thermal treatment, which was responsible for inducing the conversion of the hydroxides to their corresponding oxides.

According to Ramasamy *et al.* (RAMASAMY *et al.*, 2016a), the thermal treatment temperature of hydrotalcites has a negligible effect on their selectivity in the ethanol conversion reaction to higher-value products. The study, which investigated a broad temperature range from 723 K to 973 K, demonstrated minimal variation in product selectivity, as illustrated in Figure 3.2. Consequently, the synthesized materials were subjected to a heating ramp starting from ambient temperature at a rate of 1 K min⁻¹, followed by a hold at 873 K for 12 h.

Following the thermal treatment, a white powder is obtained. Using a mortar and pestle, the solid is finely ground and sieved through Tyler sieves to achieve a particle size distribution between 106 µm and 180 µm. This specific particle size range is selected as an attempt to minimize diffusional effects within the reaction system and to prevent excessively fine particles from escaping the reactor, which could potentially accumulate in the reactor unit lines (PACHECO *et al.*, 2019). The samples were designated as MASxyz, where xyz corresponds to the molar ratio of Mg:Al:Si (x:y:z).

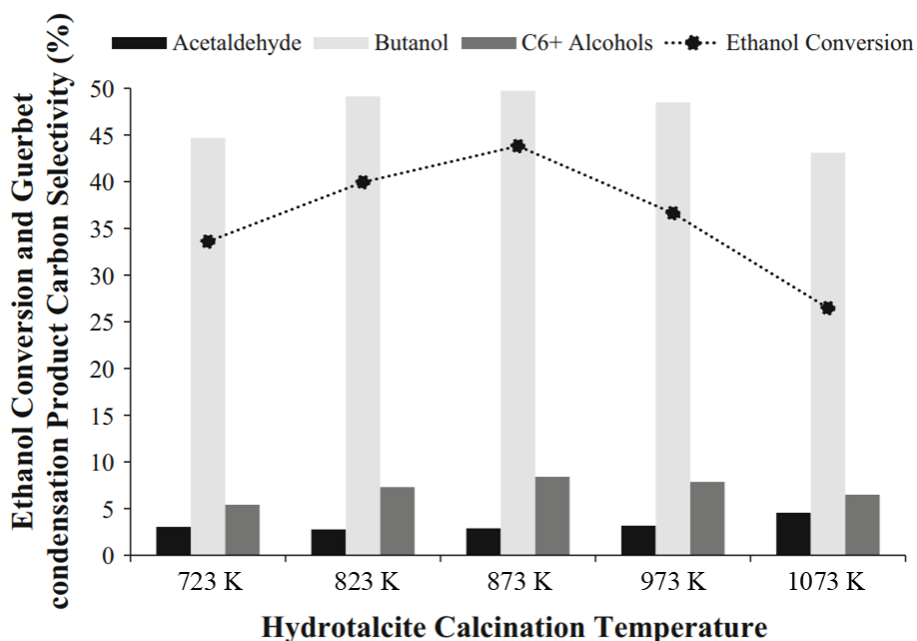


Figure 3.2 – Influence of the thermal treatment temperature of hydrotalcites on the ethanol conversion reaction to higher value-added products. Adapted from RAMASAMY *et al.*, 2016a.

After initial catalytic studies, the metals Ru and Re were deposited onto one of the previously synthesized catalysts based on its performance in the reaction system. This deposition was carried out using the incipient wetness impregnation technique, a method in which a precursor solution is brought into contact with a solid material and subsequently dried to form an active phase. In this approach, the volume of the precursor solution is carefully matched to the pore volume of the support material or slightly less, ensuring optimal interaction (DERAZ, 2018).

To prepare the impregnated materials, a solution containing the metal precursor was incrementally added to the catalyst dropwise until the solid reached saturation. The saturated material was then subjected to drying at 393 K under static air to remove surface moisture. This process was repeated iteratively until the entire precursor solution was incorporated into the oxide, ensuring uniform deposition of the active phase. While earlier studies in the literature have predominantly focused on catalysts with metal loadings mass fraction of 1 % or higher (PANG *et al.*, 2016; WANG *et al.*, 2016), a growing body of recent research has shifted toward exploring the potential of catalysts with metal promoter loadings below a mass fraction of 1 % (CIMINO; LISI; ROMANUCCI, 2018; PACHECO *et al.*, 2019). In alignment with this trend, the present work selected a metal loading mass fraction of 0.1 %. After impregnation, the samples underwent drying, followed by thermal treatment at 773 K (based on TPR results *infra*) for 12 h, at a controlled heating rate of 1 K min⁻¹, to remove organic ligands and to form the final catalytic material.

3.2 Catalyst characterization

3.2.1 X-ray Fluorescence (XRF)

The chemical composition of the bulk was analyzed by XRF at the Hydrogen Technology Laboratory (LabTech) of the Escola de Química at the Universidade Federal do Rio de Janeiro, using a Rigaku Primini equipped with a Pd X-ray source tube and operated at 4 kW. The sample preparation involved forming approximately 300 mg of the sample into circular pellets.

3.2.2 Inductively Coupled Plasma Optical Emission Spectroscopy (ICP-OES)

Elemental analysis was also conducted using ICP-OES with a Thermo Scientific iCap RQ, employing Ar as the carrier gas. For sample preparation, digestion was performed using a solution containing a balanced mixture of hydrofluoric acid (HF), nitric acid (HNO₃), and hydrochloric acid (HCl), under controlled conditions at a temperature of 453 K.

3.2.3 X-ray Diffraction (XRD)

The crystallographic properties of the synthesized catalysts were analyzed at the Multiuser X-ray Diffraction Laboratory (LMDRX) of the Chemistry Institute at the Universidade do Estado do Rio de Janeiro. A Bruker D8 Advance diffractometer equipped with a Cu X-ray source (CuK α , $\lambda = 1.5418 \text{ \AA}$) was used for the analyses. Diffraction patterns were collected over a Bragg angle range of 2° to 90° in continuous scan mode, with a step size of 0.02°. The resulting diffractograms were subsequently analyzed using the X'Pert HighScore Plus® software, which facilitated phase identification and characterization by comparison with the comprehensive database of the International Centre for Diffraction Data (ICDD/JCPDS).

The crystalline phases were further examined under *in situ* and *operando* conditions at the PAINEIRA beamline of the Brazilian Synchrotron Light National Laboratory (LNLS). The beamline was operated at an energy of 19.5 keV. The samples were loaded into a capillary and subjected to a temperature ramp up to 773 K (based on TPR results *infra*) at a controlled heating rate of 10 K min⁻¹ under a flow of 3 % H₂ in He for the metal-containing materials, and 20 % O₂ in N₂ for the non-metallic samples. Upon reaching the target temperature, the samples were held for 60 min to ensure complete reduction, followed by cooling to the reaction temperature of 723 K, at which point a flow of 5 % ethanol in He was introduced. The reaction was conducted for approximately 120 min for all samples. The evolution of the reaction was continuously monitored using an online gas chromatography coupled to a mass spectrometer (GC-MS) to ensure the occurrence of the catalytic transformation under reaction conditions, thereby validating that the XRD measurements were conducted under *operando* conditions. Throughout this process, synchrotron XRD profiles were collected at one-min intervals using a high-

speed, arc-shaped detector (PiMega 450D). Data acquisition was performed in Debye-Scherrer geometry, with diffraction patterns recorded up to a 2θ angle of 109° . The diffractograms were evaluated using the Iguape software to determine potential structural changes in the materials.

3.2.4 Thermogravimetric Analysis (TGA)

TGA was conducted to assess the thermal stability and decomposition behavior of the oxide catalyst precursor, providing insights into its phase transformations and optimal thermal treatment conditions to achieve the desired oxide phase while minimizing undesired by-products or structural degradation. The measurements were carried out using a HITACHI STA 7300 instrument, with heating rate of 10 K min^{-1} up to 1273 K under a flow of $40 \text{ cm}^3 \text{ min}^{-1}$ of N_2 and $10 \text{ cm}^3 \text{ min}^{-1}$ of O_2 .

3.2.5 N_2 Physisorption

N_2 physisorption was conducted to determine the textural properties of the catalysts, including specific surface area calculated using the BET (Brunauer-Emmett-Teller) model, as well as pore size distribution and pore volume using the BJH (Barrett-Joyner-Halenda) method. The analysis was performed on a Micromeritics ASAP 2020 instrument. Prior to the measurements, the catalysts underwent a pre-treatment process to remove residual moisture (573 K for 860 min under vacuum). Adsorption and desorption isotherms were then collected, recording the amount of N_2 adsorbed as a function of its partial pressure.

3.2.6 Temperature-Programmed Desorption (TPD)

TPD tests were employed to identify acidic and basic sites using NH_3 and CO_2 as probe molecules, respectively. The analysis consists on adsorbing a probe molecule onto the catalyst surface and monitoring its desorption profile under a flow of He while gradually increasing the temperature.

To evaluate the basic sites, CO_2 was employed as the probe molecule. Approximately 100 mg of each sample was subjected to analysis. A pre-treatment step was conducted to remove residual moisture by exposing the samples to a He flow at 30 mL min^{-1} , with a controlled heating rate of 10 K min^{-1} , gradually increasing the temperature from room temperature to 623 K , followed by a holding time of 30 min at

the target temperature. The system was then cooled to room temperature under the same He flow conditions. Following the drying process, the samples were exposed to ultra-pure CO₂ at a flow rate of 30 mL min⁻¹ for 30 min to enable adsorption. The samples were then purged with pure He at the same flow rate and ambient temperature for approximately 1 h to remove any weakly adsorbed species. Finally, the desorption step was carried out under a He flow of 60 mL min⁻¹, with the temperature ramped from room temperature to 1073 K at a heating rate of 10 K min⁻¹.

The procedure for identifying acidic sites utilized NH₃ as the probe molecule and followed a methodology analogous to that employed for basic site determination. The flow rates, temperature profiles, and heating ramp conditions were maintained consistently across all steps. However, following the drying process, the samples were exposed to a gaseous mixture containing 4 % NH₃ in He to facilitate adsorption, replacing the ultra-pure CO₂ stream used in the basic site analysis.

All procedures were conducted using a multi-functional analytical unit equipped with an inline quadrupole mass spectrometer, model QUADSTAR 422 (QMS 200, BALZERS), ensuring precise detection and analysis of desorbed species. Two species were monitored by the mass spectrometer: NH₃ (m/z = 15) and CO₂ (m/z = 44).

3.2.7 Scanning Electron Microscopy (SEM)

SEM was employed to investigate the morphological properties of the catalyst. The analyses were conducted at the Nanotechnology Characterization Center for Materials and Catalysis (CENANO) of the National Institute of Technology (INT). A Quanta FEG 450 microscope (FEI Company), operating at 5 kV under high vacuum conditions, was used for the measurements. The samples were pre-coated with Pt using an Emitech K500X metallizer.

3.2.8 Temperature-Programmed Reduction (TPR)

To investigate the behavior of the metal-doped catalysts under reducing conditions, TPR was employed. The TPR profiles enabled the evaluation of the reducibility of active sites and provided critical insights into the temperatures at which phase transitions occur within the catalyst structure. This information is essential for optimizing *in situ* pre-treatment conditions and ensuring the catalytic system's effectiveness during the reaction.

The experiments were performed in a quartz reactor enclosed within a furnace, using approximately 200 mg of catalyst per analysis. The samples underwent a pre-treatment step to eliminate residual moisture, which involved heating under Ar flow of 30 mL min⁻¹ at a gradual ramp rate of 10 K min⁻¹, reaching 773 K. This temperature was held constant for 1 h. The system was then allowed to cool to ambient temperature while maintaining the same Ar flow conditions. Following pre-treatment, the catalysts were exposed to a gas mixture of 10 % H₂ in Ar at a flow rate of 30 mL min⁻¹, with the temperature increased at a rate of 10 K min⁻¹ until reaching 1273 K, during which the H₂ adsorption was continuously monitored and registered using a thermal conductivity detector (TCD).

3.2.9 Ultraviolet-Visible Diffuse Reflectance Spectroscopy (DRS UV-Vis)

The DRS UV-Vis technique was employed to identify the coordination state of the metals (Re and Ru). The analyses were conducted using a Varian Cary 5000 UV-VIS-NIR spectrophotometer. The spectra were collected in the wavelength range of 200 nm to 800 nm, thus covering both the visible and ultraviolet regions of the electromagnetic spectrum. Measurements were conducted from room temperature to 773 K (based on TPR results *infra*), with spectra collected at intervals of every 100 K. The absorbance data obtained from the analyses of the Re- and Ru-doped catalysts, normalized using the support as a reference, were employed to calculate the reflectance as a function of wavelength. The optical band gap of the samples was determined based on the Kubelka–Munk theory.

3.2.10 X-ray Photoelectron Spectroscopy (XPS)

XPS was applied to examine the chemical states, electronic environments, and surface composition of the catalysts, offering details into their surface chemistry, elemental distribution, and bonding characteristics. The analyses were conducted at Laboratório Nacional de Nanotecnologia (LNNano), part of the Energy and Materials Research National Center (CNPEM). Prior to measurement, all samples underwent thermal treatment in a pure He atmosphere (100 mL min⁻¹) at 773 K to minimize potential memory effect. Since *in situ* analysis was not feasible under the available experimental conditions, this *ex situ* thermal treatment was considered the most suitable alternative to

approximate the sample state during reaction. XPS data were acquired using a K-alpha XPS (Thermo Scientific) under high vacuum conditions ($\sim 10^{-7}$ mbar). A monochromatic Al K α radiation (1486 eV) was employed as the excitation source. Survey scans were used for the oxides, collected at a pass energy of 150 eV, with a resolution of 1 eV, while high-resolution scans were employed to detect the low-concentration metal, recorded at a pass energy of 50 eV with 0.1 eV steps. The acquired spectra were processed by fitting Gaussian-Lorentzian product peaks to the data with the CasaXPS software package following the removal of Shirley background. Binding energy calibration was referenced to the C 1s signal (284.6 eV).

3.3 Catalytic testing

Argon (Ar), selected as the inert carrier gas for the reactions, was fed through an external line and directed into a bubbler containing ethanol (ACS ISO reagent, Merck). The temperature of the bubbler was maintained using an integrated thermal bath, enabling control over the amount of ethanol introduced into the system. The ethanol vapor flow was calculated in advance using the Antoine equation, as expressed in Equation 4.1, where p_v represents the vapor pressure of ethanol, T is the system temperature in K, and A , B , and C are the Antoine equation constants. This setup served as the ethanol feed system for the reactions.

$$\ln(p_v) = A - \left(\frac{B}{C+T}\right) \quad 4.1$$

The Ar stream, pre-saturated with the desired ethanol concentration, was introduced into a U-shaped quartz reactor enclosed in a PID-controlled furnace. The reaction temperature was monitored using a thermocouple positioned at the catalyst bed height. System pressure was continuously monitored and maintained at 1.1 bar *via* a manometer installed at the Ar inlet. All internal lines of the reaction unit were kept at 393 K using thermocouples strategically placed at various points to prevent condensation and the formation of cold spots. The outlet stream was directed to a gas chromatograph (Shimadzu GC-2014) equipped with two columns: a PoraBOND Q column (50 m \times 0.32 mm I.D.) and a Carboxen 1010 column (30 m \times 0.53 mm I.D.). The former was coupled to a flame ionization detector (FID), while the latter was paired with a thermal conductivity detector (TCD) for analyzing lighter products. Data processing was

performed using GCSolution software v. 2.32, which provided information on catalytic performance. For all experiments, unless stated otherwise, the catalyst bed contained 100 mg, with a feed flow rate of 25 mL min⁻¹ comprising 5 % volume fraction of ethanol, resulting in a gas hourly space velocity (GHSV) of 0.25 mL mg⁻¹ min⁻¹. Prior to each reaction, the Re- and Ru-doped catalysts underwent *in situ* reduction treatment to facilitate the presence of the metals in their metallic state rather than as oxides. This process involved H₂ flow at 30 mL min⁻¹, with heating at a rate of 10 K min⁻¹ up to 773 K (as determined by TPR results *infra*) and held for 60 min. For the non-impregnated catalysts, thermal activation was performed under an Ar flow rate of 30 mL min⁻¹, with heating at a rate of 10 K min⁻¹ up to 873 K, to ensure the activation of the catalytic sites.

Ethanol conversion and product selectivity were calculated using Equations 4.2 and 4.3, respectively:

$$X_{EtOH} (\%) = \left(\frac{F_i - F_f}{F_i} \right) \times 100 \quad 4.2$$

$$S_k (\%) = \left(\frac{C_k}{C_{TOTAL}} \right) \times 100 \quad 4.3$$

where F_i and F_f were used to calculate ethanol conversion (X_{EtOH}) and represent the amounts of ethanol at the inlet and outlet stream, respectively, as determined by chromatographic analysis; and C_k is the concentration of a specific product k , and C_{TOTAL} is the sum of the concentrations of all products, used to determine the reaction selectivity to product k .

Chapter 4

Results and Discussion

Some of the results and discussion presented in this chapter have been previously reported in a publication associated to this thesis, Santos *et al.* (2025). It includes the initial phases of the study, encompassing pre-impregnation catalyst screening, characterization, and selected catalytic performance data. Nonetheless, this chapter provides an extended discussion of the results, incorporating additional experimental data, and further results and analysis regarding impregnated catalysts.

4.1 Catalyst characterization

4.1.1 Chemical composition

The chemical composition of the samples was analyzed using XRF, EDS coupled with SEM, and ICP, with the results summarized in Table 4.1. XRF, a bulk elemental quantification technique, revealed that the measured elemental compositions of all catalysts were generally consistent with the expected values, with minor deviations. EDS, a method that provides localized surface composition analysis, was conducted on three distinct regions of each catalyst, and the reported values represent the average measurements from these regions. The EDS results similarly aligned with the nominal compositions. Likewise, ICP, which quantifies elements based on the emission of light from excited atoms, yielded results that were in agreement with the expected compositions, with slight deviations observed. The chemical composition of the impregnated materials was assessed exclusively through ICP analysis, which is particularly suited for detecting such small concentrations of metal. The results demonstrate that the measured values are consistent with the expected compositions, corresponding to the nominal 0.1 % mass fraction of each metal, indicating a highly successful impregnation methodology.

Table 4.1 – Chemical composition of catalysts *via* XRF, EDS, and ICP analysis.

Catalyst	XRF	EDS	ICP		
	Mg : Al : Si / mol	Mg : Al : Si / mol	Mg : Al : Si / mol	Ru /wt.%	Re /wt.%
MAS111	0.64 : 1.00 : 0.75	0.74 : 1.00 : 0.84	0.88 : 1.00 : 0.55	–	–
MAS311	3.00 : 2.00 : 1.61	3.00 : 1.64 : 1.15	3.00 : 1.34 : 1.54	–	–
MAS131	0.72 : 3.00 : 1.01	0.76 : 3.00 : 1.02	0.91 : 3.00 : 0.82	–	–
MAS113	1.17 : 1.64 : 300	1.10 : 1.35 : 3.00	1.49 : 1.40 : 3.00	–	–
0.1Ru/MAS311	–	–	3.00 : 1.26 : 0.86	0.1	–
0.1Re/MAS311	–	–	3.00 : 1.41 : 0.60	–	0.1

The discrepancies between nominal and measured values can be attributed to several factors, including those inherent to the synthesis process, such as material loss or its deposition on glassware, as well as the limitations and inherent imprecision of characterization techniques. More importantly, these deviations may arise from thermodynamic equilibrium during material synthesis, where not all cations present in the liquid phase during precipitation are fully incorporated into the solid phase. Therefore, part of the carbon is leached during the washing protocols. Nonetheless, these variations do not undermine the validity of the preparation methodology, which remains a reliable approach for synthesizing these catalysts. Furthermore, it is important to note that XRF analysis covers a larger irradiation area than EDS. Since EDS provides a localized surface analysis, it may exhibit variations across different regions of a non-homogeneous surface, whereas XRF offers a more comprehensive and representative overview of the material composition. Similarly, ICP, which quantifies elemental composition in solution after sample digestion, provides bulk measurements but may introduce slight deviations due to the complexities associated with sample preparation and dissolution. These discrepancies have been specifically reported for Si and have been attributed to the inherent challenge of achieving its complete quantitative dissolution (SZABÓ *et al.*, 2022b). These methodological differences collectively contribute to the observed disparities in the results.

It should be mentioned that traces of K were detected in all samples during the full-scan XRF analysis, as anticipated due to the use of K_2CO_3 and KOH during the precipitation of hydroxides from nitrates. Despite thorough washing procedures, residual quantities of this metal likely persist within the catalysts. However, the detected quantities

were extremely low and considered negligible relative to the primary elements. Accordingly, only the main constituents—Mg, Al, and Si—were included in the calculation of molar ratios, as the K content was insufficient to significantly influence the overall elemental composition or catalytic behavior.

4.1.2 Morphology and structure

The morphology of the non-impregnated catalysts was characterized using SEM, and the resulting images are compiled in Figure 4.1. The particles displayed a spherical aggregate structure, with small filament-like features observed on the surface.

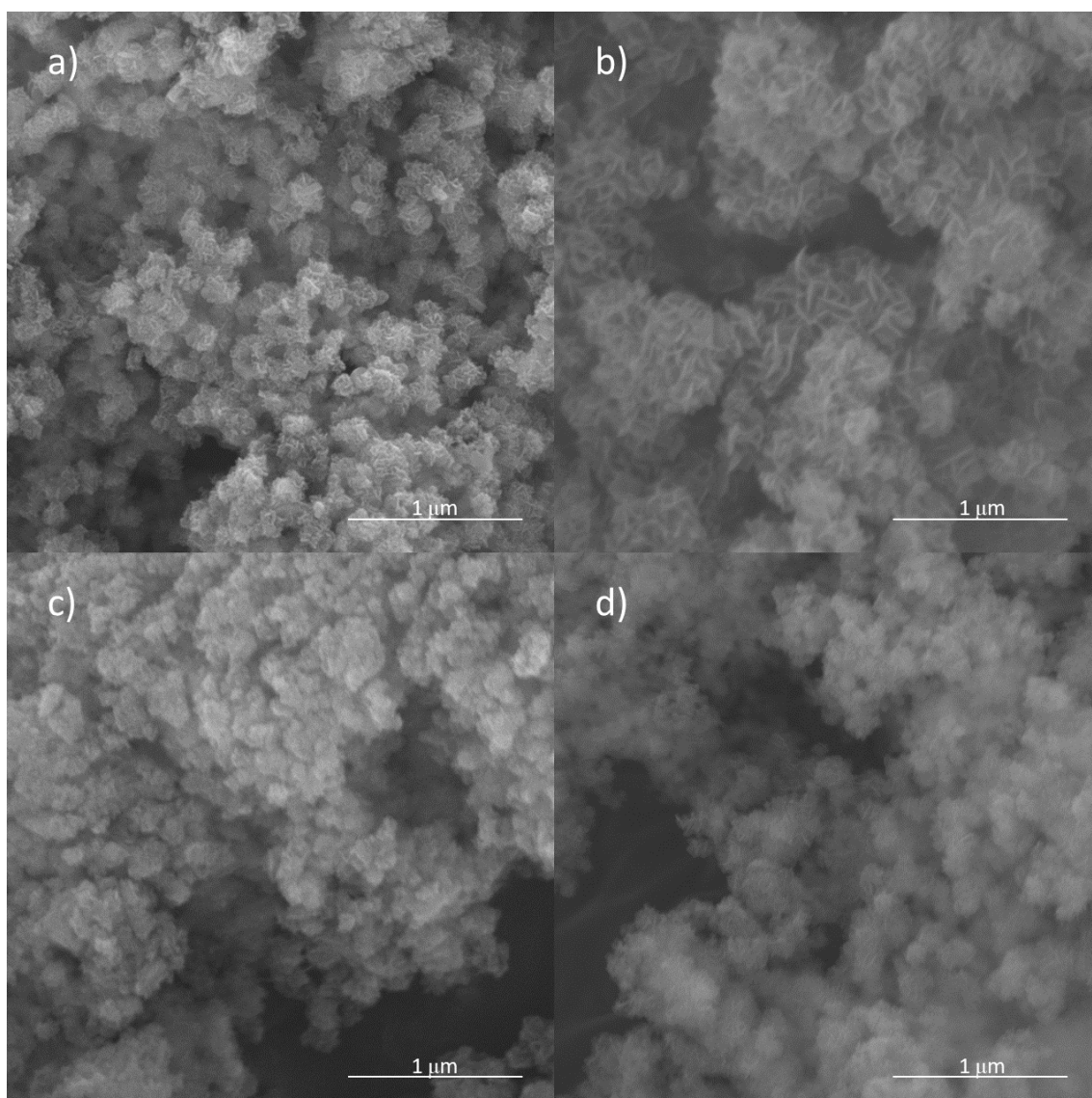


Figure 4.1 – SEM images of the catalysts: a) MAS111, b) MAS311, c) MAS131, and d) MAS113.

As expected, the incorporation of SiO₂ resulted in a spherical shape and an amorphous nature to the catalyst, a characteristic that was most pronounced in the sample with the highest Si content, MAS113 (Figure 4.1d). In the equimolar sample MAS111 (Figure 4.1a) and the sample with the highest Mg content, MAS311 (Figure 4.1b), the structure displayed filament-like features, likely representing plates or lamellae, which are commonly observed in the structures of MgO and hydrotalcites (GENNEQUIN *et al.*, 2010; RAMASAMY *et al.*, 2016b). Conversely, the sample with the highest Al content, MAS131 (Figure 4.1c), did not exhibit any organized plate or lamella structure but instead presented a cluster of rounded particles, akin to the typical morphology associated with Al₂O₃ nanoparticles (MEI *et al.*, 2018).

To assess the structural stability and decomposition behavior of the catalysts, TG and DTG curves are presented in Figure 4.2. All four samples exhibited similar decomposition behavior with the profiles revealing two distinct mass losses events: the first occurring between 300 K and 500 K, and the second within the 500 K to 700 K range. The latter was particularly pronounced for the MAS311 catalyst, whereas it appears subtly for MAS113 and is barely detectable for MAS131. The first decomposition region, characterized by overlapping peaks, corresponds to the removal of physisorbed and interlayer water (CHUNG *et al.*, 2023, 2024). The second region is attributed to the surface dehydroxylation of silica and/or hydrotalcite layers, as well as the loss of anions, ultimately leading to the collapse of the layered structure (CAVANI; TRIFIRÒ; VACCARI, 1991; ZHANG *et al.*, 2017). Notably, this decomposition event occurs at lower temperatures than those previously reported for pure hydrotalcite materials (ZHANG *et al.*, 2017), suggesting that the presence of silica might weaken the interactions between the layers and anions. The extent of mass loss within this temperature range appears to correlate with the relative Mg content in the samples (CHUNG *et al.*, 2024). Moreover, the sample with a higher Mg content exhibits the most significant weight loss compared to the other samples, pointing to a potentially greater introduction of defect sites into the oxide framework (WANG *et al.*, 2024).

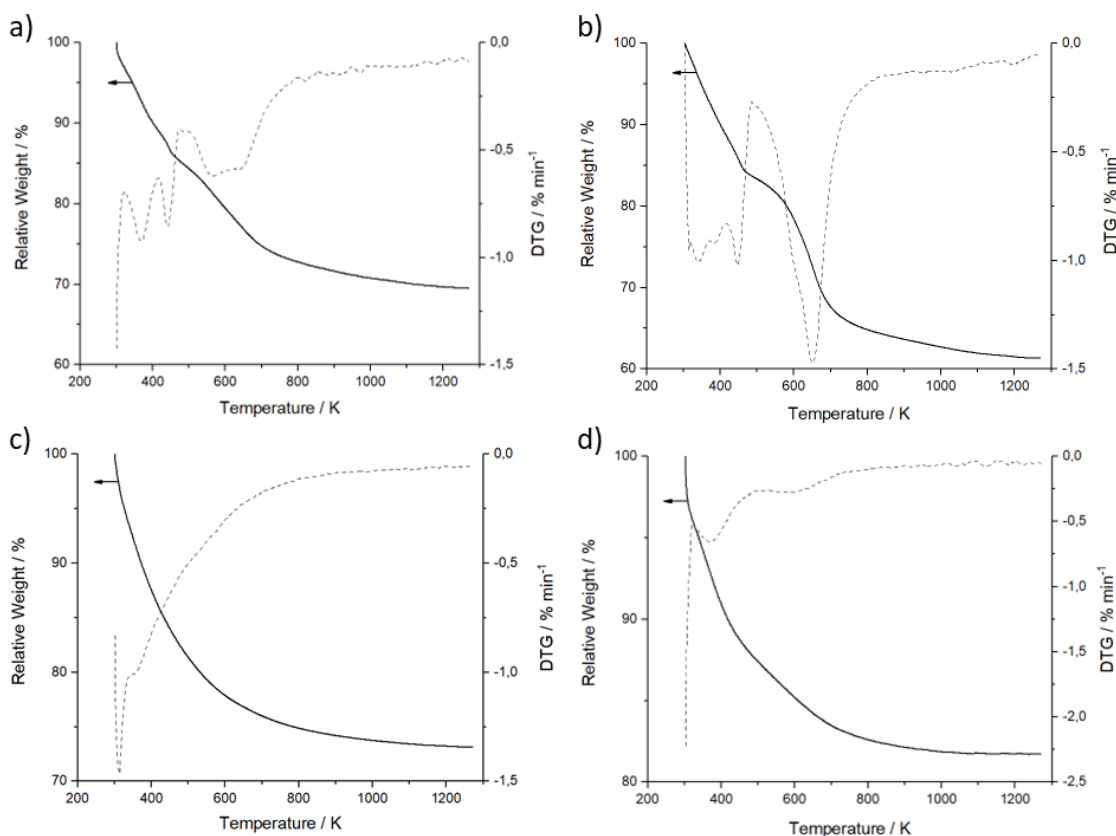


Figure 4.2 –Thermogravimetric curves and the first-derivatives of the corresponding plots for a) MAS111, b) MAS311, c) MAS131, and d) MAS113 catalysts.

4.1.3 Specific surface area

The BET surface area and porosity of the catalysts were determined *via* N₂ physisorption, with results presented in Figures 4.3 and 4.4. Analysis of the isotherms (Figure 4.3) for the different catalysts revealed no significant variations between the profiles, as all exhibited type IV isotherms, which are characteristic of mesoporous materials (SING, 1985). This observation is further corroborated by the calculated average pore size, which shows values ranging from 8 to 16 nm for all catalysts. Additionally, the narrow hysteresis loop observed for the unsupported samples is consistent with the H1-type, which is typical of materials possessing a narrow distribution of uniform cylindrical mesopores (LEOFANTI *et al.*, 1998). For the metal-containing catalysts, a subtle shift in the hysteresis loop is observed, transitioning toward an H4-type profile, typically associated with narrow slit-like micro or mesopores (SING, 1985), which may be attributed to the partial pore blockage or restructuring of the pore network induced by metal impregnation.

The surface area values clearly exhibit variation with changes in the stoichiometry of the elements. Increased content of Mg or Al in the catalysts, MAS311 and MAS131, respectively, resulted in a more than 30 % increase in specific surface area compared to the equimolar catalyst. This increase may be attributed to the formation of a greater number of pores with smaller diameters, as confirmed in Figure 4.4. In contrast, the MAS113 catalyst, with higher Si content, exhibited the lowest specific surface area among the synthesized materials. A similar trend was observed for pore volume, with MAS311 exhibiting the highest value among all samples. A reduction of approximately 20 % in surface area is observed for the materials doped with Ru or Re, a phenomenon commonly attributed to sintering induced by the thermal treatment following the incipient wetness impregnation process. This decrease is likely due to particle agglomeration and growth, which reduces the available active surface area.

The thermal decomposition of hydrotalcite-type materials into the corresponding oxide is expected to significantly enhance porosity, resulting in solids with greater specific surface area and pore volume (DI COSIMO *et al.*, 1998; MADERUELO-SOLERA *et al.*, 2023). The reduced surface area observed for the equimolar MAS111 catalyst can be attributed to a reversion from the oxide phase to the hydroxide phase, likely due to the memory effect of hydrotalcites, as confirmed by the XRD results (*vide infra*). In contrast, the substantial increase in specific surface area for MAS311 aligns with the formation of an oxide phase, wherein the thermal decomposition of hydrotalcite releases CO₂ and H₂O, creating a well-developed network of small pores that contribute to a higher surface area (DI COSIMO *et al.*, 2000). Similarly, the behavior of MAS131, the Al-rich catalyst, is consistent with literature reports, as the carbonate content—and therefore the CO₂ released during decomposition—appears proportional to the Al content (REICHLE, 1986; DI COSIMO *et al.*, 2000). The lower surface area observed for MAS113 can be attributed to the dominant SiO₂ phase and pore blockage induced by excess Si (KUMAR *et al.*, 2022).

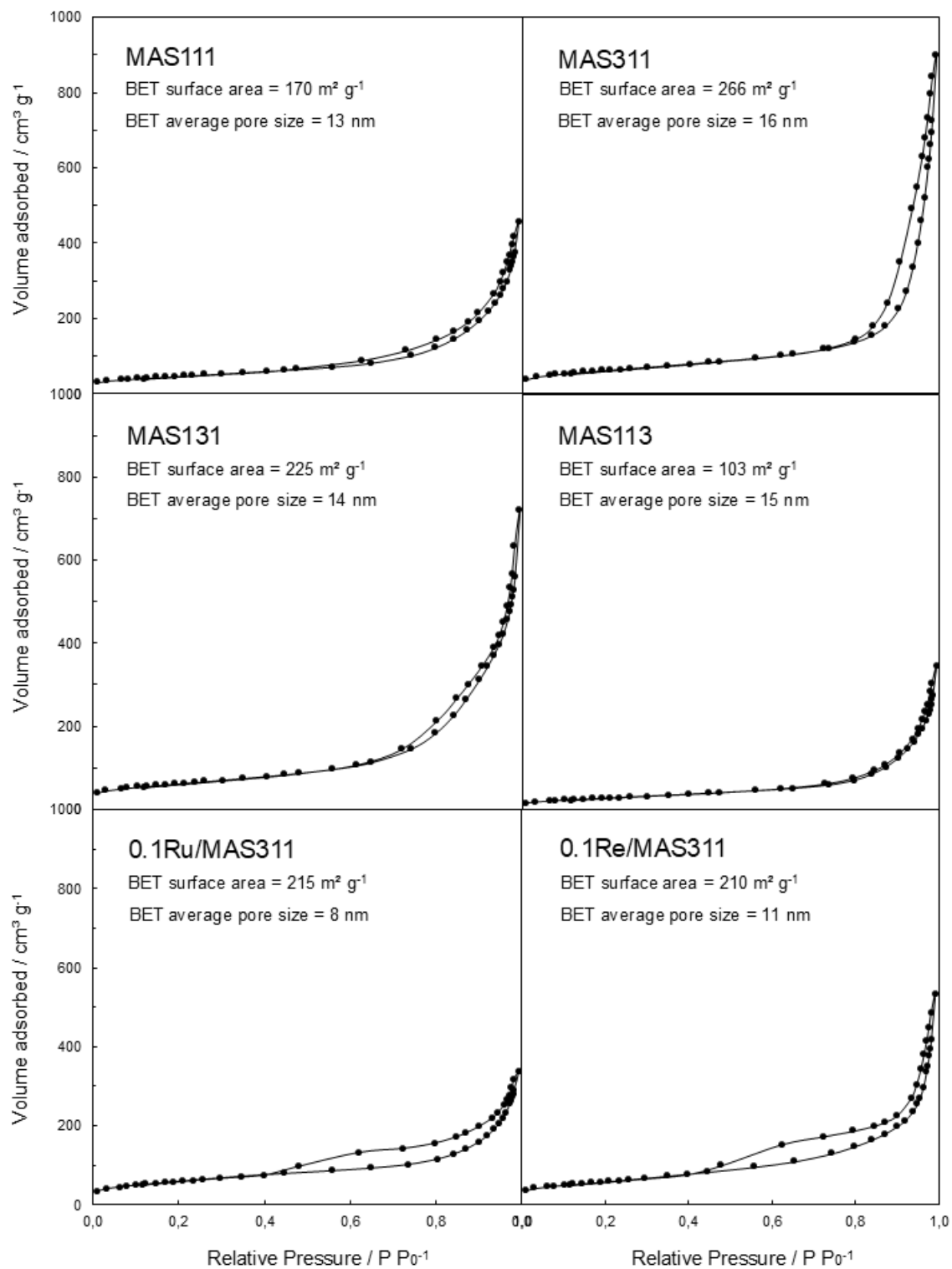


Figure 4.3 – N₂ adsorption and desorption isotherms of the catalysts.

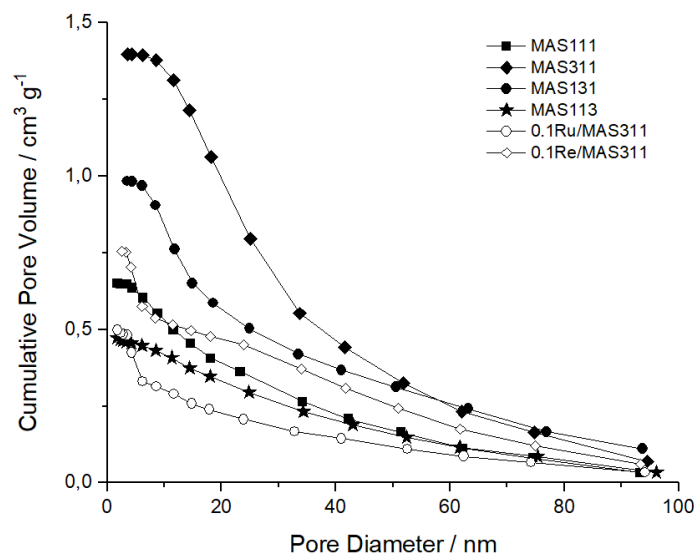


Figure 4.4 – N₂ physisorption cumulative pore size distribution results.

4.1.4 Crystallographic analysis

Conventional *ex situ* XRD patterns for the synthesized catalysts are presented in Figure 4.5. The equimolar sample, MAS111, exhibited several low-intensity peaks characteristic of hydrotalcite-like phases (JCPDS 14-0191). In contrast, the MAS311 sample, with the highest Mg content, displayed only two relatively broad peaks at 43.0° and 62.3°, corresponding to the (200) and (220) planes of MgO (JCPDS 01-1235), indicating the formation of a highly dispersed or poorly crystalline MgO phase. The MAS113 catalyst displayed low crystallinity, with a broadened peak at 26.6°, suggesting the presence of an amorphous or partially ordered phase. Meanwhile, the sample with the highest Al content, MAS131, did not exhibit any distinct diffraction peaks, implying the absence of long-range crystalline order. The MAS311 catalyst, impregnated with a 0.1 % mass fraction of Ru or Re, exhibited two intense main diffraction peaks at 43.0° and 62.3°, also present at the non-impregnated material, along with a broader, low-intensity peak at 79.1°, all of which correspond to the periclase phase of MgO (JCPDS 01-1235). Additionally, a low-intensity peak associated with the (005) phase of hydrotalcite (JCPDS 14-0191) was also observed.

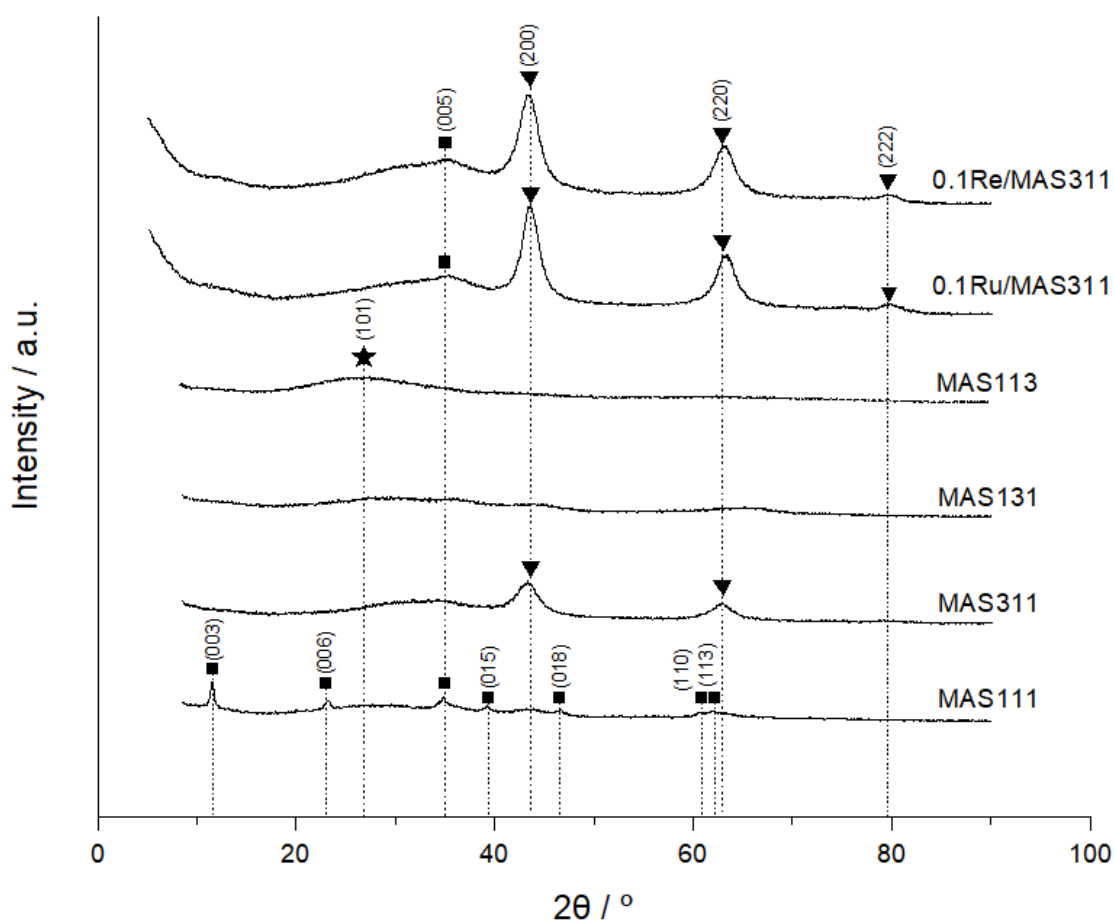


Figure 4.5 – X-ray diffractograms of the catalysts. Offsets were inserted for clarity.

■: Hydrotalcite (JCPDS 14-0191), ▼: MgO, periclase (JCPDS 01-1235), ★: SiO₂ (JCPDS 33-11-61).

To confirm that the oxides originate from a hydrotalcite-like structure, XRD analysis was conducted on a sample before its thermal decomposition into the corresponding oxides, as shown in Figure 4.6. The results validate the presence of diffraction peaks characteristic of hydrotalcite (JCPDS No. 14-0191). An important characteristic of hydrotalcite-derived materials is their ability to regenerate their original structure upon the oxide's interaction with atmospheric water and carbonates, a phenomenon known as the memory effect. This process leads to the formation of hydrated aluminum and magnesium hydroxides, specifically a hydrotalcite-like structure intercalated with hydroxyl (OH⁻) or carbonate (CO₃²⁻) ions as charge-compensating species within the interlayer region (Figure 4.7) (TICHIT; COQ, 2003). This phenomenon could account for the presence of diffraction peaks corresponding to hydrotalcite planes

(JCPDS 14-0191) observed in the MAS111 sample, suggesting that atmospheric exposure may have facilitated the partial reformation of the hydrotalcite structure.

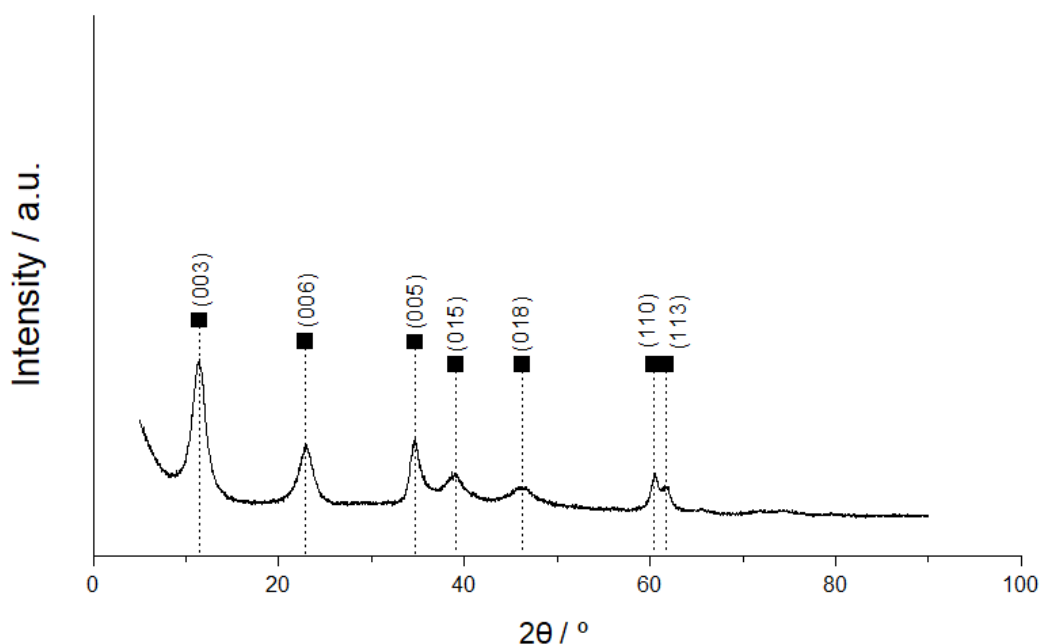


Figure 4.6 – X-ray diffractograms of one of the samples prior to the thermal treatment showing peaks of hydrotalcite (JCPDS 14-0191).

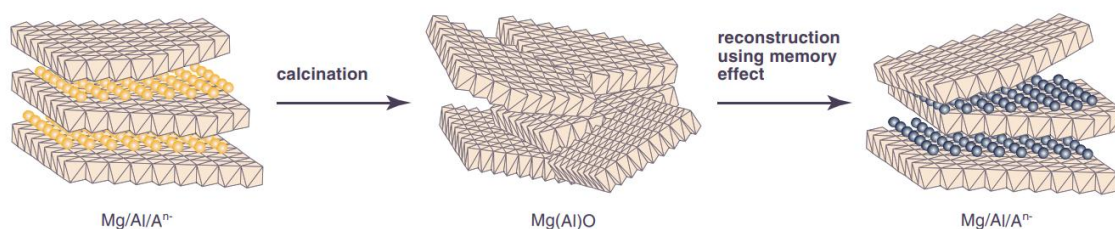


Figure 4.7 – Simplified representation of the rehydration of Mg–Al oxides (TICHIT; COQ, 2003).

The amorphous nature of the samples is further corroborated by the low crystallinity observed in all the diffractograms, as evidenced by the broad, low-intensity peaks with reduced resolution. The MAS311 catalyst showed diffraction peaks corresponding to the cubic planes of MgO periclase; however, no distinct phase associated to Al was identified. This observation suggests that the materials may exist as solid solutions in which Al is incorporated into a MgO-like lattice structure (KUŚTROWSKI *et al.*, 2004). Alternatively, it may indicate that Al-containing species are either well-dispersed or present in an amorphous phase, a phenomenon commonly

observed when the Mg/Al ratio exceeds 1 (LEÓN; DÍAZ; ORDÓÑEZ, 2011; RAMASAMY *et al.*, 2016b). The MAS113 sample, characterized by the highest Si content, exhibited low crystallinity, with a broad peak at 26.6° , indicative of amorphous SiO_2 (JCPDS 33-11-61). In contrast, the MAS131 catalyst did not display any discernible diffraction peaks, suggesting the absence of a crystalline phase or any long-range structural order in this sample. The absence of diffraction peaks associated with Ru or Re in the metal-containing materials suggests that the Ru phase in 0.1Ru/MAS311 and the Re phase in 0.1Re/MAS311 catalysts are present in a nanocrystalline state, lacking long-range structural order. This implies that the metal nanoparticles are below the limit of detection of the equipment, as their characteristic signals would be indistinguishable from background noise.

The *in situ* and *operando* XRD patterns are presented in Figures 4.8 and 4.9. Figure 4.8 illustrates the structural evolution of the material throughout the pretreatment and reaction, displaying all collected patterns. In contrast, Figure 4.9 provides a comparative view of the initial and final states of the samples by presenting only the first (prior to pretreatment) and the last patterns (post-reaction), enhancing clarity and facilitating direct evaluation of structural changes. The peaks observed at 2.3° and 10.7° are artifacts of the instrumentation and are therefore excluded from further analysis and discussion. Moreover, the angles presented here correspond to half of the values associated with the *ex situ* XRD analysis previously discussed (Figure 4.5).

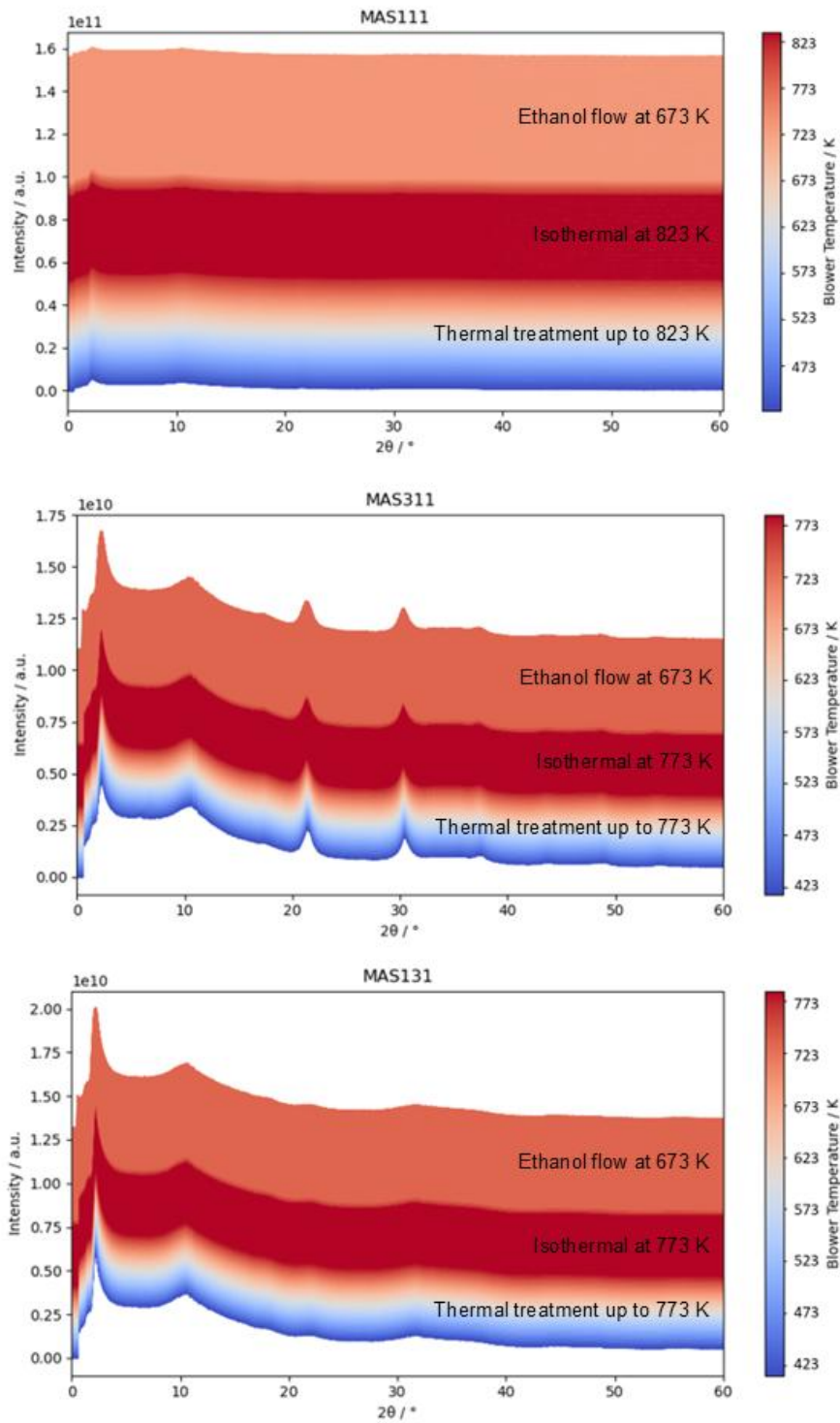


Figure 4.8 – *In situ* and *operando* XRD of the samples (MAS111, MAS311, MAS131).

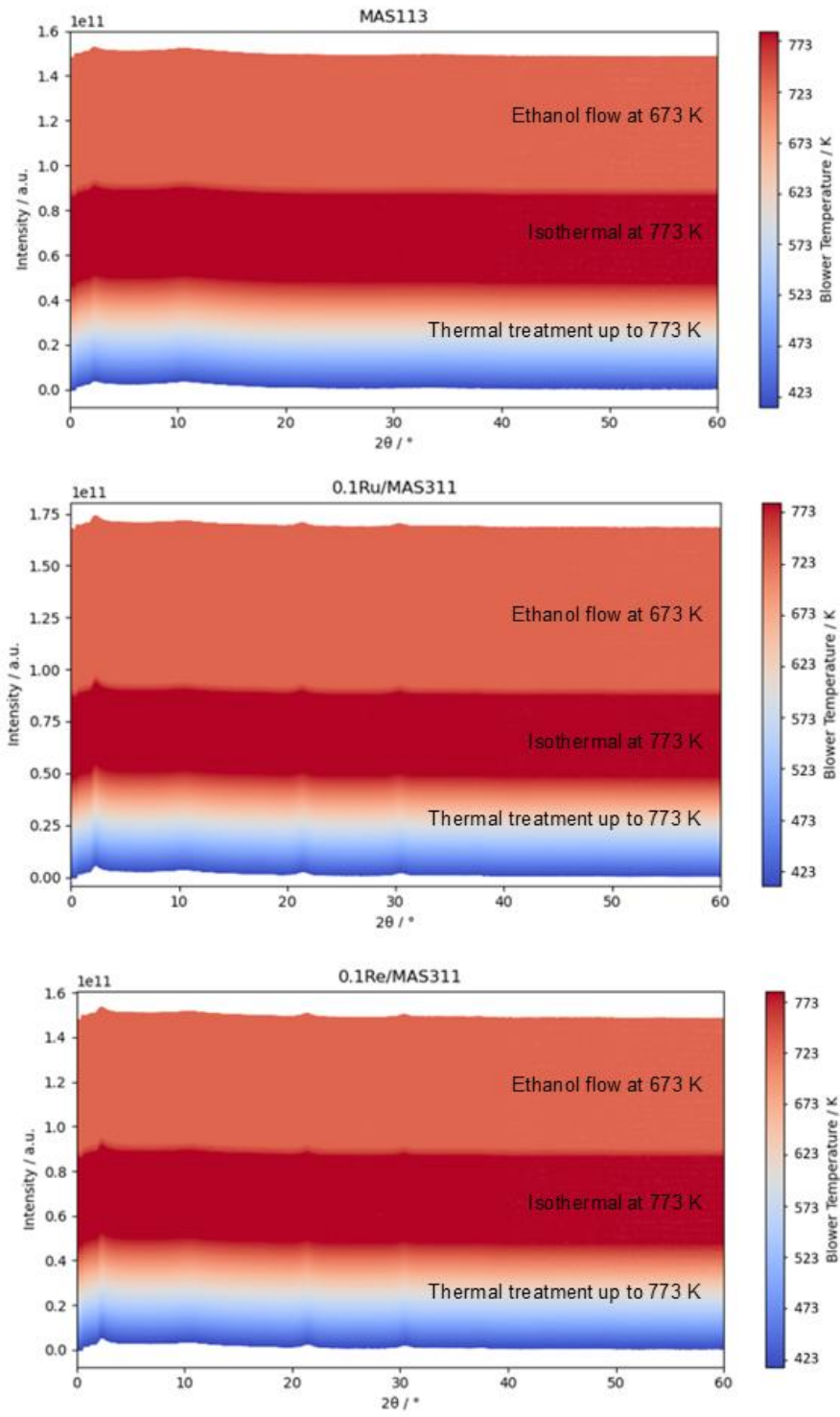


Figure 4.8 (cont.) – *In situ* and *operando* XRD of the samples (MAS113, 0.1Ru/MAS311, 0.1Re/MAS311).

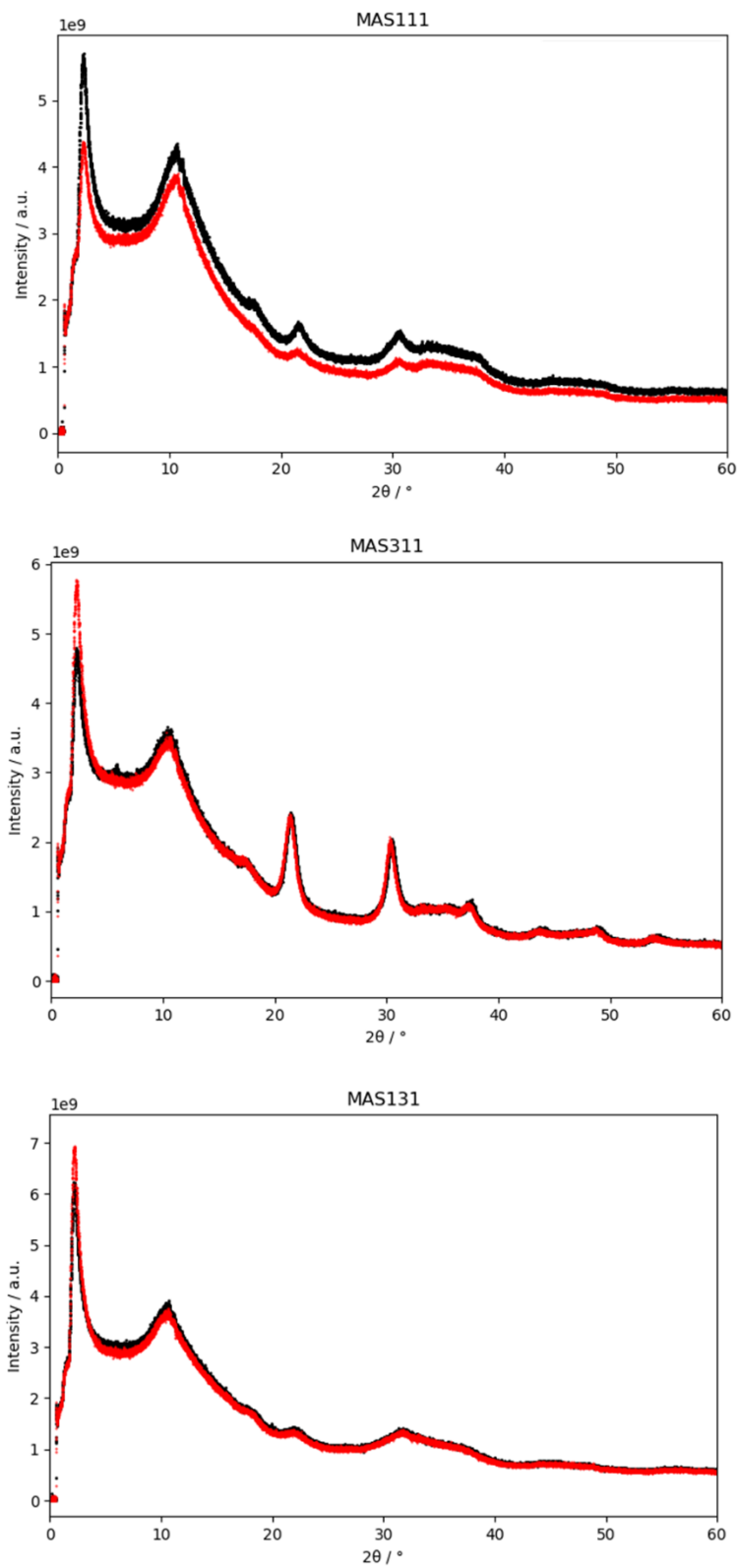


Figure 4.9 – Initial (black line) and final (red line) XRD patterns of the samples (MAS111, MAS311, MAS131).

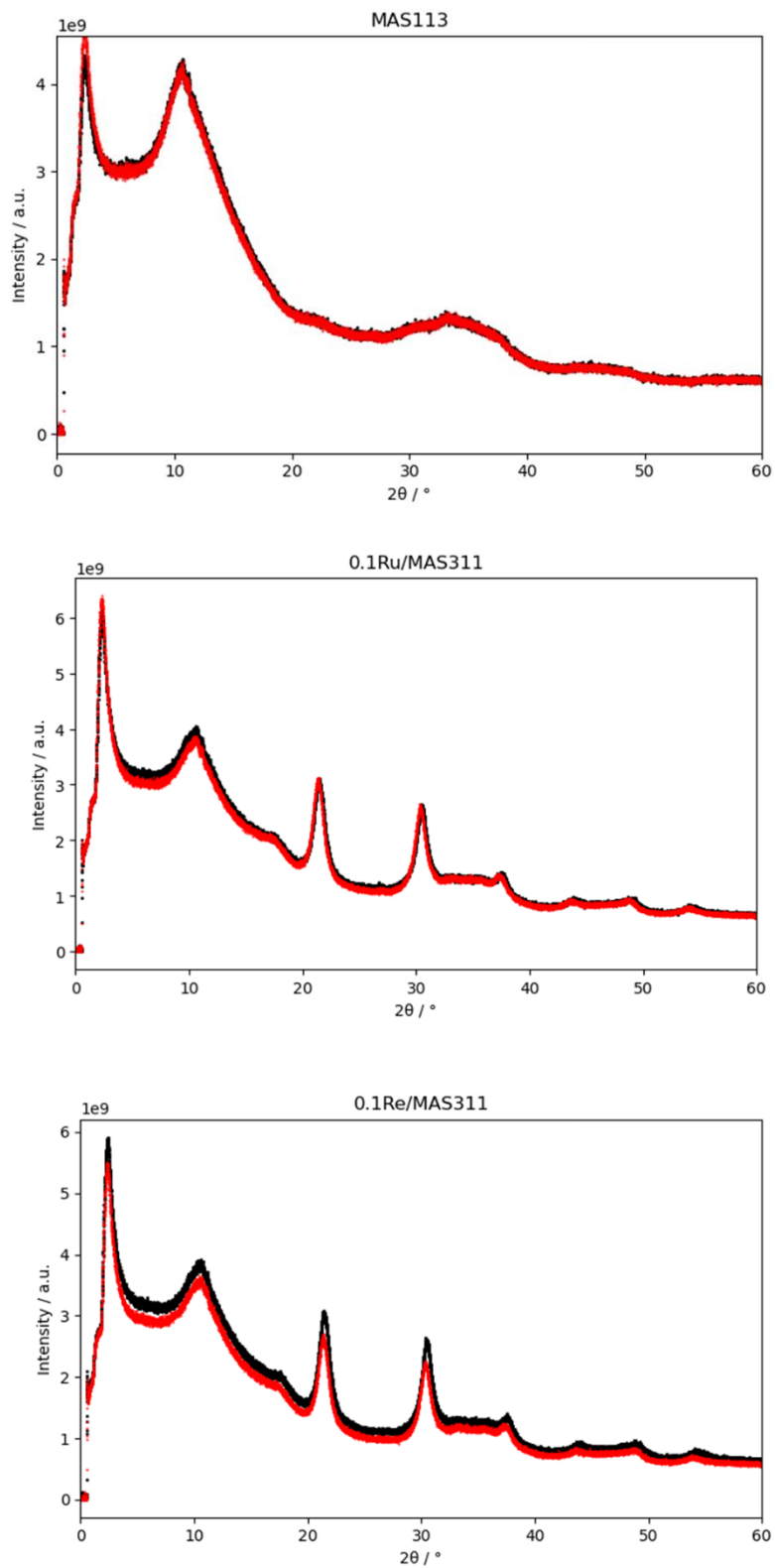


Figure 4.9 (cont.) – Initial (black line) and final (red line) XRD patterns of the samples (MAS311, 0.1Ru/MAS311, 0.1Re/MAS311).

The XRD patterns of the MAS111 catalyst exhibited two primary reflections corresponding to the (200) and (220) planes of periclase MgO (JCPDS 001-1235) at 21.5 ° and 31.1 °, respectively. Additionally, a weaker reflection at 34.7 ° was observed, which can be attributed to the (009) plane of hydrotalcite (JCPDS 014-0191). In the case of MAS311, alongside the (009) reflection of hydrotalcite and the intensified MgO-associated peaks, an additional peak at approximately 55° was detected, corresponding to the (420) plane of MgO. Furthermore, less intense reflections at 37.6 °, 44.3 °, and 49.2 ° were identified, which can be assigned to the (521), (242), and (171) planes of mullite-type aluminum silicates (JCPDS 015-0776), respectively. The MAS131 catalyst exhibited the same diffraction peaks as MAS111; however, they appeared significantly broadened, suggesting a reduction in long-range crystallinity. In contrast, MAS113 displayed an entirely amorphous phase, with no discernible crystalline reflections. The metal-containing catalysts exhibited diffraction patterns identical to those of MAS311, with no observable peaks corresponding to the metal phase, indicating a high degree of dispersion or possible incorporation into the support matrix.

Among all materials, MAS111 was the only catalyst that exhibited noticeable differences between its pre- and post-reaction XRD patterns (Figure 4.9). The post-reaction pattern displayed a reduction in crystallinity, which may be attributed to partial structural degradation, likely due to thermal-induced phase transformations, leaching of active sites, or catalyst-support interactions, or coke deposition on the surface, which can hinder the interpretation of diffraction peaks and contribute to catalyst deactivation.

It is important to note that while post-reaction *ex situ* XRD analysis can provide structural insights, a more detailed understanding of the transformation pathways and their impact on catalytic performance would require *operando* characterization. To the best of our knowledge, this is the first report of such real-time crystallographic changes occurring under ethanol upgrading conditions in hydrotalcite-derived catalysts. This previously unreported observation provides direct, time-resolved evidence of structural instability, distinguishing MAS111 from the other materials, which maintained stable diffraction patterns with no significant variation in peak position, intensity, or broadening throughout the reaction; moreover, no coke or otherwise carbon-related phases could be observed, at least within the time frame of the analysis conducted in this work. While these findings confirm the high thermal and chemical stability of the other catalysts, the exact origin of deactivation in MAS111 remains unclear. Similar materials reported in

the literature have exhibited catalytic deactivation, yet often without any identified correlation to crystallographic changes (TAIFAN *et al.*, 2019; ZHANG *et al.*, 2020; CUELLO-PENALOZA *et al.*, 2022)—raising the possibility that processes such as amorphous carbon deposition or hydroxylation of active sites may play a role. These processes may not lead to detectable structural changes in conventional XRD patterns, further highlighting the importance of *operando* techniques in capturing subtle but catalytically significant transformations. Finally, it is also relevant to highlight that given the scant time to conduct experiments at a synchrotron facility, longer time-on-stream (TOS) could further shed light onto this behavior.

4.1.5 Surface acidity and basicity

The TPD analyses utilizing NH_3 and CO_2 as probe molecules enabled the identification and estimated quantitative assessment of the accessible acidic and basic sites, respectively, on the catalyst surfaces. The integrated peak areas provided an approximate quantification of the site densities, while the desorption profiles offered insights into the strength distribution of these sites. A higher desorption temperature indicates stronger interaction between the probe molecules and the active surface sites. The NH_3 and CO_2 desorption profiles for the non-impregnated materials are presented in Figure 4.10.

Additionally, to evaluate the influence of pretreatment temperature on the acidity and basicity of the catalysts, the CO_2 - and NH_3 -TPD profiles for samples pretreated at 623 K are presented in Figure 4.11 to be compared with those obtained for 773 K (Figure 4.10).

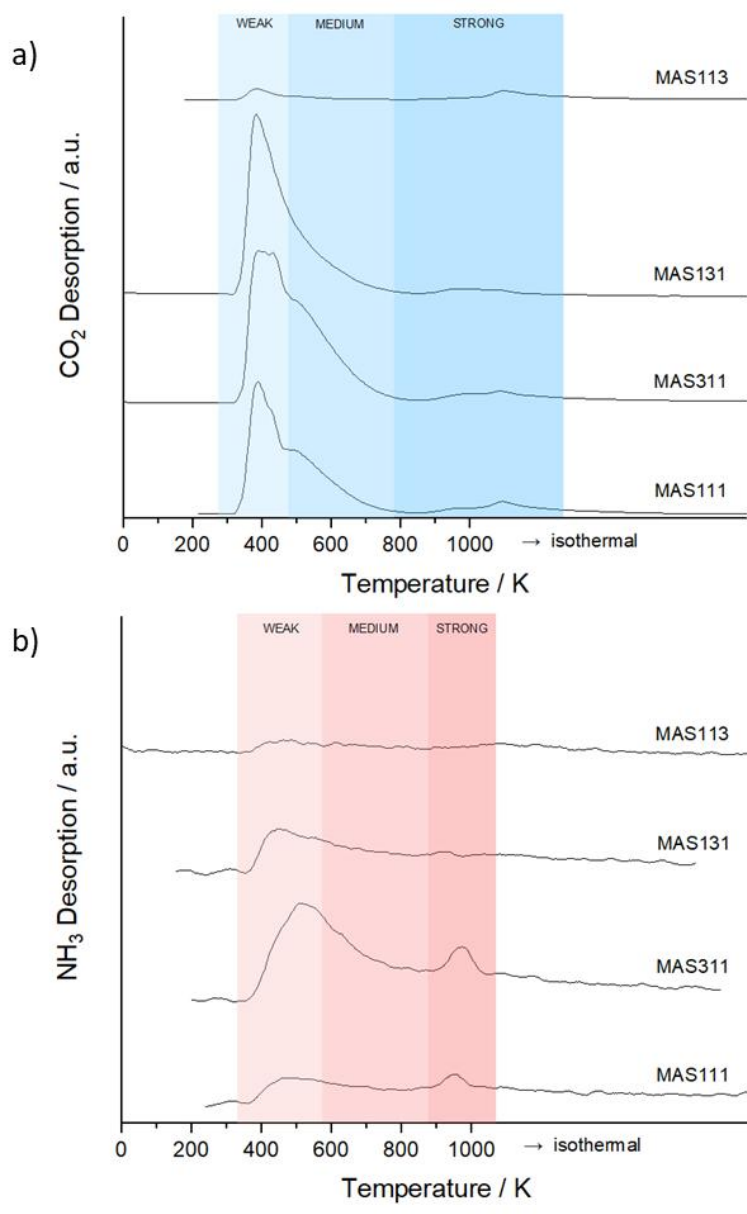


Figure 4.10 – Desorption profiles of a) CO₂ and b) NH₃ for catalysts pretreated at 773 K.

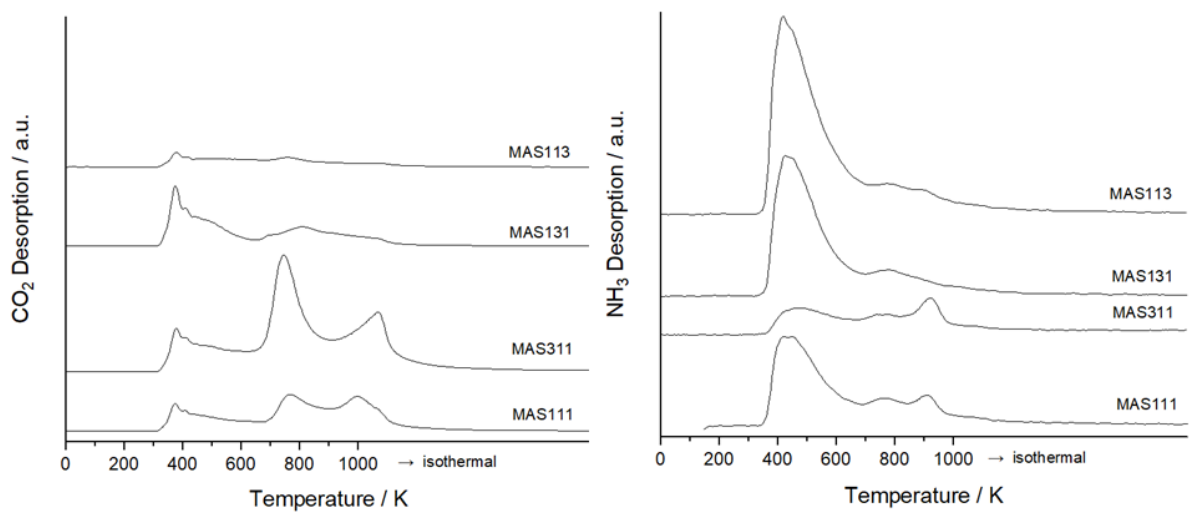


Figure 4.11 – Desorption profiles of a) CO₂ and b) NH₃ for catalysts pretreated at 623 K.

A distinct contrast is observed between the desorption profiles of the samples treated at 623 K (Figure 4.11) and 773 K (Figure 4.10). For the latter, CO₂ desorption predominantly occurs at relatively low temperatures (300 K – 800 K), whereas the sample pretreated at 623 K exhibits a broader desorption distribution. In the case of the NH₃-TPD profiles, a notable discrepancy is evident in the intensity of the observed peaks. These results indicate that differences in pretreatment conditions leads to variability in the density and strength of the acidic and basic sites. Kuśtrowski *et al.* observed similar trends in their analysis of the influence of thermal treatment conditions on hydrotalcite-derived Mg–Al oxides (KUŚTROWSKI *et al.*, 2004). The CO₂ desorption profiles of the samples thermally treated at 723 K exhibited two prominent peaks, whereas in the samples treated at 823 K, the basicity associated with OH surface groups, which correspond to the low-temperature desorption peak, became more pronounced. This suggests that the decomposition of NO₃⁻ anions during thermal treatment may promote the formation of Brønsted basic sites. Understanding the nature and strength of acidic and basic sites is paramount, as these sites govern the catalytic pathways of Guerbet and Lebedev reactions (*vide supra*). Previous studies often highlight the tuning of acid-to-base site ratio in hydrotalcites and hydrotalcite-derived oxides through controlled mass fraction adjustments during synthesis; nonetheless, the results presented in Figures 4.10 and 4.11 demonstrate that thermal treatment also plays a significant role in shaping the chemical environment of the catalyst surface in the examined ternary systems. Beyond influencing the total number of active sites, thermal treatment critically alters their relative distribution with respect to site strength, further impacting catalytic performance.

Since the catalysts undergo thermal treatment at 773 K prior to reaction, the discussion will further focus on the insights derived from the desorption profiles in Figure 4.10. Literature reports indicate that CO₂ desorption is generally observed around 373 K and 573 K, associated with weak and strong basic sites, respectively, while NH₃ desorption typically occurs at approximately 373 K and 473 K, corresponding to weak and medium-strength acidic sites (DI COSIMO *et al.*, 2000; RAMASAMY *et al.*, 2016b; SAMSUDIN; JAENICKE; CHUAH, 2023). However, the quantitative analysis of TPD results is inherently influenced by discretionary choices made by the experimenter, as the threshold definitions for weak, medium, and strong sites are ultimately arbitrary and often inconsistent across studies. Moreover, the experimental conditions in this study permitted higher desorption temperatures than those commonly reported, and the material itself is

novel, making direct benchmarking challenging. Furthermore, the conventional approach of peak deconvolution is not always applicable and frequently yields phenomenologically unreasonable results, as observed in this study, due to the intrinsic mathematical limitations of splining and peak-fitting algorithms. In the studied cases, the obtained profiles were classified into three regions to represent the relative strength of the adsorption sites. For CO₂-TPD analysis, weak, medium, and strong basic sites are defined within the temperature ranges of 273 K – 473 K, 473 K – 773 K, and above 773 K, respectively. Similarly, for NH₃-TPD, weak, medium, and strong acid sites correspond to the intervals 323 K – 573 K, 573 K – 873 K, and 873 K – 1073 K, respectively. These temperature regions were also applied to the metal-containing materials, as depicted in Figure 4.12. The quantitative data, normalized by the specific surface area determined *via* the BET method, for all catalysts—including the impregnated samples—is summarized in Table 4.2 and Figure 4.12.

The CO₂ desorption profiles of the oxides (Figure 4.10a) indicate a predominance of desorption events in the first and second regions, corresponding to weak and medium basic sites, respectively, across all samples except MAS113, which exhibits consistently low-intensity peaks throughout all regions. For the metal-containing catalysts (Figure 4.12a), the emergence of a desorption peak in the strong basic sites region is observed. Notably, the NH₃ desorption profiles (Figure 4.10b) reveal that all samples exhibit more pronounced desorption peaks associated with weak and medium acid sites region. In the case of 0.1Ru/MAS311 and 0.1Re/MAS311 (Figure 4.12b), a reduction in peak intensity is observed within the strong acid sites region relative to the unsupported MAS311 (Figure 4.10b). Conversely, within the weak and medium acid sites region, Ru incorporation leads to a decrease in peak intensity, whereas Re promotes an increase.

When evaluating the basic-to-acid site ratio (Figure 4.13), MAS113 exhibits the highest value among the unsupported catalysts (2.86), despite having the lowest total site density, 0.93 (Table 4.2). The other unsupported catalysts display comparable basic-to-acid ratio values, ranging from 1.22 to 1.54, with MAS311 exhibiting the highest basic site density (1.82). The introduction of metal species to MAS311 leads to a reduction in the density of both acidic and basic sites, in the case of 0.1Ru/MAS311. This decrease is likely attributed to partial steric hindrance arising from metal deposition on the support surface, which may limit the accessibility of probe molecules (PACHECO *et al.*, 2019). Conversely, an increase in the density of acidic sites, particularly weak acid sites, is

observed for 0.1Re/MAS311. The addition of Re as a dopant in oxide supports is known to promote the formation of Lewis acid sites (LUO; LIANG, 2024b). Both Ru- and Re-modified catalysts exhibit an overall decrease in total site density, as well as a reduction in the basic-to-acid site ratio.

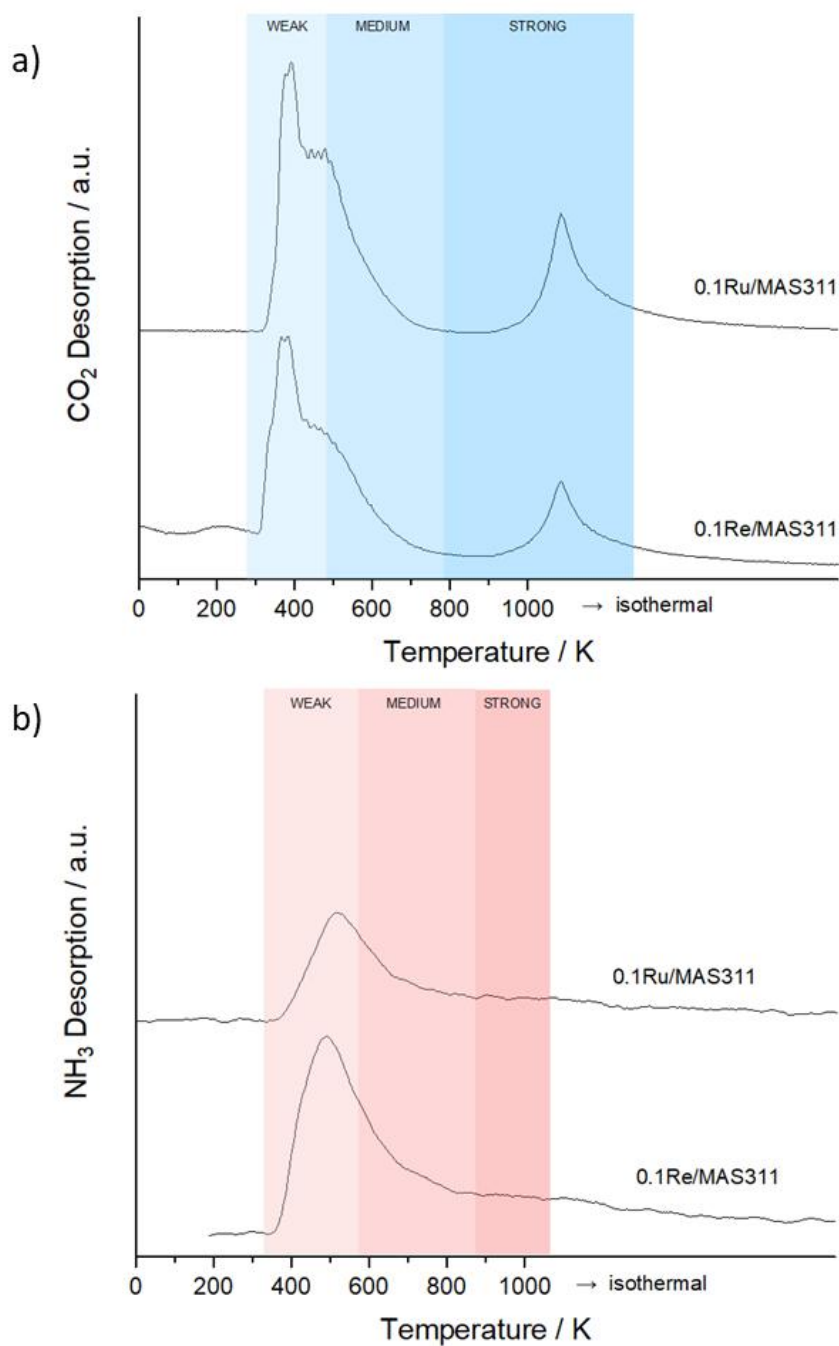


Figure 4.12 – Desorption profiles of a) CO₂ and b) NH₃ for 0.1Ru/MAS311 and 0.1Re/MAS311.

Table 4.2 – Quantification of acid and basic sites by NH₃- and CO₂-TPD.

Catalyst	Total acid site density / $\mu\text{mol m}^{-2}$	Total basic site density / $\mu\text{mol m}^{-2}$	Total site density / $\mu\text{mol m}^{-2}$	Basic-to-acid sites ratio
MAS111	1.36	1.71	3.07	1.26
MAS311	1.49	1.82	3.31	1.22
MAS131	1.16	1.79	2.95	1.54
MAS113	0.24	0.69	0.93	2.86
0.1Ru/MAS311	1.03	0.97	2.00	0.95
0.1Re/MAS311	1.62	0.69	2.31	0.43

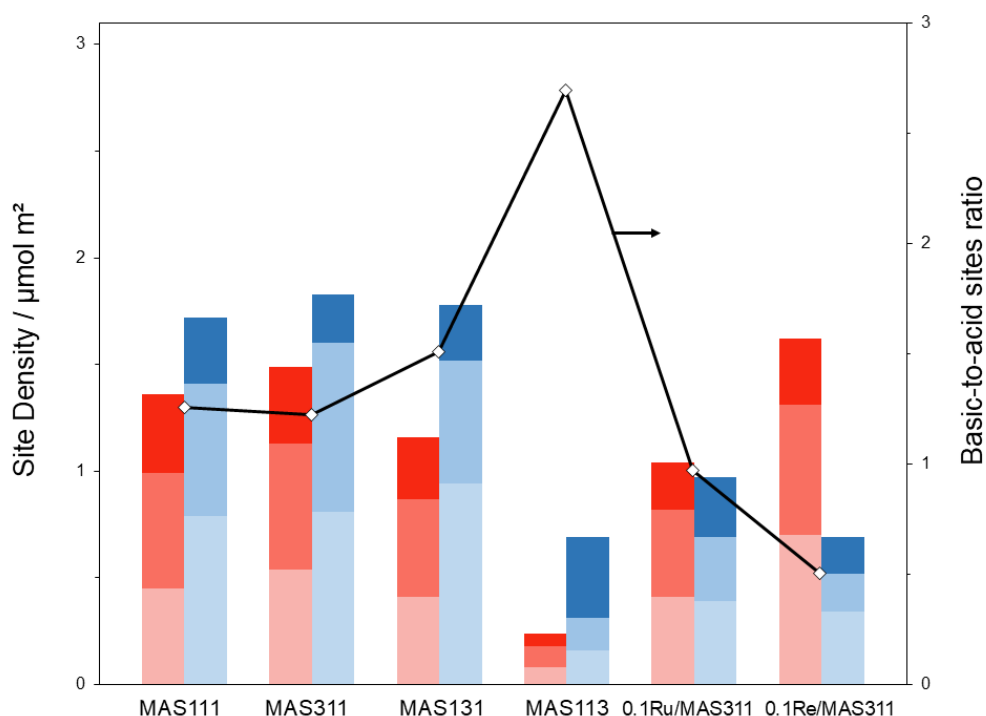


Figure 4.13 – Acid and basic sites density and correlation between them. ■ Weak, ■ medium and ■ strong acid sites; ■ weak, ■ medium and ■ strong basic sites.

Using CO₂-TPD, chemisorption, and XPS techniques, Di Cosimo *et al.* (DI COSIMO *et al.*, 2000) investigated the influence of Al content on the basicity of Mg–Al mixed oxides. Their findings indicate that, in Al-rich samples, phase segregation due to surface coverage results in a reduction in the density of basic sites as the Al content increases. This trend, however, is not evident when comparing the MAS111 and MAS131 samples, which exhibit total basic site density of 1.71 $\mu\text{mol m}^{-2}$ and 1.79 $\mu\text{mol m}^{-2}$. As expected, a higher Mg content enhances the basicity of the catalyst, as reflected in the

increased total basic site density ($1.82 \mu\text{mol m}^{-2}$). Conversely, the material with the highest Si content demonstrates the lowest basic site density ($0.69 \mu\text{mol m}^{-2}$).

Three distinct carbonate species can adsorb onto Mg_xAlO_y surfaces at basic sites with varying structures and strengths (DI COSIMO *et al.*, 2000; BOLOGNINI *et al.*, 2002; SILVA *et al.*, 2010). Bicarbonates form on weakly basic OH groups, bidentate carbonates adsorb on pairs of Mg–O and Al–O sites containing accessible cations, and unidentified carbonates adsorb on strongly basic O^{2-} anions. As the Al content increases, the relative concentration of surface OH groups and Mg–O pairs in Mg_xAlO_y also increases, leading to a reduction in the average basic site strength. This trend is evident in the CO_2 desorption profile of MAS131, where the highest intensity peak appears in the first temperature range (Figure 4.10a). The MAS113 catalyst, which has the highest Si content, exhibits weaker basicity than the other samples. Literature suggests that the total concentration of basic sites in Mg–Al–Si systems is governed by factors beyond the relative abundance of SiO_2 and Mg_xAlO_y phases. The accessibility and potential obstruction of active sites also play a critical role, making a direct correlation with the $\text{Si}/(\text{Si} + \text{Mg} + \text{Al})$ ratio unreliable (KONDRATOWICZ *et al.*, 2022). This complexity is exemplified by the findings of Čapek *et al.* (KONDRATOWICZ *et al.*, 2022), who investigated a core–shell system composed of SiO_2 and Mg–Al layered double hydroxides. In a material with the highest Si content [$\text{Si}/(\text{Si} + \text{Mg} + \text{Al}) = 0.54$, as determined by SEM-EDS], the concentration of basic sites measured by CO_2 -TPD was $108 \mu\text{mol g}_{\text{cat}}^{-1}$. Upon partial Si removal, decreasing the $\text{Si}/(\text{Si} + \text{Mg} + \text{Al})$ ratio to 0.47, the basic site concentration significantly declined to $65 \mu\text{mol g}_{\text{cat}}^{-1}$. However, when the ratio was further reduced to 0.11, the basic site concentration increased to $153 \mu\text{mol g}_{\text{cat}}^{-1}$, the highest value observed.

For the metal-containing catalysts, a notable decrease in basicity is observed, particularly within the range of weak to medium basic sites. This decline can be primarily attributed to the deposition of the metal onto the surface or within the pore structure of the support (PACHECO *et al.*, 2019), which may lead to partial blockage or neutralization of surface basic sites. Such deposition is further supported by the observed reduction in specific surface area following metal impregnation (see Section 4.1.3)

Previous studies on NH_3 desorption from Mg–Al mixed oxides have demonstrated that these materials possess both Brønsted and Lewis acid sites (SHEN; TU; HU, 1998). The Lewis acidity is attributed to Al–O–Mg species within the MgO framework, where

Al^{3+} cations predominantly occupy octahedral coordination sites. The interaction of NH_3 with Lewis acid sites is stronger than with Brønsted acid sites, as it involves coordination of a lone electron pair with the Mg and Al cations. Low-intensity desorption peaks within the strong acid site region are observed for MAS111 and MAS311 (Figure 4.10b), indicating a limited presence of strong acidic sites. Brønsted acid sites, which arise from hydroxyl groups capable of donating protons to adsorbed species, are distinctly identified in the low-temperature range across all catalysts. Furthermore, the incorporation of Al into the catalyst framework is well-documented to promote the formation of Lewis acid sites of relatively weak strength (VISHWANATHAN *et al.*, 2007). The ternary coordination at the Mg, Al, and Si interface, facilitated by partially activated O anions from surface silanol species, can induce deviations from the typical octahedral coordination of Al. This structural modification promotes the formation and enrichment of acid sites, specifically Al–O–Si and Al–O–Mg, which contribute to the overall acidity of the catalyst (KUMAR *et al.*, 2022).

The supported catalysts exhibited contrasting trends in acid site densities, depending on the metal incorporated. The 0.1Ru/MAS311 catalyst demonstrates a decrease in acidity, which may result from site blockage due to interactions between the Ru species and the support, thereby reducing access to acidic domains (QUESADA *et al.*, 2018a). In contrast, the 0.1Re/MAS311 catalyst shows an increase in acid site density. This enhancement could be attributed to the well-dispersed ReO_x species on the oxide support, which may facilitate the formation of oxygen-bridged $\text{Re}^{n+}\text{--O--M}^{\delta+}$ structures (where M represents a metal). As a result, the metal ions (Re^{n+}) contribute to the formation of Lewis acid sites, while the Re species with higher valencies (Re^{6+} and Re^{7+}) may enhance surface Brønsted acidity by attracting hydroxyl groups (LUO; LIANG, 2024a).

4.1.6 Reduction profile

The thermal profile of the reduction by H_2 for the metal-containing catalysts are illustrated in Figure 4.14. Due to the low metal content in these materials, the curves observed in this study exhibit subtle features, requiring a careful analysis for accurate interpretation. The reduction profile of 0.1Ru/MAS311 displays three small distinct peaks at approximately 340 K, 440 K, and 520 K, whereas 0.1Re/MAS311 displays two broad peaks centered at around 700 K and 870 K.

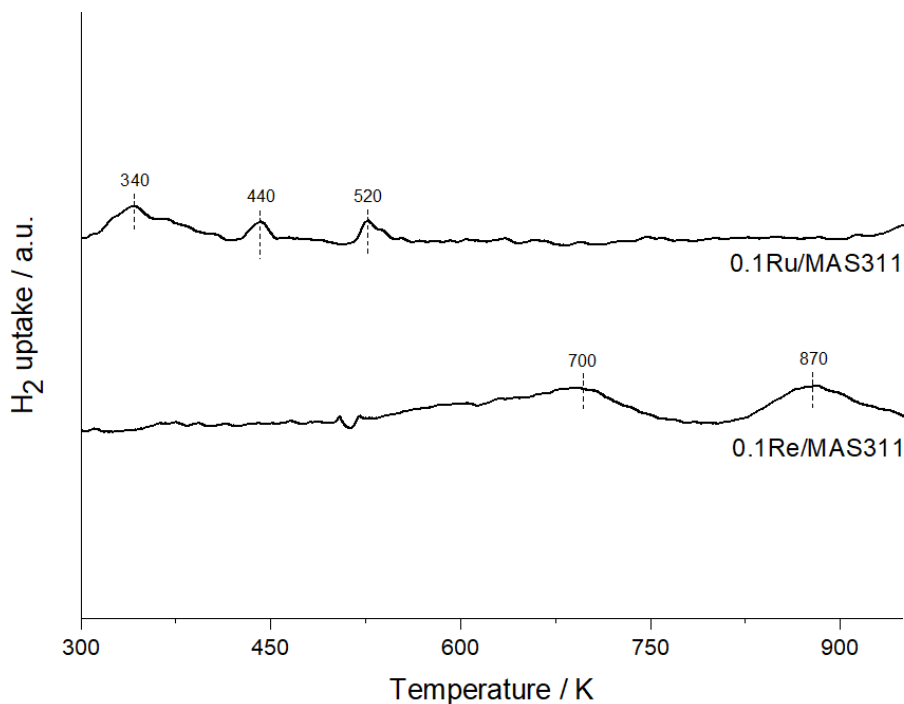


Figure 4.14 – TPR results for the metal-containing catalysts. Offsets were added for clarity.

The interpretation of these reduction features is challenging due to the limited literature available on Ru- and Re-containing materials, particularly when these metals are deposited in such low loadings and on this specific oxide support. To aid the understanding of the observed reduction behavior, comparisons with diverse catalytic systems were considered. For 0.1Ru/MAS311, the low-temperature peaks are typically attributed to the reduction of well-dispersed RuO_x species, whereas the peak at 520 K is indicative of the reduction of bulk RuO_2 (BETANCOURT *et al.*, 1998; BALLARINI *et al.*, 2013; MISOL *et al.*, 2024). The absence of reduction events above 600 K suggests a relatively weak interaction between Ru species and the MAS311 support compared to other previously reported hydrotalcite-derived catalysts (BALLARINI *et al.*, 2013; MISOL *et al.*, 2024). Furthermore, the lack of detectable RuO_2 phase in the XRD patterns (Figures 4.5 and 4.8) may be attributed to highly dispersed Ru species in the oxide matrix, preventing the formation of large crystalline domains (MISOL *et al.*, 2024). In turn, the reducibility of the Re species depends strongly on the nature of the oxide support, primarily due to variations in the strength of the bridging Re–O–support bonds (MITRA *et al.*, 2001; TING *et al.*, 2022). Ting *et al.* investigated the TPR profiles of Re species supported on different oxides and reported that the onset reduction temperature followed the trend $\text{Re(VII)/SiO}_2 < \text{Re(VII)/Al}_2\text{O}_3 < \text{Re(VII)/MgO}$ going from approximately 600

K to 760 K (TING *et al.*, 2022). The broad peaks observed in the TPR profile of 0.1Re/MAS311 have been previously associated with the reduction of Re(VII) species, as well as the presence of Re nanoclusters and even isolated Re atoms (BARE *et al.*, 2011). Analogously to the 0.1Ru/MAS311 catalyst, the absence of detectable Re phases in the XRD (Figures 4.5 and 4.8) further supports this discussion. These findings suggest that the MAS311 support influences the electronic and structural properties of the Re species, possibly stabilizing high-valency states and affecting the overall reducibility profile. Finally, the absence of reduction events at temperatures exceeding 900 K indicates that the support remains in its oxidized state throughout the investigated temperature range, as expected from analogous materials, given its thermochemical stability even under reducing atmosphere (TING *et al.*, 2022).

4.1.7 Electronic structure of metals

Figure 4.15 presents the *in situ* UV-Vis spectra of the metal-containing catalysts, recorded from room temperature at intervals of 100 K, up to the final reduction temperature following a 1-h treatment.

The Ru-doped material (Figure 4.15a) exhibits a broad absorption peak spanning from 230 nm to 500 nm, which decreases in intensity and undergoes a slight blueshift as the temperature increases. A similar trend is observed for an additional peak appearing below 230 nm. In contrast, the Re-doped material (Figure 4.15b) shows the emergence of a new peak between 200 nm and 400 nm, which was absent at lower temperatures and also displayed a blueshift behavior. Meanwhile, the peak initially centered at approximately 200 nm progressively diminishes until it completely disappears after 1 h at 773 K.

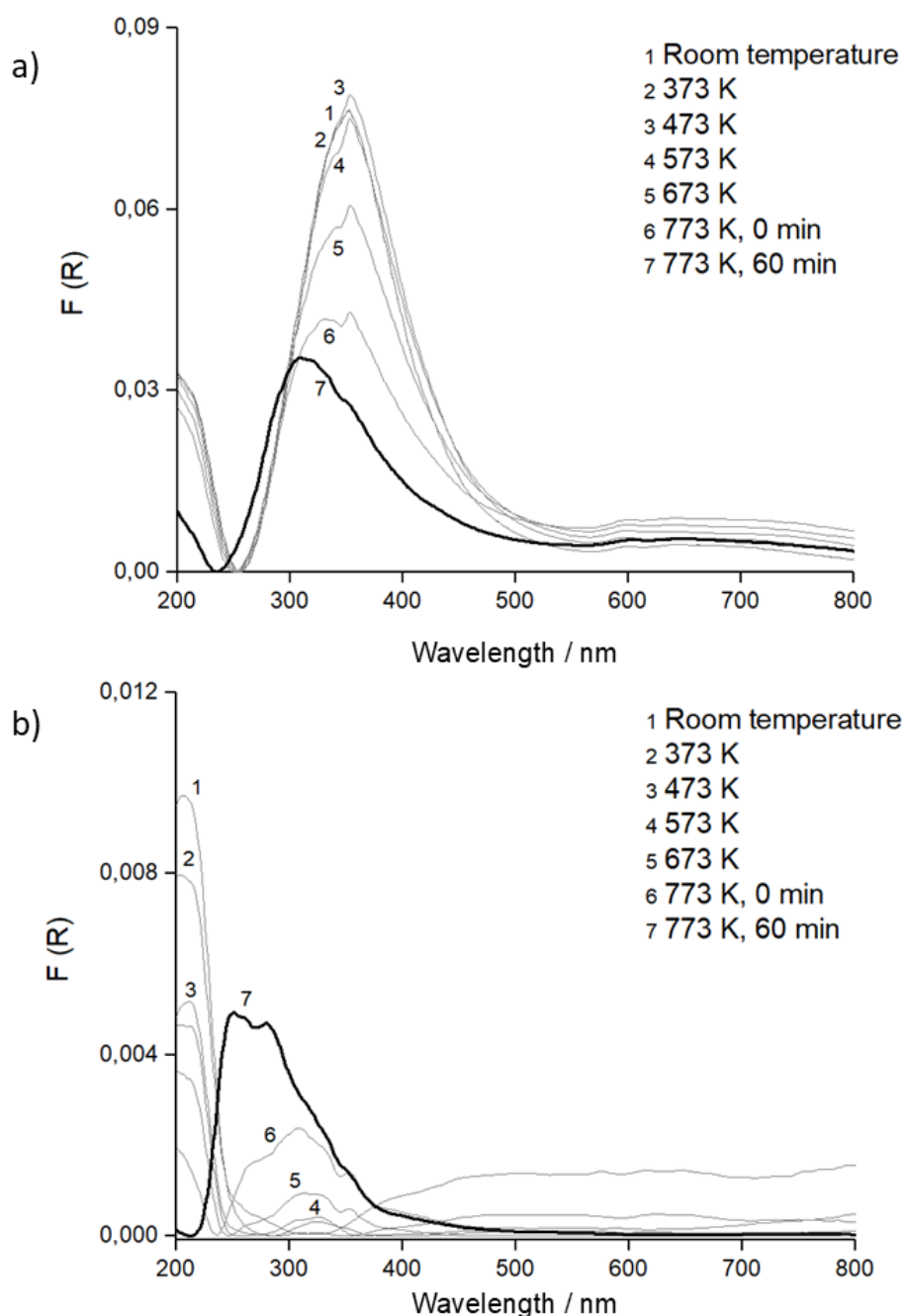


Figure 4.15 – UV-Vis spectra of a) 0.1Ru/MAS311 and b) 0.1Re/MAS311 catalysts.

The absorption band observed at approximately 350 nm in the Ru-containing material is attributed to the d–d transition of Ru^{3+} . Its progressive attenuation suggests the gradual reduction of Ru^{3+} to metallic Ru^0 (ZHANG *et al.*, 2007; KAMSUWAN; JONGSOMJIT; HERRERA, 2022). The spectral shifts observed in these bands can be assigned to the interaction between Ru species and OH groups of the support, which may influence the local electronic environment and stabilization of Ru oxidation states (KAMSUWAN; JONGSOMJIT; HERRERA, 2022). A similar trend is observed for the

absorption feature below 230 nm, which could indicate the involvement of small Ru clusters or highly dispersed Ru species in the reduction process, further highlighting the strong metal–support interactions in this system. These findings are in agreement with the expected RuO_x reduction to Ru, as per the TPR results (Figure 4.14). For the 0.1Re/MAS311 catalyst prior to the reduction treatment, the presence of a band at approximately 200 nm, coupled with the absence of d–d transition bands in the 300 nm – 800 nm region, indicates the lack of lower-valency Re species, suggesting that the catalyst predominantly contains Re⁷⁺ sites (LWIN *et al.*, 2015; ZHANG *et al.*, 2021; ZHANG; WACHS, 2021). Conversely, the band initially observed at 330 nm, which then shifts to 260 nm following the reduction treatment, has been attributed to mixed rhenium oxide species (ReO_x–Re⁷⁺O₅³⁻) (EDREVA-KARDJIEVA; VUURMAN; MOL, 1992; STOYANOVA *et al.*, 2008). Moreover, the increase in H₂ adsorption for this band, compared to the initial band observed at room temperature, is likely attributed to the gradual elimination of OH groups associated with the support (STOYANOVA *et al.*, 2008).

4.1.8 Surface chemistry analysis

The surface composition of the impregnated catalysts was analyzed using XPS survey spectra (Figure 4.16), with the corresponding quantitative analysis presented in Table 4.3. Due to the overlap between the most intense photoelectron line of Ru (Ru 3d_{5/2}) and the C 1s peak, the Ru 3p region was instead selected for analysis (PACHECO *et al.*, 2019). However, no detectable Ru signal was observed in this region, likely due to limitations in detection sensitivity. Similarly, the Re 4f peak, typically employed for XPS quantitative analysis, overlaps with the Mg 2p signal, thereby hindering accurate quantification of Re (CIMINO *et al.*, 1982).

The results confirmed that the surface compositions of Mg, Al, and Si in both catalysts aligned with the expected bulk stoichiometry, showing no significant deviations from the values obtained *via* ICP analysis (Table 4.1). This close agreement indicates minimal to no surface segregation or enrichment of these elements during synthesis or post-treatment steps, suggesting a homogeneous distribution of Mg, Al, and Si throughout the entire catalyst matrix, bulk or surface.

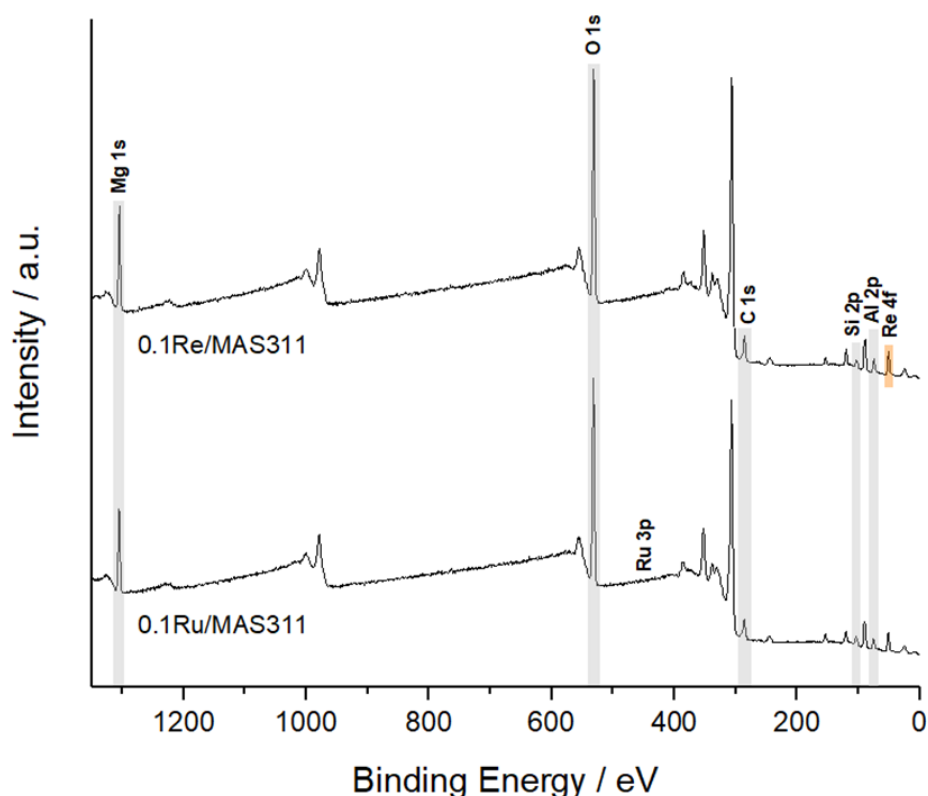


Figure 4.16 – XPS complete spectrum range for 0.1Ru/MAS311 and 0.1Re/MAS311.

Table 4.3 – XPS quantitative analysis (atomic %) for the elements.

Sample	Mg 1s	Al 2p	Si 2p	Mg : Al : Si
0.1Ru/MAS311	23.73	11.07	7.39	3.00 : 1.26 : 0.81
0.1Re/MAS311	23.24	12.64	4.97	3.00 : 1.47 : 0.56

The deconvoluted O 1s XPS spectra of 0.1Ru/MAS311 and 0.1Re/MAS311 are shown in Figure 4.17. The Ru-containing catalyst exhibits a less intense O 1s peak relative to its Re-containing counterpart, which may be attributed to a reduced surface oxygen concentration or modifications in the electronic environment of surface oxygen species, likely influenced by the interaction of Ru with the support. The low-binding energy component ($O\alpha$), centered around 530 eV, is attributed to lattice oxygen species (O^{2-}) associated with brucite-like layers formed by edge-sharing $M(OH)_6$ octahedron—characteristic of the layered double hydroxide-derived structure (JING *et al.*, 2021). A second component ($O\beta$), observed at 531.36 eV for 0.1Ru/MAS311 and slightly shifted to higher binding energy at 531.87 eV for 0.1Re/MAS311, corresponds to oxygen species in oxygen-deficient environments or low-coordinated surface oxygen, often related to

oxygen vacancies or defect sites. The third peak (O_γ), attributed to surface hydroxyl groups ($-\text{OH}$) or physisorbed water interacting *via* hydrogen bonding, exhibits a more pronounced shift, with a nearly 1 eV difference between the two catalysts (WANG *et al.*, 2024).

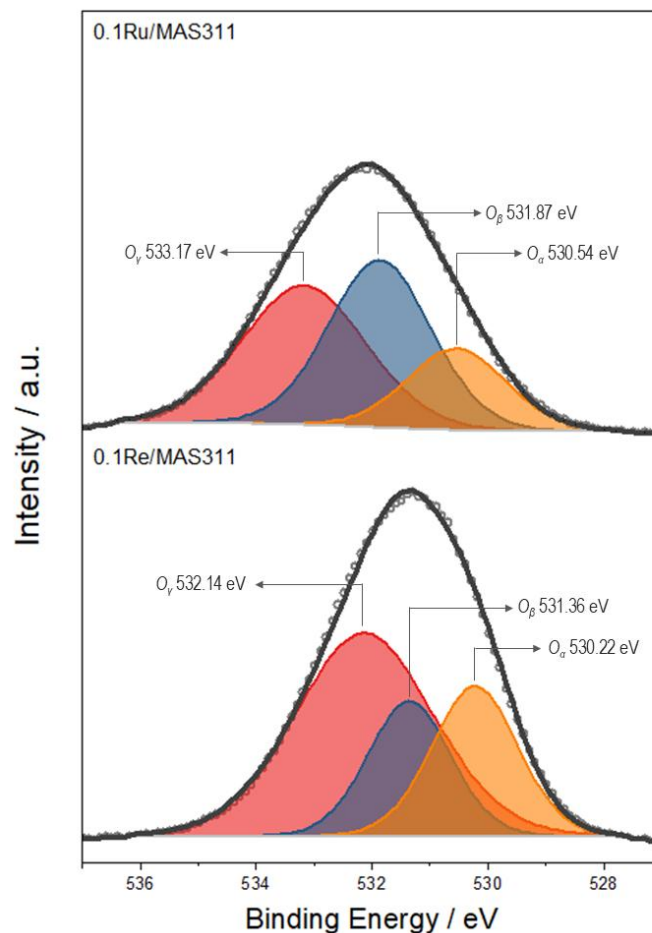


Figure 4.17 – XPS spectra of the O 1s region for 0.1Ru/MAS311 and 0.1Re/MAS311.

Although XPS data does not directly probe the basicity of a material, qualitative correlations can be made between O 1s components and basic site types. The O_γ component, typically associated with weak basic sites such as surface hydroxyl groups, represents the largest contribution to the O 1s spectra in both catalysts—accounting for 40.44 % in 0.1Ru/MAS311 and 53.72 % in 0.1Re/MAS311. This trend is consistent with the basic site distribution determined by CO_2 -TPD analysis (Section 4.1.6), revealed a predominance of weak basic sites in both catalysts. In contrast, the O_β and O_α components—attributed to medium (e.g., low-coordination O^{2-} near cations) and strong basic sites (lattice O^{2-}), respectively—exhibited lower relative contributions: 40.43% (O_β) and 19.13% (O_α) for the Ru-containing catalyst, and 21.48% (O_β) and 24.79% (O_α) for the Re-containing catalyst. These proportions reflect the same trend observed in the CO_2 -

TPD data, further supporting the assignment of O 1s features to different basic site strengths.

4.2 Catalytic tests

4.2.1 Effect of reaction temperature on the performance of MAS111

To evaluate the performance of the synthesized catalysts, initial catalytic tests were conducted to determine the optimal operating temperature for the system. The conversion and selectivity of the equimolar catalyst MAS111 were assessed across a range of temperatures selected based on typical reaction conditions reported in the literature (CHIEREGATO *et al.*, 2015; POMALAZA *et al.*, 2020). The study was performed at 523 K, 573 K, 623 K, 673 K, and 723 K, while all other experimental parameters were held constant. Prior to the temperature screening, a series of assays was conducted to establish the kinetic regime of the system, as depicted in Figure 4.18. The observed linear relationship between ethanol conversion and GHSV⁻¹ confirms that, within the evaluated range, the system operates under kinetic control, free from external diffusion limitations. It is also assumed that the chosen granulometry renders the system free from internal diffusion issues as well. For consistency and experimental feasibility, GHSV⁻¹ of 4 mg min mL⁻¹ was selected for all subsequent studies. In this setup, 100 mg of catalyst was used with an Ar flow rate of 25 mL min⁻¹ containing 5 % ethanol (GHSV 0.25 mL mg⁻¹ min⁻¹). The system pressure was maintained at 1.0 bar. Blank experiments conducted in the absence of catalyst showed negligible conversion. For all experiments, the carbon balance exceeded 85 %.

Figure 4.19 shows the results for ethanol conversion and selectivity of the main products for the equimolar catalyst across the analyzed temperature range (additional details are provided in Appendix A). The reaction at 523 K was ineffective under the tested conditions, yielding negligible ethanol conversion (the observed selectivity mainly shows the thermal decomposition of EtOH into AcH); therefore, results for this temperature are neither presented nor discussed. It is important to acknowledge that, due to technical limitations, the separate identification of BD and certain butenes isomers (1-butene and isobutene) was not feasible, and as a result, these products are reported collectively under the label "BD."

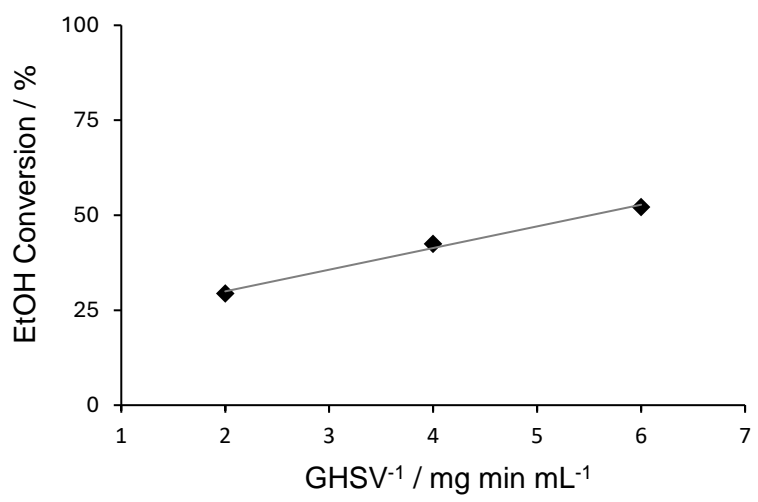


Figure 4.18 – Linear correlation between ethanol conversion and reactor space time demonstrates kinetic regime. Experiments were carried out with varying catalyst bed and flow rates at 723 K and 1 bar, and a 5 % ethanol concentration in the inlet stream.

The solid gray line represents the best linear fit, for visual clarity.

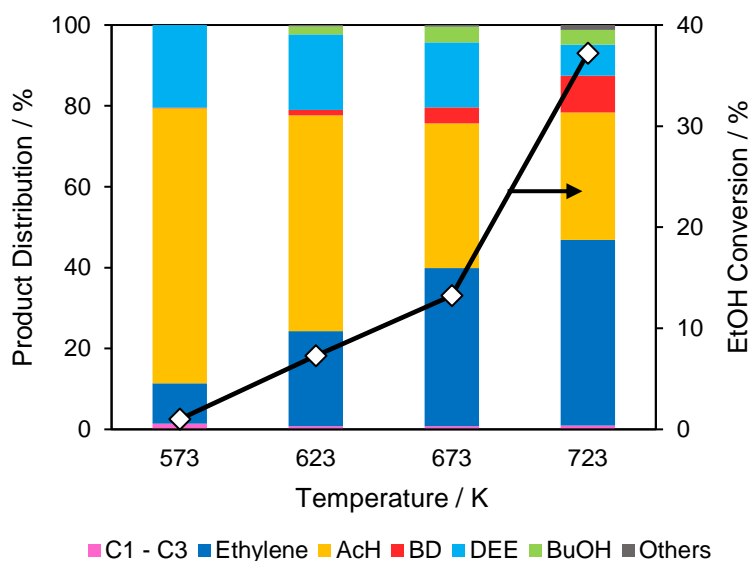


Figure 4.19 – Ethanol conversion and product distribution of MAS111 at different temperatures with a flow rate of 0.25 mL mg⁻¹ min⁻¹.

The primary products identified were ethylene, AcH, BD, butenes, DEE, BuOH, and other hydrocarbons, including methane, ethane, and propylene, collectively referred to as C1–C3. This diverse product distribution was expected due to the inherent complexity of the process, which involves multiple parallel reactions, further emphasizing ethanol's role as a versatile platform molecule. Given the endergonic nature of the reaction, an increase in temperature is expected to enhance ethanol conversion, a

trend that was confirmed within the investigated temperature range. At the lowest temperature, 573 K, ethanol conversion was approximately 1 %, increasing progressively with temperature and reaching a maximum of 37 % at 723 K.

Regarding product selectivity, a contrasting trend was observed between the dehydration products ethylene and DEE. Ethylene selectivity increased with temperature, whereas DEE selectivity declined as higher temperatures were employed. This behavior is consistent with previous studies (CHEN *et al.*, 2007; PHUNG *et al.*, 2014) and can be attributed to the distinct thermodynamic and mechanistic pathways of these reactions. Ethylene formation proceeds *via* an endothermic intramolecular dehydration mechanism, whereas DEE is produced through an exothermic intermolecular dehydration pathway. Additionally, DEE may act as an intermediate in ethylene production, decomposing at elevated temperatures to further contribute to ethylene formation.

Within the studied temperature range, it is evident that the selectivity towards AcH decreases from 68.0 % at 573 K to 31.5 % at 723 K. Previous studies on the dehydrogenation of ethanol to AcH have reported that selectivity for this product remains stable or increases between 473 K and 573 K, but declines at higher temperatures. This decline is attributed to the increasing formation of condensation products, alongside increased competition for ethanol, which undergoes enhanced dehydration to ethylene at elevated temperatures (YU *et al.*, 2019; PAMPARARO *et al.*, 2020). Among the condensation products of AcH, BuOH exhibited the highest selectivity at 673 K, reaching 3.9 %. At 573 K, BuOH is not observed as a condensation product of AcH, and AcH itself exhibited the highest selectivity under the experimental conditions used, suggesting that the condensation reaction may be inhibited at lower temperatures. As the temperature increased, BuOH selectivity increased; however, at 723 K, the value is reduced to 3.6 %. These findings suggest a volcano-type behavior, similar to previously observed by Wang *et al.* for the 2%Cu-NiMgAlO catalyst, who attributed the trend of stability followed by a reduction in BuOH selectivity to its decomposition into butenes at higher temperatures (WANG *et al.*, 2022c). To further investigate this hypothesis, experiments conducted at temperatures above 723 K would be necessary, but such tests were not performed in this study as they were beyond the scope of the research.

Studies have demonstrated a strong correlation between the selectivities of AcH and BD, suggesting that the condensation of AcH is the rate-determining step for BD formation (MAKSHINA *et al.*, 2014; CHIEREGATO *et al.*, 2015). This hypothesis is

reinforced by the opposing trends observed in the selectivities of these two products in this study. The highest BD selectivity, 9.1 %, was recorded at 723 K, when AcH selectivity reached its lowest value of 31.5 %. However, the relationship between BD selectivity, temperature, and the catalytic system remains partially unclear due to variations in reaction conditions, indicating that optimal reaction temperature must be determined on a case-by-case basis (MAKSHINA *et al.*, 2014). Based on these findings, 723 K was selected as the operating temperature for the performance evaluation of the non-equimolar catalysts in this study.

The analysis of product selectivity as a function of ethanol conversion (Figure 4.20) further highlights the predominance of AcH at low conversion levels and its sharp decline as ethanol conversion increases, which is typical of a cascade-type reaction mechanism. This behavior may be attributed to higher conversions or longer reaction times, in which the accumulation of AcH enables its participation as an intermediate in condensation reactions, leading to the formation of additional products. This trend is corroborated by the increase in BD and BuOH selectivity as ethanol conversion rises, suggesting that as more ethanol is converted, greater amounts of AcH are produced, subsequently facilitating the formation of condensation products. Among the dehydration products, a decline in DEE selectivity is observed, while ethylene selectivity increases. As previously discussed, DEE can serve as an intermediate in ethylene formation, so within the temperature range studied, higher ethanol conversions (or higher TOS) appear to be sufficient to promote DEE decomposition into ethylene. Furthermore, due to the nature of the experiments conducted in this study—where ethanol conversion is inherently linked to variations in the system temperature—ethylene formation is facilitated at higher temperatures, which in this case correspond to conditions of greater ethanol conversions (YU *et al.*, 2019).

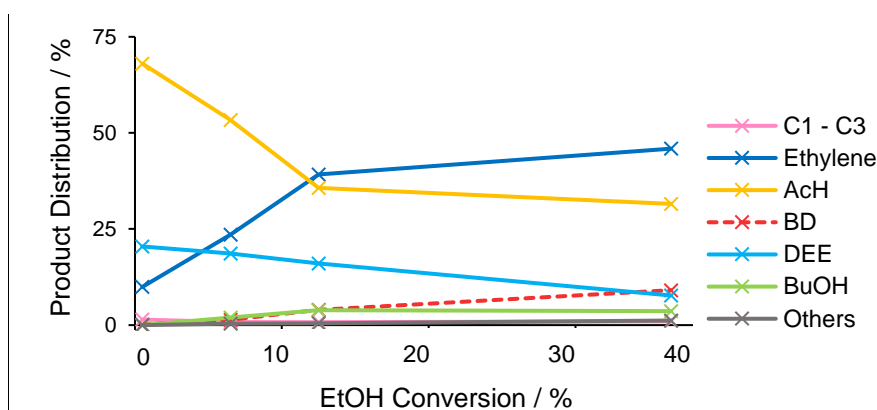


Figure 4.20 – Product selectivity as a function of ethanol conversion.

4.2.2 Effect of the Mg:Al:Si ratio on catalytic performance

After establishing the optimal operating temperature, the next step involved assessing the performance of the synthesized catalysts under identical reaction conditions. In these experiments, 100 mg of catalyst were loaded into the catalytic bed, with an Ar flow rate of 25 mL min⁻¹ containing 5 % ethanol (GHSV 0.25 mL mg⁻¹ min⁻¹), while maintaining the system pressure at 1 bar. Figure 4.21 presents the results regarding ethanol conversion and the selectivity of the main reaction products for catalysts with varying Mg:Al:Si molar ratios. For the detailed dataset, the reader is referred to Appendix A.

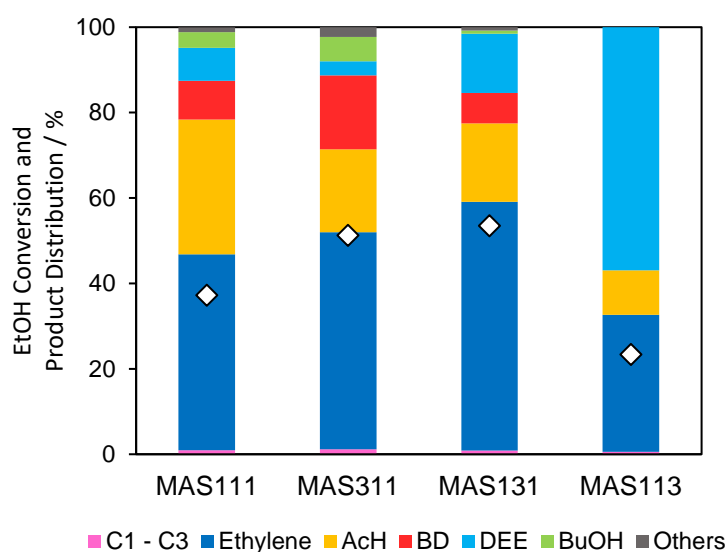


Figure 4.21 – Ethanol conversion and product distribution at 723 K with a flow rate of 0.25 mL mg⁻¹ min⁻¹.

As observed in the previous experiments, the predominant reaction products detected were ethylene, AcH, BD, butenes, DEE, and BuOH. Ethanol conversion increased for MAS311 and MAS131 compared to the equimolar catalyst but decreased for MAS113. This variation in conversion may be attributed to differences in the specific surface area of the catalysts. Samples with higher Mg and Al content exhibited increased surface areas, whereas the catalyst with a higher Si content showed a comparatively lower surface area relative to the equimolar catalyst. Notably, when ethanol conversion was normalized by the specific surface area of each catalyst, the resulting values were 0.22 g m⁻², 0.20 g m⁻², 0.24 g m⁻², and 0.23 g m⁻² for MAS111, MAS311, MAS131, and MAS113, respectively. This consistency suggests uniform intrinsic catalytic activity

across all samples under normalized isoconversion conditions and allows for fair comparison among materials at similar extents of reaction. Therefore, variations in catalyst composition, which influence the quantity, strength, and nature of acid and basic sites, are likely to affect only product selectivity rather than overall conversion efficiency and potential conversion-selectivity trade-off features.

The role of strong acid sites in alcohol dehydration reactions remains a topic of ongoing debate; however, there is broader consensus regarding the contribution of basic sites. In both MgO–SiO₂ systems and Mg–Al mixed oxides, the presence of weak surface basic sites—likely associated with surface hydroxyl groups—is considered beneficial for facilitating ethanol dehydrogenation. Medium-strength Mg–O and Al–O pairs are known to promote aldol condensation, while strongly basic tricoordinated oxygen anions (O²⁻) are highly reactive but susceptible to deactivation due to poisoning by condensation products. It is crucial to note that the mechanisms underlying ethanol conversion reactions require the cooperative interaction between acid and basic sites. Therefore, not only the quantity and strength of active sites but also their spatial proximity are critical for achieving selective ethanol transformation (ANGELICI *et al.*, 2015; POMALAZA *et al.*, 2020). For instance, one proposed mechanism for aldol condensation involves the enolization of an AcH molecule at an acid–base pair site, followed by its reaction with a neighboring AcH molecule to form a new C–C bond—highlighting the importance of site proximity (Figure 4.22). Moreover, reactions that require stronger basicity, such as ethanol dehydrogenation and subsequent condensation, are believed to proceed *via* the initial formation of surface ethoxide species on Lewis acid–strong base pairs (DI COSIMO *et al.*, 1998).

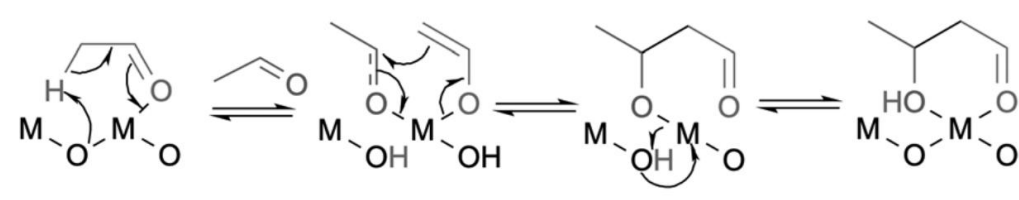


Figure 4.22 – Proposed mechanism for the aldol condensation of AcH, where M represents a metal atom (POMALAZA *et al.*, 2020).

For the MAS113 catalyst, the predominant product is DEE, followed by ethylene, which are the main products of ethanol dehydration. This behavior can be attributed to the catalyst’s basic and acidic site distribution. MAS113 features a higher concentration

of strong basic sites compared to weak and medium ones, with a site density ratio of weak/medium/strong = 1.67:1:2.53. Moreover, the presence of SiO₂ contributes to a Brønsted acidic character (VIEIRA *et al.*, 2022). The absence of condensation products suggests that the catalyst lacks the strong acid–base pair interactions typically required for such reactions, as evidenced by NH₃-TPD data (Section 4.1.6), which show a scarcity of acidic sites.

It is important to note that, as previously discussed, higher temperatures are expected to favor ethylene formation over DEE, but this behavior was not observed in this case. To further investigate this unusual response, catalytic tests were performed at additional temperatures (673 K and 773 K) to assess the effect of temperature on product selectivity for this catalyst. As illustrated in Figure 4.23, the results align with established literature: ethylene selectivity increases with temperature ($S_{\text{ethylene}}(673 \text{ K}) < S_{\text{ethylene}}(723 \text{ K}) < S_{\text{ethylene}}(773 \text{ K})$), whereas DEE selectivity decreases accordingly ($S_{\text{DEE}}(673 \text{ K}) > S_{\text{DEE}}(723 \text{ K}) > S_{\text{DEE}}(773 \text{ K})$). The unexpected selectivity pattern observed at 723 K in the initial experiments may be ascribed to kinetic constraints, as the pathway towards intermolecular dehydration was favored over the intramolecular one. However, upon evaluation over an extended temperature range, the anticipated thermodynamic trend was restored: the endothermic dehydration pathway leading to ethylene became favorable at higher temperature, while the exothermic formation of DEE was progressively suppressed. These findings underscore the dominant influence of thermodynamic driving forces in dictating product selectivity during ethanol dehydration.

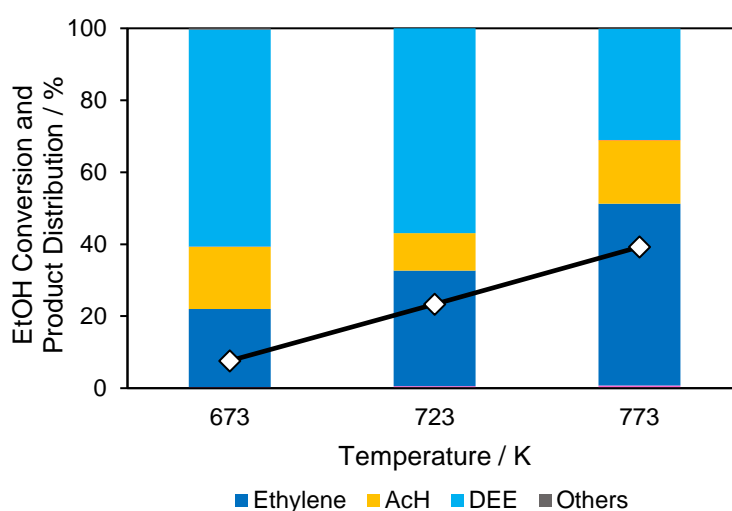


Figure 4.23 – Conversion and product distribution for the MAS113 catalyst at 0.25 mL mg⁻¹ min⁻¹.

As previously discussed, the interplay between acidic and basic surface properties plays a pivotal role in governing the complex reaction mechanisms involved in the catalytic upgrading of ethanol to higher products. The acid–base characteristics of mixed oxide catalysts can be finely tuned by adjusting the relative proportions of Mg and Al, thereby directly influencing catalytic performance. In the case of the MAS131 catalyst, the higher Al content is expected to enhance ethanol dehydration, favoring ethylene formation through acid-catalyzed pathways—particularly under elevated temperatures. Consistent with this expectation, MAS131 exhibited the highest ethylene selectivity among the unsupported catalysts, reaching 58.2 % at 723 K. Conversely, the formation of products that depend on basic sites, such as BuOH and BD, was limited. The combined selectivity for these products was only 7.8 %, the second lowest among the catalysts, following MAS113, where it was negligible.

The MAS311 catalyst, characterized by the highest Mg content among the samples, exhibited the greatest selectivity for BD, reaching 17.3 %. Additionally, the selectivity for BuOH was significantly enhanced compared to the other catalysts, attaining 5.7 %. Although MAS311 also displayed a notable ethylene selectivity of 50.8 %, the selectivity for DEE—another ethanol dehydration product—declined markedly, reaching its lowest value 3.3 %. In comparison to the equimolar catalyst, MAS311 demonstrated an increase in BD selectivity accompanied by a reduction in AcH selectivity. This trend aligns with the mechanistic pathway for C–C bond formation in ethanol upgrading, where AcH is initially generated *via* ethanol dehydrogenation. The subsequent steps—considered rate-limiting—involve the formation of carbocation intermediates at proximate acid–base site pairs: AcH is adsorbed on acidic sites, while adjacent basic sites abstract a proton from the aldehyde, generating a reactive carbocation species. This intermediate then undergoes nucleophilic attack by another adsorbed AcH molecule, forming acetaldol, a key precursor to higher oxygenates and unsaturated hydrocarbons (DI COSIMO *et al.*, 2000; ANGELICI; WECKHUYSEN; BRUIJNINCX, 2013).

The role of surface acid–base properties in shaping product distribution is illustrated in Figure 4.24. Clearly, an increase in the basic-to-acid site ratio—i.e., a higher density of basic sites relative to acidic ones—induces divergent trends in selectivity. Products derived from ethanol dehydration, particularly ethylene and DEE, exhibit an overall increase in selectivity with rising basicity. In contrast, the combined selectivity

toward AcH, BuOH, and BD, intermediate and final products of ethanol dehydrogenation, decreases under the same conditions. This observation underscores the complexity of ethanol upgrading mechanisms and suggests that the enhancement of basicity alone, especially when it significantly outweighs surface acidity, does not necessarily promote the formation of C–C coupling products. Instead, a more equally balanced distribution of acid and base sites—where the basic-to-acid ratio approaches unity—appears more favorable for pathways involving dehydrogenation and subsequent condensation steps, while concurrently suppressing dehydration reactions. These results point to the importance of tailoring acid–base site synergy, rather than maximizing one type exclusively, to direct product selectivity toward higher-value compounds in ethanol conversion.

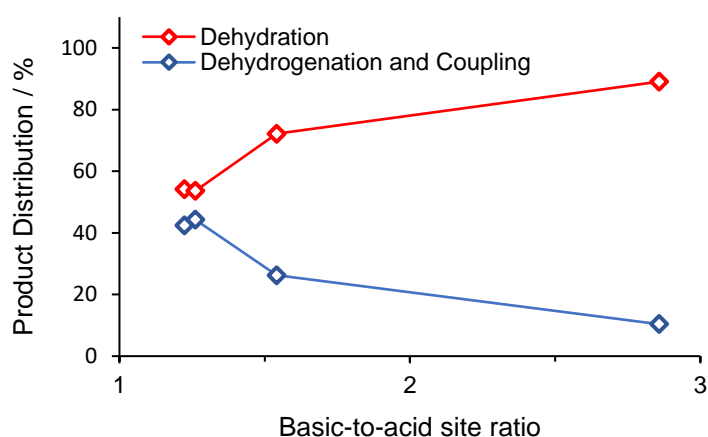


Figure 4.24 – Correlation between product distribution and the acidity and basicity of the unsupported catalysts.

4.2.3 Effect of reaction temperature on the performance of MAS311

Given the high ethanol conversion and superior BD selectivity among the unsupported catalysts, MAS311 performance was further evaluated across a range of reaction temperatures. Figure 4.25 presents the ethanol conversion and selectivity profiles for major products at varying temperatures using MAS311. Consistent with earlier findings, the main products formed include ethylene, AcH, butenes, BD, DEE, and BuOH.

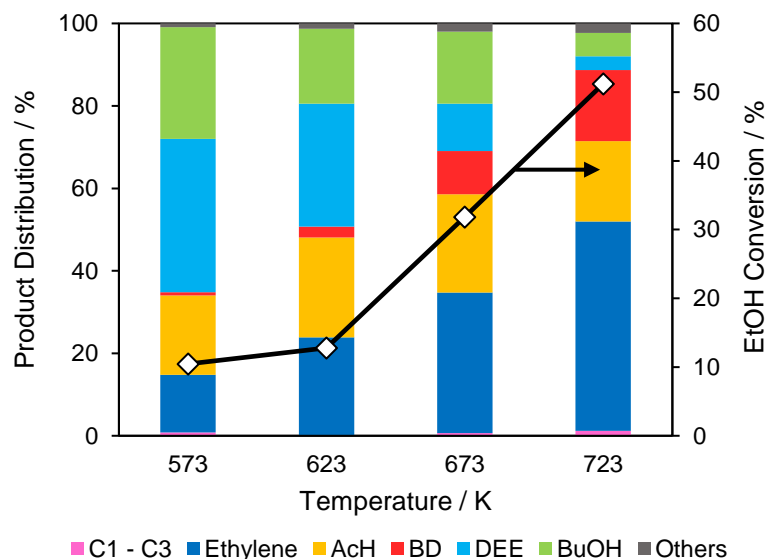


Figure 4.25 – Ethanol conversion and product selectivity for MAS311 at different temperatures at 1.0 bar and GHSV $0.25 \text{ mL mg}^{-1} \text{ min}^{-1}$.

As previously observed with MAS111 (Figure 4.19), a temperature-dependent shift is observed among dehydration products. Ethylene selectivity increases with temperature, consistent with the endothermic nature of the dehydration step that favors its formation at elevated temperatures. Conversely, DEE selectivity steadily decreases, as this exothermic product is thermodynamically less favored at higher temperatures. In contrast, the dehydrogenation-derived products exhibit distinct trends. Notably, BuOH selectivity drops significantly from 27.1 % at 573 K to 2.3 % at 723 K, while BD selectivity increases markedly, rising from 1 % to 17.8 % over the same temperature range. This inverse relationship suggests that increasing temperature not only promotes the subsequent dehydration of the intermediate crotonaldehyde into BD but also suppresses parallel hydrogenation reactions that lead to BuOH. Interestingly, AcH selectivity remains relatively constant across all temperatures studied, indicating a stable intermediate pool and suggesting the ongoing occurrence of aldol condensation.

These results point to an enhanced contribution of the Lebedev pathway at elevated temperatures, likely favored over the Guerbet route under these conditions. The consistent AcH levels and increasing BD yields between 623 K and 723 K further support the notion of an activated Lebedev pathway. In contrast, the declining BuOH selectivity suggests a diminished contribution from the Guerbet route, which typically requires effective hydrogenation steps, more dominant at lower temperatures and under different acid/base balances (GABRIËLS *et al.*, 2015).

4.2.4 Catalytic Stability of MAS311

Catalyst deactivation remains a persistent challenge in ethanol upgrading processes, often limiting long-term performance and industrial viability (ZHANG *et al.*, 2020). To assess the stability of the catalysts under reaction conditions relevant to this study, a longer TOS experiment was conducted using the MAS311 catalyst. The material was subjected to a significantly prolonged reaction time of 72 h, exceeding the duration of standard catalytic assays. Although this time frame is still far from industry standards, it could yield important information on the catalyst behavior at the beginning of its operating cycle. The test was carried out at 723 K—chosen as the upper temperature limit within this study’s operating window—to simulate harsh reaction conditions most likely to promote deactivation phenomena, presumably through sintering of active phase or formation of amorphous coke.

The results, presented in Figure 4.26, illustrate ethanol conversion and product selectivity trends throughout the test. Over the 72-h period, MAS311 maintained relatively stable catalytic performance, with minimal loss in activity or selectivity shifts. This suggests a high degree of thermal and chemical robustness under continuous operation, consistent with the structural resistance previously observed through *operando* XRD analysis (Section 4.1.4). A potential contributing factor to this result is the minimized impact of coke deposition, likely facilitated by the material's high porosity, which enhances diffusion and helps preserve active site accessibility, thereby supporting its catalytic stability.

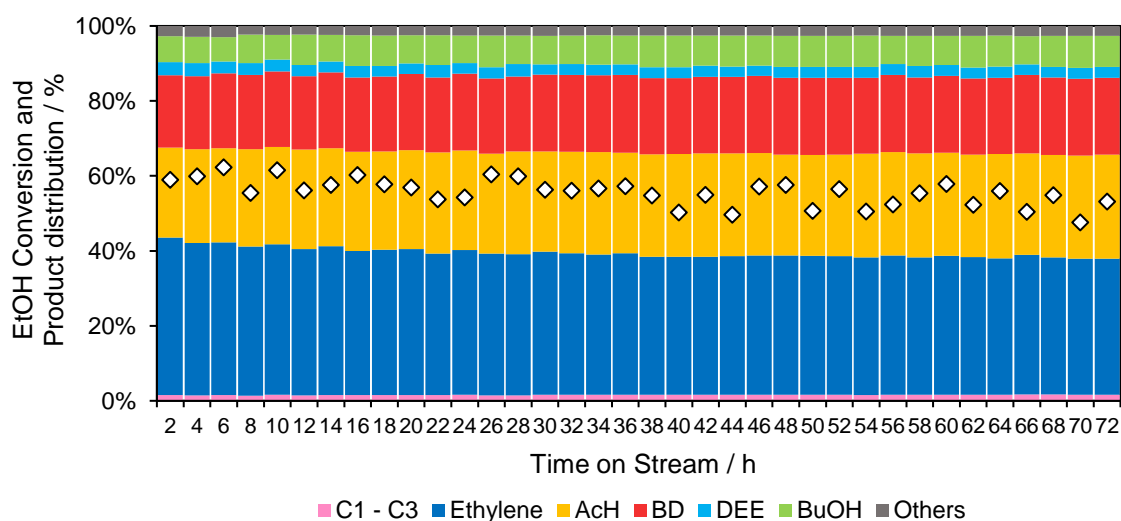


Figure 4.26 – Stability test for MAS311 at 723 K, 1.0 bar and 0.25 mL mg⁻¹ min⁻¹.

4.2.5 Effect of metal doping on catalytic performance of MAS311

To elucidate the role of dehydrogenating agents in the ethanol upgrading reaction, the catalytic performance of metal-doped variants of the MAS311 catalyst were investigated at 673 K, 1.0 bar and GHSV of $0.25 \text{ mL mg}^{-1} \text{ min}^{-1}$. The incorporation of transition metals such as Ru and Re is known to enhance the catalyst's ability to facilitate dehydrogenation steps, potentially influencing the distribution of key products (KOZLOWSKI; DAVIS, 2013b; BIN SAMSUDIN *et al.*, 2020). A comparison of the catalytic performance of these doped catalysts to the undoped MAS311 is presented in Figure 4.27.

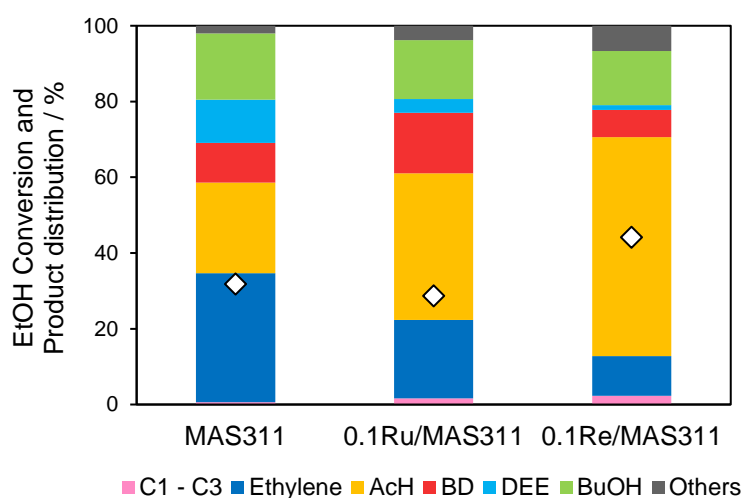


Figure 4.27 – Ethanol conversion and product distribution of unsupported MAS311 and Ru- and Re-doped at 673 K, 1.0 bar and $0.25 \text{ mL mg}^{-1} \text{ min}^{-1}$.

Ethanol conversion remained nearly unchanged for 0.1Ru/MAS311 compared to the undoped MAS311 catalyst. In contrast, 0.1Re/MAS311 exhibited a substantial enhancement in conversion, reaching 44.1 %. This improvement is particularly notable given the reduction in surface area from $266 \text{ m}^2 \text{ g}^{-1}$ (MAS311) to $210 \text{ m}^2 \text{ g}^{-1}$ upon Re incorporation. Furthermore, significant alterations in product distribution were observed. The selectivity toward AcH increased for both metal-doped catalysts, suggesting that the addition of transition metals effectively promotes ethanol dehydrogenation. Although a significant enhancement in the dehydrogenation step is evident, the subsequent hydrogenation and dehydration reactions—responsible for the formation of BuOH and BD, respectively—do not appear to benefit to the same extent. This is reflected in the combined selectivity toward BuOH and BD, which increases only marginally from 28.0

% for MAS311 to 31.4 % for the Ru-doped catalyst, and notably decreases to 21.5 % for the Re-doped counterpart.

This limited improvement—or, in the case of the Re-doped catalyst, a decline—in BuOH and BD selectivity may be attributed, in part, to differences in surface electronic environments and modifications in the acid–base properties induced by metal incorporation, as evidenced by TPD and XPS analysis (Sections 4.1.5 and 4.1.8, respectively). Notably, the enhancement in AcH selectivity was particularly pronounced for the Re-containing catalyst, a behavior that can be correlated with its surface characteristics. XPS results indicated a higher relative abundance of O_γ species—typically associated with weak basic sites—on the Re-containing material compared to its Ru-based counterpart. These weak basic sites are known to facilitate the initial dehydrogenation of ethanol to AcH, thereby contributing to the observed elevated selectivity toward this intermediate. Conversely, the Ru-containing catalyst displayed a greater concentration of O_β species, which are linked to medium basic sites and are more favorable for subsequent aldol condensation reactions. This observation is consistent with the higher selectivity toward C–C coupling products observed for this material. Moreover, the marked reduction in overall basic site density upon metal doping, as revealed by CO₂-TPD analysis, likely plays a critical role in limiting the formation of coupling products. Given that basic sites are essential for promoting aldol condensation and subsequent C–C bond formation, the decreased basicity likely hinders these pathways. Additionally, a strong interaction between the metal dopant and AcH may further contribute to an increased accumulation of this intermediate. Such interactions could stabilize AcH species on the catalyst surface, thereby impeding their further transformation by restricting access to adjacent active sites or limiting the surface mobility necessary for subsequent reactions.

These findings suggest that, while metal doping effectively promotes the initial ethanol dehydrogenation step, a comprehensive understanding of the electronic state of the dopant and its interaction with key intermediates is crucial. Moreover, providing an adequate distribution of acid and base functionalities remains essential for promoting the complete reaction sequence required for the efficient production of higher alcohols and dienes. This implies that, in such complex catalyst formulation, a more thorough understanding of the interplay between acid, basic and metallic sites is required to further improve catalyst tuning approaches.

Following the initial catalytic evaluation of the doped materials, their stability was then investigated under relevant reaction conditions through extended TOS experiments. In line with the stability test conducted for the MAS311 support, the doped catalysts were subjected to prolonged operation for 70 h; however, in this case, the tests were performed at 673 K to better assess their long-term performance under demanding conditions. The ethanol conversion and product distribution are presented in Figure 4.28.

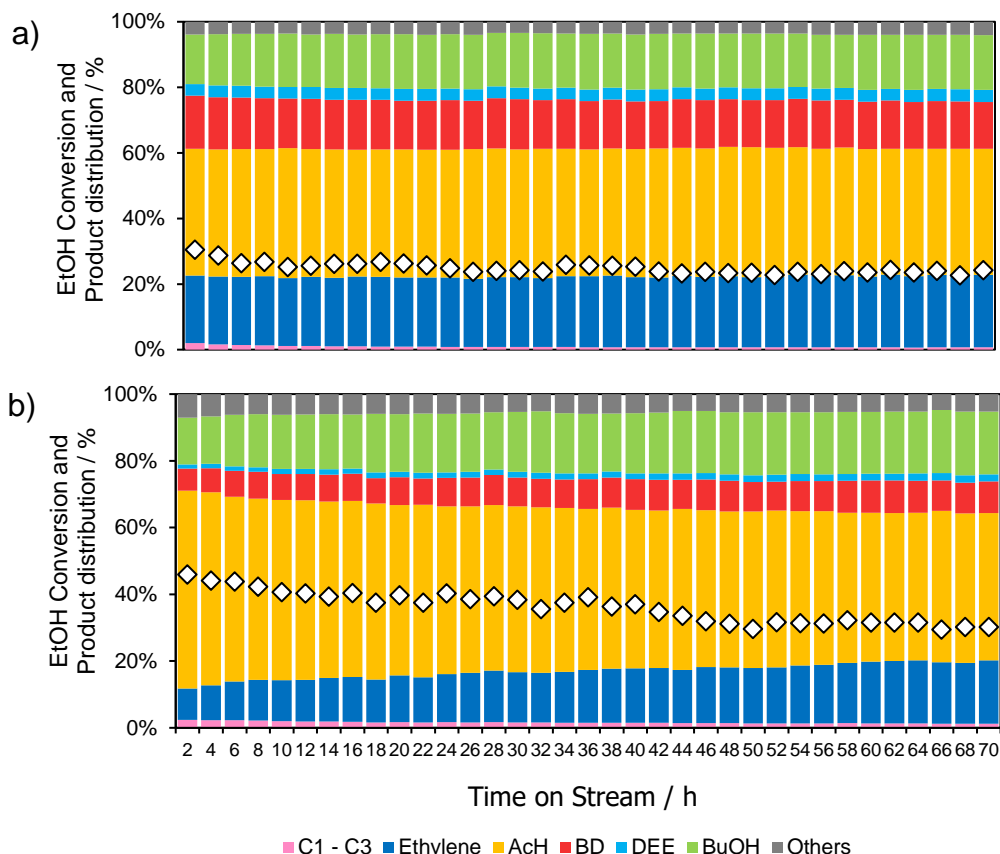


Figure 4.28 – Stability test for a) 0.1Ru/MAS311 and b) 0.1Re/MAS311 at 673 K, 1.0 bar and GHSV $0.25 \text{ mL mg}^{-1} \text{ min}^{-1}$.

The 0.1Ru/MAS311 catalyst (Figure 4.28a) exhibited notable stability over the 70-h TOS experiment, with ethanol conversion decreasing only moderately from 30 % to 24 %. The product distribution remained largely consistent throughout the duration of the test, with minimal fluctuations in selectivity across the major products, suggesting that the catalyst maintained its structural integrity—as previously suggested by the *operando* XRD analysis (see Section 4.1.4)—and active site accessibility under the applied conditions.

In contrast, the 0.1Re/MAS311 catalyst displayed more pronounced changes over time (Figure 4.28b). Ethanol conversion declined from an initial 46 % to 30 % after 70 h,

accompanied by a significant shift in product selectivity. Notably, ethylene formation increased from 9 % to 19 %, while AcH selectivity decreased from 59.3 % to 44.1 %. These variations may be indicative of partial catalyst deactivation. The increase in ethylene selectivity could point to an increase in Brønsted acid-mediated dehydration pathways, potentially promoted by the migration or transformation of oxidized Re species during extended exposure to the reaction environment. Simultaneously, the drop in AcH selectivity suggests a decline in dehydrogenation activity, which may result from changes in the oxidation state of Re or the loss of accessible active sites. It is plausible that the oxidized Re species, as detected by UV-Vis experiments—previously identified *via* UV-Vis spectroscopy (Section 4.1.7)—undergo further reduction under the hydrogen-rich, reducing conditions present during ethanol conversion. Such redox dynamics may lead to structural or electronic alterations of the Re phase, potentially resulting in loss of catalytic function and shifts in reaction pathways. This highlights the redox-sensitive nature of Re-based catalysts and suggests that the interplay between oxidation state, acidity, and active site availability plays a critical role in dictating both catalyst stability and selectivity. However, additional *operando* or post-reaction characterizations would be necessary to confirm these mechanistic hypotheses and to elucidate the precise deactivation pathways involved.

Chapter 5

Conclusions

The synthesis conditions employed for the preparation of the catalysts proved to be appropriate for the intended objectives. Although the experimental Mg, Al, and Si contents exhibited some deviations from the theoretical values, they were deemed acceptable for the scope of this study. As anticipated, alterations in the molar ratios of these elements imparted distinct physicochemical characteristics to the catalysts. This was reflected in the formation of different crystalline structures, as identified by XRD analysis. The equimolar MAS111 catalyst exhibited phases corresponding to hydrotalcite-like structures, while MAS311 showed diffraction peaks characteristic of periclase-type MgO. In contrast, MAS113 was dominated by amorphous or poorly crystalline SiO₂, and MAS131, which contained the highest Al content, did not exhibit any detectable crystalline phases. These compositional changes also significantly affected the textural properties and surface site characteristics of the catalysts. Among the series, MAS311 displayed the highest specific surface area (266 m² g⁻¹), as well as the highest density of basic sites (1.82 μmol m⁻²), suggesting a surface environment more favorable to base-catalyzed reactions. On the other hand, MAS113, with the lowest surface area (103 m² g⁻¹), exhibited the lowest total site density and a predominance of acid sites. These structural and surface characteristics are expected to play a decisive role in the catalytic performance of the materials in ethanol conversion reactions.

The catalytic evaluation of the unsupported catalysts yielded results that are consistent with literature reports and met the expectations of this study. All catalysts demonstrated activity for ethanol conversion under the applied reaction conditions. It was possible to discern clear correlations between the acid–base properties and the product distribution. A higher basic-to-acid site ratio favored ethanol dehydration pathways, promoting the formation of ethylene and DEE, while a more balanced ratio—particularly values approaching unity—promoted aldol condensation and subsequent hydrogenation steps, enhancing the formation of higher alcohols and dienes, such as BuOH and BD. Among the evaluated catalysts, MAS311 delivered the most promising performance for

BD production, achieving a selectivity of 17.3 % at 51 % ethanol conversion under reaction conditions of 723 K and a GHSV of 0.25 mL mg⁻¹ min⁻¹. This outcome is attributed to the optimal balance of acid and basic sites (basic-to-acid sites ratio of 1.22), which are essential for facilitating both aldol condensation of AcH and the subsequent dehydration of crotyl alcohol to BD.

The incorporation of metal species into MAS311 *via* incipient wetness impregnation was successfully achieved even at low loadings (mass fraction of 0.1 %), as confirmed by ICP analysis. Metal doping significantly modified the catalyst's physicochemical properties. The specific surface area decreased to 215 m² g⁻¹ for 0.1Ru/MAS311 and 210 m² g⁻¹ for 0.1Re/MAS311, likely due to partial pore blockage or restructuring upon metal incorporation. Furthermore, the incorporation of Ru and Re induced significant modifications in the surface acid–base properties of the catalysts, leading to markedly reduced basic-to-acid site ratios—i.e., an excess of acidic sites relative to basic ones. However, characterizing materials at such low Ru and Re contents is still challenging, particularly regarding XPS analysis. Catalytic performance testing of the doped materials demonstrated a pronounced enhancement in the initial ethanol dehydrogenation step, as evidenced by increased selectivity to AcH—38.7 % for 0.1Ru/MAS311 and 7.8 % for 0.1Re/MAS311. However, despite this improvement in the initial step, the overall yields of downstream products such as BD and BuOH remained limited. This indicates that while metallic active sites facilitate ethanol dehydrogenation, the progression of the reaction toward higher molecular weight products also requires a suitable distribution of acid and basic sites to catalyze condensation, hydrogenation, and dehydration steps effectively.

Operando XRD analysis proved to be a particularly valuable technique in this study, offering real-time insights into the structural integrity of the catalysts under actual reaction conditions. For both the undoped and metal-doped MAS311 catalysts, no significant phase transformations or structural degradation were observed throughout the duration of the *operando* analysis. These findings were further validated by long-term catalytic stability tests, conducted over 70 h of TOS, which demonstrated minimal deactivation, reinforcing the suitability of these materials for continuous ethanol upgrading applications.

5.1 Suggestions for upcoming works

To build upon the findings of this study and deepen the understanding of structure–activity relationships in ethanol upgrading catalysts, several avenues for future research are recommended.

One promising direction involves widening the variation in molar ratios of Mg, Al, and Si used in this novel catalyst. In this work, selected compositions demonstrated how subtle shifts in metal ratios can significantly alter the physicochemical properties, such as crystallinity, surface area, and acid–base site distribution. Exploring a broader compositional space could help identify optimal combinations that better promote desired reaction pathways, such as aldol condensation and selective hydrogenation steps, while minimizing unwanted dehydration routes.

Another important line of investigation is the screening of a wider range of metallic dopants beyond Ru and Re. Transition metals with different redox properties, electron affinities, or coordination behavior—such as Cu, Pd, Zn, or Ni—may interact differently with key intermediates like AcH or crotonaldehyde. Comparative studies could provide valuable insights into how these dopants influence both reaction pathways and catalyst stability, potentially identifying more efficient or cost-effective alternatives.

Given the low metal loadings (0.1 mass fraction) employed in this study and seeing how promise it is, another critical recommendation is the implementation of more sensitive characterization techniques capable of detecting and analyzing such trace amounts with high resolution. Techniques such as synchrotron-based X-ray absorption spectroscopy (XAS) and high-resolution transmission electron microscopy (HR-TEM) could offer more detailed insights into the local environment of metal atoms, their oxidation states, dispersion, and interaction with the support.

Lastly, it is suggested to systematically vary reaction conditions, including temperature, pressure, space velocity, and ethanol partial pressure, in order to map out the full catalytic potential of the synthesized materials. Such studies could help determine optimal operational windows for each catalyst and reveal kinetic limitations or regime shifts that are not observable under a single set of conditions. Moreover, getting closer to industrial conditions, particularly for pressures and ethanol content in the feeding stream, could be valuable for assessing the materials. Additionally, conducting long-term stability

tests under varied conditions would provide a more comprehensive assessment of catalyst durability and resistance to deactivation mechanisms such as sintering or coking.

Collectively, these future directions would contribute to the rational design of more effective and selective catalysts for the upgrading of ethanol into higher products, supporting the development of more sustainable and efficient biomass-derived chemical processes.

Appendix

Appendix A

Table A.1 – Ethanol conversion values (%) and product selectivity (%) for the MAS111 catalyst at different temperatures. All reactions were conducted using 100 mg of catalyst loaded in a fixed-bed reactor, with an inert Ar flow of 25 mL min⁻¹ containing 5 % ethanol (GHSV: 0.25 mL mg⁻¹ min⁻¹).

	Temperature / K			
	573	623	673	723
S _{C1-C3}	1.44	0.82	0.77	0.95
S _{Ethylene}	9.93	23.5	39.16	45.9
S _{AcH}	68.04	53.32	35.72	31.53
S _{BD+butenes}	0.13	1.39	3.97	9.09
S _{DEE}	20.46	18.62	16.05	7.71
S _{BuOH}	0	1.98	3.88	3.63
S _{Others}	0	0.37	0.45	1.19
Conversion	1.00	7.28	13.22	37.21

Table A.2 – Ethanol conversion values (%) and product selectivity (%) for all un-doped catalysts. All reactions were conducted at 723 K, using 100 mg of catalyst loaded in a fixed-bed reactor, with an inert Ar flow of 25 mL min⁻¹ containing 5 % ethanol (GHSV: 0.25 mL mg⁻¹ min⁻¹).

	Catalyst			
	MAS111	MAS311	MAS131	MAS113
S_{C1-C3}	0.95	1.19	0.87	0.58
S_{Ethylene}	45.9	50.77	58.24	32.09
S_{AcH}	31.53	19.48	18.34	10.37
S_{BD+butenes}	9.09	17.28	7.13	0
S_{DEE}	7.71	3.32	13.9	56.96
S_{BuOH}	3.63	5.65	0.74	0
S_{Others}	1.19	2.32	0.79	0
Conversion	37.21	51.21	53.47	23.36

Table A.3 – Ethanol conversion values (%) and product selectivity (%) for the MAS311 catalyst at different temperatures. All reactions were conducted using 100 mg of catalyst loaded in a fixed-bed reactor, with an inert Ar flow of 25 mL min⁻¹ containing 5 % ethanol (GHSV: 0.25 mL mg⁻¹ min⁻¹).

	Temperature / K			
	573	623	673	723
S _{Cl-C3}	0.80	0	0.65	1.19
S _{Ethylene}	13.98	23.86	34.05	50.77
S _{AcH}	19.23	24.23	23.86	19.48
S _{BD+butenes}	0.83	2.66	10.52	17.28
S _{DEE}	37.16	29.81	11.44	3.32
S _{BuOH}	27.12	18.13	17.48	5.65
S _{Others}	0.87	1.31	2.01	2.32
Conversion	10.45	12.76	31.83	51.21

Table A.4 – Ethanol conversion values (%) and product selectivity (%) for the metal-doped catalyst. All reactions were conducted at 673 K, using 100 mg of catalyst loaded in a fixed-bed reactor, with an inert Ar flow of 25 mL min⁻¹ containing 5 % ethanol (GHSV: 0.25 mL mg⁻¹ min⁻¹).

	Catalyst	
	0.1Ru/MAS311	0.1Re/MAS311
S _{C1-C3}	1.61	2.30
S _{Ethylene}	20.72	10.49
S _{AcH}	38.75	57.78
S _{BD+butenes}	15.91	7.22
S _{DEE}	3.62	1.29
S _{BuOH}	15.59	14.25
S _{Others}	3.80	6.68
Conversion	28.71	44.11

References

- AKHADE S. A. [et al.]** Influence of Ag metal dispersion on the thermal conversion of ethanol to butadiene over Ag-ZrO₂/SiO₂ catalysts [Article] // Journal of Catalysis. - 2020. - 386. - 30-38.
- AMADA Y. [et al.]** Reaction mechanism of the glycerol hydrogenolysis to 1,3-propanediol over Ir-ReO_x/SiO₂ catalyst [Article] // Applied Catalysis B: Environmental. - 2011. - 1-2. - 117-127 : Vol. 105.
- ANGELICI C. [et al.]** Effect of Preparation Method and CuO Promotion in the Conversion of Ethanol into 1,3-Butadiene over SiO₂-MgO Catalysts [Article] // Chemsuschem. - 2014. - 2505-2515 : Vol. 7.
- ANGELICI C., VELTHOEN M. E. Z. and WECKHUYSSEN B. M.** Influence of acid–base properties on the Lebedev ethanol-to-butadiene process catalyzed by SiO₂–MgO materials [Article] // Catal. Sci. Technol.. - 2015. - 2869-2879 : Vol. 5.
- ANGELICI C., WECKHUYSSEN B. M. and CRUIJNINCX P. C. A.** Chemocatalytic Conversion of Ethanol into Butadiene and Other Bulk Chemicals [Article] // ChemSusChem. - 2013. - pp. 1595-1614 : Vol. 6.
- ARMSTRONG H. E. and MILLER A. K.** The decomposition and genesis of hydrocarbons at high temperatures. The products of the manufacture of gas from petroleum [Article] // Journal of the Chemical Society. - 1886. - 80. - Vol. 49.
- ASHOK A. [et al.]** Study of ethanol dehydrogenation reaction mechanism for hydrogen production on combustion synthesized cobalt catalyst [Article] // International Journal of Hydrogen Energy. - 2017. - 37. - 23464-23473 : Vol. 42.
- Association Renewable Fuels** Global ethanol production by country or region [Report]. - [s.l.] : U.S. Department of Energy, 2021.
- BAERDEMAEKER T. [et al.]** Bimetallic Zn and Hf on Silica Catalysts for the Conversion of Ethanol to 1,3-Butadiene [Article] // ACS Catal.. - 2015. - 5. - 3393–3397 : Vol. 6.
- BARRETO L, MAKIHIRA A and RIAHI K** The Hydrogen Economy in the 21st Century: A Sustainable Development Scenario [Article] // International Journal of Hydrogen Energy. - 2003. - 28. - pp. 267-284.
- BARROS S. and WOODY K.** Corn Ethanol Production Booms in Brazil [Article] // United States Department of Agriculture: Foreign Agricultural Service. - 2020.
- BATISTA L.** Alta do petróleo fez País viver crise nos anos 1970 [Online] // Estadão. - 12 6, 2014. - 1 7, 2022. - <https://acervo.estadao.com.br/noticias/acervo,alta-do-petroleo-fez-pais-viver-crise-nos-anos-1970,10618,0.htm>.
- BAZIN D. [et al.]** Re-Co/NaY and Re-Co/Al₂O₃ Bimetallic Catalysts: In Situ EXAFS Study and Catalytic Activity [Article] // Catalysis Letters. - 2002. - 82. - 169–182.
- BENITES-LAZARO L.L., MELLO-THÉRY N.A. and LAHSEN M.** Business storytelling about energy and climate change: the case of Brazil's ethanol industry [Article] // Energy Res Soc Sci. - 2017. - 31. - 77-85.

- BHATTACHARYYA S. and AVASTHI B.** One-Step Catalytic Conversion of Ethanol to Butadiene in a Fluidized Bed [Article] // *Ind. Eng. Chem. Process Des.* - 1963. - pp. 45-51 : Vol. 2.
- BHATTACHARYYA S. and SANYAL S.** Kinetic study on the mechanism of the catalytic conversion of ethanol to butadiene [Article] // *J. Catal.* - 1967. - 7. - 152-158.
- BHATTACHARYYA S. K. and GANGULY N. D.** One-step catalytic conversion of ethanol to butadiene in the fixed bed. II Binary- and ternary-oxide catalysts [Article] // *J. Appl. Chem.* - 1962. - pp. 105-110 : Vol. 12.
- BOLOGNINI M.** [*et al.*] Heterogeneous basic catalysts as alternatives to homogeneous catalysts: reactivity of Mg/Al mixed oxides in the alkylation of m-cresol with methanol [Article] // *Catalysis Today*. - 2002. - 1-4. - 103-111 : Vol. 75.
- BOND G.** Platinum Metals as Hydrogenation Catalysts [Article] // *Platinum Metals Review*. - 1957. - pp. 87-93 : Vol. 3.
- BRASIL H** [*et al.*] Synthesis modification of hydroxyapatite surface for ethanol conversion: The role of the acidic/basic sites ratio [Article] // *Journal of Catalysis*. - 2021. - 404. - pp. 802-813.
- BRAVO-SUÁREZ J, SUBRAMANIAM B and CHAUDHARI RV** Vapor-phase methanol and ethanol coupling reactions on CuMgAl mixed metal oxides [Article] // *Applied Catalysis A: General*. - 2013. - pp. 234-246 : Vol. 455.
- BRITO A.** [*et al.*] Biodiesel Production from Waste Oil Using Mg–Al Layered Double Hydroxide Catalysts [Article] // *Energy Fuels*. - 2009. - 6. - 2952–2958 : Vol. 23.
- BROADBENT H. S.** [*et al.*] Rhenium and Its Compounds as Hydrogenation Catalysts. III. Rhenium Heptoxide_{1,2,3} [Article] // *J. Org. Chem.* - 1959. - 24. - 1847–1854 : Vol. 12.
- BROADBENT H. S., SLAUGH H. and JARVIS N. L.** Rhenium Sulfides as Liquid-Phase Hydrogenation Catalysts. A Comparison with Molybdenum Sulfide and Cobalt Polysulfide [Article] // *J. Amer. Chem. Soc.* - 1954. - 6. - pp. 1519-1523 : Vol. 76.
- CAVANI F., TRIFIRÒ F. and VACCARI A.** Hydrotalcite-type anionic clays: Preparation, properties and applications [Article] // *Catalysis Today*. - 1991. - 2. - 173-301 : Vol. 11.
- CAVENTOU E.** [Article] // *Annalen der Chemie und Pharmacie*. - 1863. - 93. - Vol. 127.
- CESPI D.** [*et al.*] Butadiene from biomass, a life cycle perspective to address sustainability in the chemical industry [Article] // *Green Chem.* - 2016. - 1625-1638 : Vol. 18.
- CHAKRABORTY S.** [*et al.*] Highly Selective Formation of n-Butanol from Ethanol through the Guerbet Process: A Tandem Catalytic Approach [Article] // *J. Am. Chem. Soc.* - 2015. - 14264-14267 : Vol. 137.
- CHANKLANGA S.** [*et al.*] Hydrogenolysis of Glycerol to 1,3-Propanediol Over H-ZSM-5-Supported Iridium and Rhenium Oxide Catalysts [Article] // *Catalysis Today*. - 2021.
- CHEN C** [*et al.*] Synthesis and characterisation of aqueous miscible organic-layered double hydroxides [Article] // *Journal of Materials Chemistry A*. - 2014. - 36. - pp. 15102–15110.
- CHEN G.** [*et al.*] Catalytic dehydration of bioethanol to ethylene over TiO₂/Al₂O₃ catalysts in microchannel reactors [Article] // *Catalysis Today*. - 2007. - 1. - 111-119 : Vol. 125.

CHEN Y., WU S. and HO J. The role of Ru atoms toward the dehydrogenation of ethanol on Ru/ZrO₂(1 1 1) surface [Article] // Chemical Physics Letters. - 2011. - 501. - 315-318 : Vols. 4-6.

CHENG F-L [et al.] Guerbet reaction of methanol and ethanol catalyzed by CuMgAlO_x mixed oxides: Effect of M²⁺/Al³⁺ ratio [Article] // Journal of Fuel Chemistry and Technology. - 2018. - 12. - pp. 1472-1481 : Vol. 46.

CHIA M. [et al.] Selective Hydrogenolysis of Polyols and Cyclic Ethers over Bifunctional Surface Sites on Rhodium–Rhenium Catalysts [Article] // J. Am. Chem. Soc.. - 2011. - 133. - 12675–12689 : Vol. 32.

CHIEREGATO A. and OCHOA J.V., BANDINELLI, C., et al. On the chemistry of ethanol on basic oxides: Revising mechanisms and intermediates in the lebedev and guerbet reactions [Article] // ChemSusChem. - 2014. - 2. - pp. 1-13 : Vol. 8.

CHRISTIANSEN MA, MPOURMPAKIS G and VLACHOS DG Density Functional Theory-Computed Mechanisms of Ethylene and Diethyl Ether Formation from Ethanol on γ -Al₂O₃(100) [Article] // ACS Catal.. - 2013. - 3. - 1965–1975 : Vol. 9.

CIMINO S., LISI L. and ROMANUCCI S. Catalysts for conversion of ethanol to butanol: Effect of acid-base and redox properties [Article] // Catalysis Today. - 2018. - 304. - 58-63.

CLEWS R. J. Fundamentals of the Petroleum Industry [Book Section] // Project Finance for the International Petroleum Industry. - [s.l.] : Academic Press, 2016.

COOPER G. The Truth About Ethanol and Carbon Emissions [Online] // Renewable Fuels Association. - Renewable Fuels Association, 10 2022. - 05 2023. - <https://ethanolrfa.org/media-and-news/category/blog/article/2022/10/the-truth-about-ethanol-and-carbon-emissions>.

CORSON B. B. [et al.] Butadiene from Ethyl Alcohol. Catalysis in the One-and Two-Stop Processes [Article] // Ind. Eng. Chem.. - 1950. - pp. 359-373 : Vol. 42.

CORSON BB [et al.] Butadiene from ethyl alcohol - Catalysis in the one- and two-step processes [Article] // Ind. Eng. Chem. . - 1950. - pp. 359-373 : Vol. 42.

CRABBE E. [et al.] Biodiesel production from crude palm oil and evaluation of butanol extraction and fuel properties [Article] // Process Biochem. - 2001. - pp. 65-71 : Vol. 37.

CUELLO-PENALOZA PA [et al.] Ethanol to distillate-range molecules using Cu/Mg_xAlO_y catalysts with low Cu loadings [Article] // Applied Catalysis B: Environmental. - 2022. - 120984 : Vol. 304.

DA ROS S. [et al.] Ethanol do 1,3-Butadiene Conversion by using ZrZn-Containing MgO/SiO₂ Systems Prepared by Co-precipitation and Effect of Catalyst Acidity Modification [Article] // ChemCatChem. - 2016. - 8. - 2376–2386.

DAGLE VL [et al.] Effect of the SiO₂ support on the catalytic performance of Ag/ZrO₂/SiO₂ catalysts for the single-bed production of butadiene from ethanol [Article] // Applied Catalysis B: Environmental. - 2018. - pp. 576-587 : Vol. 236.

DAL SANTO V. [et al.] Bimetallic heterogeneous catalysts for hydrogen production [Article] // Catalysis Today. - 2012. - 1. - 190-205 : Vol. 197.

DERAZ N.M. The comparative jurisprudence of catalysts preparation methods: I. precipitation and impregnation methods [Article] // J Ind Environ Chem. - 2018. - pp. 19-21.

- DI COSIMO J. I. [et al.]** Structural Requirements and Reaction Pathways in Condensation Reactions of Alcohols on Mg₂AlO₄ Catalysts [Article] // Journal of Catalysis. - 2000. - 190. - 261–275.
- DI COSIMO J. I. [et al.]** Structure and surface and catalytic properties of Mg-Al basic oxides [Article] // J Catal. - 1998. - pp. 499-510 : Vol. 178.
- DI COSIMO J. L. [et al.]** Structure and surface catalytic properties of Mg-Al basic oxides [Article] // Journal of Catalysis. - 1998. - 2. - pp. 499-510 : Vol. 178.
- DIBENEDETTO T. A. and JONES W. D.** Upgrading of Ethanol to n-Butanol via a Ruthenium Catalyst in Aqueous Solution [Article] // Organometallics. - 2021. - 12. - pp. 1884-1888 : Vol. 40.
- DOMÉNECH P. [et al.]** Catalytic production of long-chain hydrocarbons suitable for jet-fuel use from fermentation-derived oxygenates [Article] // Green Chemistry. - 2022. - 9. - 3461-3474 : Vol. 24.
- DOWSON G. R. M. [et al.]** Catalytic Conversion of Ethanol into an Advanced Biofuel: Unprecedented Selectivity for n-Butanol [Article] // Angew. Chem. Int. Ed.. - 2013. - 34. - pp. 9005-9008 : Vol. 52.
- DÜRREN P.** Biobutanol: An attractive biofuel [Article] // Biotechnology Journal. - 2007. - 2. - pp. 1525–1534 : Vol. 12.
- EMIROĞLU A. O. and ŞEN M.** Combustion, performance and emission characteristics of various alcohol blends in a single cylinder diesel engine [Article] // Fuel. - 2018. - 15. - 34-40 : Vol. 212.
- ETEnergyWorld** National Hydrogen Mission: Leapfrogging towards India's cleaner future [Online] // Energy World. - 02 16, 2021. - 07 02, 2022. - <https://energy.economictimes.indiatimes.com/news/renewable/national-hydrogen-mission-leapfrogging-towards-indias-cleaner-future/80991679>.
- EWAN B. C. R. and ALLEN R. W. K.** A figure of merit assessment of the routes to hydrogen [Article] // International Journal of Hydrogen Energy. - 2005. - 8. - 809-819 : Vol. 30.
- EZINKWO G.O. [et al.]** Fundamental issues of catalytic conversion of bio-ethanol into butadiene [Article] // CHemBioEng. - 2014. - 1. - pp. 194-203 : Vol. 5.
- FAN D, DAI D-J and WU H-S** Ethylene Formation by Catalytic Dehydration of Ethanol with Industrial Considerations [Article] // Materials (Basel). - 2013. - pp. 101-115 : Vol. 6.
- FAN D. [et al.]** A DFT study on the aldol condensation reaction on MgO in the process of ethanol to 1,3-butadiene: understanding the structure–activity relationship [Article] // Phys. Chem. Chem. Phys.. - 2017. - pp. 25671-25682 : Vol. 19.
- FARMER T. J. and MASCAL M** Platform Molecules [Book Section] // Introduction to Chemicals from Biomass. - 2014.
- FIGUEREDO A. L. [et al.]** Process Optimization for a Sustainable and Selective Conversion of Fumaric Acid into γ -Butyrolactone Over Pd-Re/SiO₂ [Article] // Catalysis Letters. - 2021. - 6. - 1821-1833 : Vol. 151.
- FU S. [et al.]** Manganese-Catalyzed Upgrading of Ethanol into 1-Butanol [Article] // J. AM. Chem. Soc. - 2017. - 34. - pp. 11941-11948 : Vol. 139.

- GALLO J. M. R., BUENO J. M. C. and SCHUCHARDT J.** Catalytic Transformations of Ethanol for Biorefineries [Article] // J. Braz. Chem. Soc.. - 2014. - 12. - 2229-2243 : Vol. 25.
- GAO M. [et al.]** Study on the Mechanism of Butadiene Formation from Ethanol [Article] // Catalysis Letters. - 2014. - 144. - 2071–2079.
- GARBARINO G. [et al.]** A study of ethanol dehydrogenation to acetaldehyde over copper/zinc aluminate catalysts [Article] // Catalysis Today. - 2020. - 167-175 : Vol. 354.
- GARCÍA V. [et al.]** Challenges in biobutanol production: How to improve the efficiency? [Article] // Renewable and Sustainable Energy Reviews. - 2011. - 2. - pp. 964-980 : Vol. 15.
- GENNEQUIN C. [et al.]** Use and observation of the hydrotalcite "memory effect" for VOC oxidation [Article] // Catalysis Today. - 2010. - 1. - 191-197 : Vol. 157.
- GONZÁLEZ G. M. C.** Experimental study and reaction kinetics of 1,3-butadiene synthesis from bioethanol over an Hf-Zn/SiO₂ catalyst [Book]. - Sevilla : Universidad de Sevilla - Escuela Técnica Superior de Ingeniería, 2020.
- GORIN Y. A. and DANILINA M. I.** [Article] // J. Gen. Chem.. - 1948. - pp. 1069-1075 : Vol. 18.
- GOTHE M. L. [et al.]** Rhenium – A Tuneable Player in Tailored Hydrogenation Catalysis [Article] // Eur. J. Inorg. Chem.. - 2021. - 4043-4065.
- GRUB J. and LOSER E.** Butadiene in Ullmann's Encyclopedia of Industrial Chemistry [Book]. - Weinheim : Wiley-VHC, 2012.
- GUO J. [et al.]** Dehydrogenation and aromatization of propane over rhenium-modified HZSM-5 catalyst [Article] // Journal of Molecular Catalysis A: Chemical. - 2005. - 239. - 222-227.
- HAAGEN-SMIT A. and FOX M.** Ozone Formation in Photochemical Oxidation of Organic Substances [Article] // Industrial Chemical and Engineering Research. - 1956. - pp. 1484-1487 : Vol. 48.
- HAÁZ E. [et al.]** Platform Molecule Removal from Aqueous Mixture with Organophilic Pervaporation: Experiments and Modelling [Article] // Periodica Polytechnica Chemical Engineering. - 2019. - 1. - pp. 138-146 : Vol. 63.
- HAMMER B. and NØRSKOV J. K.** Theoretical surface science and catalysis—calculations and concepts [Article] // Adv. Catal.. - 2000. - pp. 71-129 : Vol. 45.
- HAN S. J. [et al.]** Hydrogen production by steam reforming of ethanol over mesoporous Ni–Al₂O₃–ZrO₂ xerogel catalysts: Effect of Zr/Al molar ratio [Article] // International Journal of Hydrogen Energy. - 2013. - 3. - 1376-1383 : Vol. 38.
- HANSEN A. C., ZHANG Q. and LYNE P. W. L.** Ethanol–diesel fuel blends — a review [Article] // Bioresource Technology. - 2005. - 3. - pp. 277-285 : Vol. 96.
- HANSPAL S. [et al.]** Multiproduct steady-state isotopic transient kinetic analysis of the ethanol coupling reaction over hydroxyapatite and magnesia [Article] // ACS Catalysis. - 2015. - pp. 1737-1746 : Vol. 5.
- HARVEY B. G., MERRIMAN W. W. and QUINTANA R. L.** Renewable Gasoline, Solvents, and Fuel Additives from 2,3-Butanediol [Article] // ChemSusChem. - 2016. - 14. - 1814-1819 : Vol. 9.

- HATTORI HIDESHI** Heterogeneous Basic Catalysis [Article] // Chem. Rev.. - [s.l.] : Chem. Rev., 1995. - 95. - 537–558 : Vol. 3. - 537–558.
- HAYASHI Y.** [*et al.*] Experimental and computational studies of the roles of MgO and Zn in talc for the selective formation of 1,3-butadiene in the conversion of ethanol [Article] // Phys. Chem. Chem. Phys.. - 2016. - 36. - 25191–25209.
- HE R.** [*et al.*] Interaction of Ethanol with MgO-SiO₂ Catalysts Studied by TPD Techniques [Article] // Chemistry Letters. - 2018. - 47. - 1097-1100 : Vol. 9.
- HEINZ J. B. and TEX L.** Process for the Production of Ceopentyl Glycol [Patent] : 3920760. - U.S., 1975.
- HO C. R., SHYLES S. and BELL A. T.** Mechanism and Kinetics of Ethanol Coupling to Butanol over Hydroxyapatite [Article] // ACS Catalysis. - 2016. - pp. 939-948 : Vol. 6.
- IEA** The Future of Petrochemicals [Online] // IEA. - IEA, 10 2018. - 7 22, 2022. - <https://www.iea.org/reports/the-future-of-petrochemicals>.
- IEA** Trends and developments in electric vehicle markets [Report]. - Paris : Global EV Outlook 2021, 2021.
- IFPRI International Food Policy Research Institute** Global Trade and Environmental Impact Study of the EU Biofuels Mandate [Article] // ATLASS Consortium. - [s.l.] : ATLASS Consortium, 2010. - 1-125. - 1-125.
- IHS Markit** Butadiene: Chemical Economics Handbook [Book]. - Londres : [s.n.], 2021.
- Jornal do Comércio** Maior demanda impulsiona eteno verde da Braskem [Online] // Jornal do Comércio. - 06 02, 2022. - 06 27, 2022. - https://www.jornaldocomercio.com/_conteudo/especiais/meio_ambiente/2022/05/849368-maior-demanda-impulsiona-eteno-verde-da-braskem.html.
- KEMPER J.** Biomass and carbon dioxide capture and storage: A review [Article] // International Journal of Greenhouse Gas Control. - 2015. - 401-430 : Vol. 40.
- KIBBY C. L. and HALL W.** Dehydrogenation of alcohols and hydrogen transfer from alcohols to ketones over hydroxyapatite catalysts [Article] // J Catal.. - 1973. - pp. 65-73 : Vol. 31.
- KIKHTYANIN O.** [*et al.*] Influence of Mg–Al Mixed Oxide Compositions on Their Properties and Performance in Aldol Condensation [Article] // Industrial & Engineering Chemistry Research. - 2017. - 45. - 13411-13422 : Vol. 56.
- KING A. M.** [*et al.*] Rhenium Complexes Bearing Tridentate and Bidentate Phosphinoamine Ligands in the Production of Biofuel Alcohols via the Guerbet Reaction [Article] // Organometallics. - 2021. - 40. - 2844-2851 : Vol. 16.
- KITAYAMA Y., SATOH M. and KODAMA T.** Preparation of large surface area nickel magnesium silicate and its catalytic activity for conversion of ethanol into buta-1,3-diene [Article] // Catal. Lett.. - 1996. - pp. 95-97 : Vol. 36.
- KODA K.** [*et al.*] Guerbet Reaction of Ethanol to n-Butanol Catalyzed by Iridium Complexes [Article] // Chem. Lett.. - 2009. - pp. 838-839 : Vol. 38.

- KONDRATOWICZ T. [et al.]** Controlled silica core removal from SiO₂@MgAl core-shell system as a tool to prepare well-oriented and highly active catalysts [Article] // Applied Clay Science. - 2022. - 106365 : Vol. 216.
- KOZLOWSKI J. T. and DAVIS R. J.** Heterogeneous Catalysts for the Guerbet Coupling of Alcohols [Article] // ACS Catalysis. - 2013. - 7. - pp. 1588-1600 : Vol. 3.
- KOZLOWSKY J. T. and DAVIS R. J.** Heterogeneous Catalysts for the Guerbet Coupling of Alcohols [Article] // ACS Catalysis. - 2013. - 3. - pp. 1588-1600 : Vol. 7.
- KULKARNI N. V., BRENNESSEL W. W. and JONES W. D.** Catalytic Upgrading of Ethanol to n-Butanol via Manganese-Mediated Guerbet Reaction [Article] // ACS Catalysis. - 2018. - pp. 997-1002 : Vol. 8.
- KUMAR R. [et al.]** Silica-Supported Nanoscale Hydrotalcite-Derived Oxides for C₄ Chemicals from Ethanol Condensation [Article] // ACS Appl. Nano Mater.. - 2022. - 7885–7895 : Vol. 5.
- KUSTROWSKI P. [et al.]** Acidity and basicity of hydrotalcite derived mixed Mg–Al oxides studied by test reaction of MBOH conversion and temperature programmed desorption of NH₃ and CO₂ [Article] // Mater. Res. Bull.. - 2004. - 263–281 : Vol. 39.
- LARINA OV [et al.]** Design of Effective Catalysts Based on ZnLaZrSi Oxide Systems for Obtaining 1,3-Butadiene from Aqueous Ethanol [Article] // ACS Sustainable Chem. Eng.. - 2020. - 8. - pp. 16600-16611 : Vol. 44.
- LEBEDEV S. V.** British Patent [Patent] : 331,402. - 1929.
- LEOFANTI G. [et al.]** Surface area and pore texture of catalysts [Article] // Catal. Today. - 1998. - 207-219 : Vol. 41.
- LEÓN M, DÍAZ E and ORDÓÑEZ S** Ethanol catalytic condensation over Mg–Al mixed oxides derived from hydrotalcites [Article] // Catalysis Today. - 2011. - pp. 436-442 : Vol. 164.
- LI X. [et al.]** One-Pot Conversion of Lignin into Naphthenes Catalyzed by a Heterogeneous Rhenium Oxide-Modified Iridium Compound [Article] // ChemSusChem. - 2020. - 17. - 4409-4419 : Vol. 13.
- LISBOA C. C. [et al.]** Bioethanol production from sugarcane and emissions of greenhouse gases – known and unknowns [Article] // GCB Bioenergy. - 2011. - 277–292 : Vol. 3.
- LIU S. [et al.]** Selective Hydrodeoxygenation of Vegetable Oils and Waste Cooking Oils to Green Diesel Using a Silica-Supported Ir–ReO_x Bimetallic Catalyst [Article] // ChemSusChem. - 2018. - 9. - 1446-1454 : Vol. 11.
- LIVINGSTONE S.** The Chemistry of Ruthenium, Rhodium, Palladium, Osmium, Iridium and Platinum [Book]. - 1973.
- LU Y. [et al.]** CO₂ photoelectroreduction with enhanced ethanol selectivity by high valence rhenium-doped copper oxide composite catalysts [Article] // Journal of Colloid and Interface Science. - 2021. - pp. 497-506 : Vol. 599.
- LUO W. [et al.]** The influence of impregnation sequence on glycerol hydrogenolysis over iridium-rhenium catalyst [Article] // React. Kinet. Mech. Catal.. - 2016. - 118. - 481–496.
- MADERUELO-SOLERA R. [et al.]** Tailoring basic and acidic properties of MgAl hydrotalcite by fluoride anions: Effect on glycerol oligomerisation [Article] // Catalysis Today. - 2023. - 114197 : Vol. 421.

- MAKSHINA E. V. [et al.]** Catalytic study of the conversion of ethanol into 1,3-butadiene [Article] // Catal. Today. - 2012. - pp. 338-344 : Vol. 198.
- MAKSHINA E. V. [et al.]** Review of old chemistry and new catalytic advances in the on-purpose synthesis of butadiene [Article] // Chem. Soc. Rev.. - 2014. - pp. 7917-7953 : Vol. 43.
- MARCU I-C [et al.]** Catalytic valorization of bioethanol over Cu-Mg-Al mixed oxide catalysts [Article] // Catalysis Today. - 2009. - 3-4. - pp. 231-238 : Vol. 147.
- MarketsandMarkets** Electric Vehicle Market by Component, Vehicle (Passenger Cars, CV), Propulsion (BEV, PHEV, FCEV), Vehicle Drive Type (FWD, RWD, AWD), Vehicle Top Speed (<125 mph, >125 mph), Charging Point, Vehicle Class, V2G, Region-Global Forecast 2030 [Report]. - 2021.
- MASIH D [et al.]** Catalytic dehydration of ethanol-to-ethylene over Rho zeolite under mild reaction conditions [Article] // Microporous and Mesoporous Materials. - 2019. - pp. 91-99 : Vol. 282.
- MEI J. [et al.]** Synthesis of Al₂O₃ with tunable pore size for efficient formaldehyde oxidation degradation performance [Article] // Journal of Materials Science. - 2018. - 3375–3387 : Vol. 53.
- MELLO F. F. C. [et al.]** Payback time for soil carbon and sugar-cane ethanol [Article] // Nature Climate Change. - 2014. - 4. - 605-609.
- MENDIBURU A. Z. [et al.]** Ethanol as a renewable biofuel: Combustion characteristics and application in engines [Article] // Energy. - 2022. - 124688 : Vol. 257.
- Michelin** Michelin, IFP Energies nouvelles, and Axens give a new dimension to the BioButterfly project [Online] // Michelin. - Michelin, 9 26, 2019. - 7 22, 2022. - <https://www.michelin.com/en/press-releases/michelin-ifp-energies-nouvelles-and-axens-give-a-new-dimension-to-the-biobutterfly-project/>.
- MILLENSIFER T. A.** Rhenium and Rhenium Compounds [Book]. - [s.l.] : John Wiley & Sons, Inc, 2010.
- MIYAKE N, BREZICKI G and DAVIS RJ** Cascade Reaction of Ethanol to Butadiene over Multifunctional Silica-Supported Ag and ZrO₂ Catalysts [Article] // : ACS Sustainable Chem. Eng.. - 2022. - pp. 1020-1035 : Vol. 10.
- MIYAMOTO M. [et al.]** Influence of the pre-reformer in steam reforming of dodecane using a Pd alloy membrane reactor [Article] // International Journal of Hydrogen Energy. - 2011. - 13. - 7771-7775 : Vol. 36.
- MME - Ministério de Minas e Energia** Nota Explicativa sobre a Proposta de Criação da Política Nacional de Biocombustíveis [Online] // MME - Ministério de Minas e Energia. - MME - Ministério de Minas e Energia, 2017. - 05 2023. - <https://www.gov.br/mme/pt-br/assuntos/secretarias/petroleo-gas-natural-e-biocombustiveis/renovabio-1/legislacao-e-documentos/concepcao-do-renovabio/renovabionotaexplicativa.pdf>.
- MORTON M.** History of Synthetic Rubber [Article] // Journal of Macromolecular Science: Part A - Chemistry. - 2006. - 7. - 1289-1302 : Vol. 15.
- MÜCK J. [et al.]** Transition metals promoting Mg-Al mixed oxides for conversion of ethanol to butanol and other valuable products: Reaction pathways [Article] // Applied Catalysis A: General. - 2021. - 626. - 118380.

- MUDIYANSELAGE K. [et al.]** Reactions of ethanol over CeO₂ and Ru/CeO₂ catalysts [Article] // Applied Catalysis B: Environmental. - 2016. - 197. - 198-205.
- NATTA G. and RIGAMONTI R.** Studio roentgenografico e chimico dei catalizzatori usati per la produzione del butadiene dall'alcool [Article] // Chim. Ind.. - 1947. - 239–243 : Vol. 29.
- NAVA J.** From crude oil refineries to biorefineries – From existing to new business models using hybrid approaches [Online] // BBA. - BBA, 11 08, 2021. - 05 2023. - <https://www.bba.ca/publications/from-crude-oil-refineries-to-biorefineries-from-existing-to-new-business-models-using-hybrid-approaches>.
- NDOU A. S., PLINT N. and COVILLE N. J.** Dimerisation of ethanol to butanol over solid-base catalysts [Article] // Appl. Catal.. - 2003. - pp. 337-345 : Vol. 251.
- NIELSEN M. [et al.]** Efficient Hydrogen Production from Alcohols under Mild Reaction Conditions [Article] // Angewandte Chemie. - 2011. - pp. 9767-9771 : Vol. 123.
- NIELSEN M. [et al.]** Towards a Green Process for Bulk-Scale Synthesis of Ethyl Acetate: Efficient Acceptorless Dehydrogenation of Ethanol [Article] // Angewandte Chemie. - 2012. - pp. 5711-5713 : Vol. 51.
- NIYAMA H., MORII S. and ECHIGOYA E.** Formation from ethanol over silica-magnesia catalysts [Article] // Bulletin of Chemical Society of Japan. - 1972. - 655-659 : Vol. 45.
- NISHIMURA S., TAKAGAKI A. and EBITANI K.** Characterization, synthesis and catalysis of hydrotalcite-related materials for highly efficient materials transformations [Article] // Green Chemistry. - 2013. - 2026-2042 : Vol. 15.
- OGO S. [et al.]** 1-Butanol synthesis from ethanol over strontium phosphate hydroxyapatite catalysts with various Sr/P ratios [Article] // J Catal. - 2012. - pp. 24-30 : Vol. 296.
- OGO S., ONDA A. and ANAGISAWA K.** Selective synthesis of 1-butanol from ethanol over strontium phosphate hydroxyapatite catalysts [Article] // Appl. Catal. A-General. - 2011. - pp. 188-195 : Vol. 402.
- OHNISHI R., AKIMOTO T. and TANABE K.** Pronounced catalytic activity and selectivity of MgO–SiO₂–Na₂O for synthesis of buta-1,3-diene from ethanol [Article] // Chem. Commun.. - 1985. - pp. 1613-1614 : Vol. 22.
- OLIVEIRA M. D.** Sugarcane and Ethanol Production and Carbon Dioxide Balances [Book Section] // Biofuels, Solar and Wind as Renewable Energy Systems. - [s.l.] : D. Pimentel, 2008.
- ORDÓÑEZ S [et al.]** Hydrotalcite-derived mixed oxides as catalysts for different C–C bond formation reactions from bioorganic materials [Article] // Catalysis Today. - 2011. - pp. 71-76 : Vol. 167.
- ORDÓÑEZ S. [et al.]** Hydrotalcite-derived mixed oxides as catalysts for different C-C bond formation reactions from bioorganic materials [Article] // Catal Today. - 2011. - pp. 71-76 : Vol. 167.
- OSTROMISLENSKY J.** [Article] // J. Russ. Phys. Chem. Soc.. - 1915. - pp.. 1472-1506 : Vol. 47.
- PACHECO H. P. [et al.]** Ru Promoted MgO and Al-Modified MgO for Ethanol Upgrading [Article] // Topics in Catalysis. - 2019. - pp. 894-907 : Vol. 62.

- PACHECO H. P.** Investigation of the mechanism of ethanol upgrading on MgO-based catalysts [Report]. - Rio de Janeiro : Universidade Federal do Rio de Janeiro, 2019.
- PALMA V. [et al.]** CeO₂-supported Pt/Ni catalyst for the renewable and clean H₂ production via ethanol steam reforming [Article] // Applied Catalysis B: Environmental. - 2014. - 145. - 73-84.
- PALWE, S.** Electric Vehicle Market Research Report Information [Online] // Market Research Future. - Market Research Future, 10 2020. - 6 2023. - https://www.marketresearchfuture.com/reports/electric-vehicles-market-1793?utm_source=adwords&utm_medium=ppc&utm_campaign=competitors&utm_id=mixed+reprot&campaign=20188667444&content=659692648005&keyword=electric%20vehicle%20market&utm_term=electric%20veh.
- PAMPARARO . [et al.]** A study of ethanol dehydrogenation to acetaldehyde over supported copper catalysts: Catalytic activity, deactivation and regeneration [Article] // Applied Catalysis A, General. - 2020. - 117710 : Vol. 602.
- PANG J [et al.]** Upgrading ethanol to n-butanol over highly dispersed Ni–MgAlO catalysts [Article] // Journal of Catalysis. - 2016. - 344. - pp. 184-193.
- PANG J. [et al.]** Upgrading ethanol to n-butanol over highly dispersed Ni–MgAlO catalysts [Article] // J Catal. - 2016. - pp. 184-193 : Vol. 344.
- PANG J. F. [et al.]** Upgrading ethanol to n-butanol over highly dispersed Ni–MgAlO catalysts [Article] // J. Catal.. - 2016. - pp. 184-193 : Vol. 344.
- PEREIRA L. G. [et al.]** Comparison of biofuel life-cycle GHG emissions assessment tools: the case studies of ethanol produced from sugarcane, corn, and wheat [Article] // Renew Sustain Energy Rev. - 2019. - 110. - 1-12.
- PEREIRA L. G. [et al.]** Production of Butanol and Other High Valued Chemicals Using Ethanol as Feedstock Integrated to a First and Second Generation Sugarcane Distillery [Article] // Chemical Engineering Transactions. - 2014. - pp. 805-810 : Vol. 37.
- PEREIRA L.G. [et al.]** Investigation of uncertainties associated with the production of n-butanol through ethanol catalysis in sugarcane biorefineries [Article] // Bioresource Technology. - 2015. - pp. 242-250 : Vol. 190.
- PHUNG T. K. [et al.]** A study of commercial transition aluminas and of their catalytic activity in the dehydration of ethanol [Article] // Journal of Catalysis. - 2014. - 102-113 : Vol. 311.
- POLAMAZA G. [et al.]** Ethanol-to-Butadiene: The Reaction and its Catalyst [Article] // Cat al. Sci. Techn ol.. - 2020. - 4860-4911 : Vol. 10.
- Polaris Market Research** 1,3 Butadiene (BD) Market Share, Size, Trends, Industry Analysis Report, By Type (Extractive Distillation, and Oxidative Dehydrogenation); By Application; By Region; Segment Forecast, 2022 - 2030 [Online] // Polaris Market Research. - Polaris Market Research, 08 2022. - 05 2023. - <https://www.polarismarketresearch.com/industry-analysis/1-3-butadiene-market>.
- POMALAZA G. [et al.]** ZnTa-TUD-1 as an easily prepared, highly efficient catalyst for the selective conversion of ethanol to 1,3-butadiene [Article] // Green Chem. - 2018. - 20. - 3203-3209.

- POMALAZA G., CAPRON M. and DUMEIGNIL F.** . Improving the synthesis of Zn-Ta-TUD-1 for the Lebedev process using the Design of Experiments methodology [Article] // Appl. Catal.. - 2020. - Vol. 591.
- QUATTLEBAUM W. M., TOUSSAINT W. J. and DUNN J. T.** Deoxygenation of Certain Aldehydes and Ketones: Preparation of Butadiene and Styrene [Article] // J. Am. Chem. Soc.. - 1947. - pp. 593-599 : Vol. 69.
- QUESADA J. [et al.]** Copper-Basic Sites Synergic Effect on the Ethanol Dehydrogenation and Condensation Reactions [Article] // ChemCatChem. - 2018. - 10. - 3583–3592.
- QUESADA J. [et al.]** Enhancement of the 1-butanol productivity in the ethanol condensation catalyzed by noble metal nanoparticles supported on Mg-Al mixed oxide [Article] // Applied Catalysis A: General. - 2018. - 563. - 64-72.
- RAMASAMY KK [et al.]** Role of Calcination Temperature on the Hydrotalcite Derived MgO–Al₂O₃ in Converting Ethanol to Butanol [Article] // Topics in Catalysis. - 2016. - pp. 46-54 : Vol. 59.
- RAYNAL L.** Our Solutions [Online] // IFP Energies Nouvelles. - IFP Energies Nouvelles, 2021. - 7 22, 2022. - <https://www.ifpenergiesnouvelles.com/innovation-and-industry/our-expertise/renewable-energies/bio-based-chemistry/our-solutions#BioButterfly>.
- REICHLER W. T., KANG S. Y. and EVERHARDT E. S.** The nature of the thermal decomposition of a catalytically active anionic clay mineral [Article] // Journal of Catalysis. - 1986. - 352-359 : Vol. 101.
- Renewable Fuels Association** 2023 Ethanol Industry Outlook [Online] // Renewable Fuels Association. - Renewable Fuels Association, 01 2023. - 05 2023. - <https://d35t1syewk4d42.cloudfront.net/file/2432/2023%20RFA%20Outlook%20FINAL.pdf>.
- RESTREPO-VALENCIA S. and WALTER A.** Techno-Economic Assessment of Bio-Energy with Carbon Capture and Storage Systems in a Typical Sugarcane Mill in Brazil [Article] // Energies. - 2019. - 1129 : Vol. 12.
- RIITTONEN T. [et al.]** One-Pot Liquid-Phase Catalytic Conversion of Ethanol to 1-Butanol over Aluminium Oxide—The Effect of the Active Metal on the Selectivity [Article] // Catalsts. - 2012. - pp. 68-84 : Vol. 2.
- RIITTONEN T.** Bio-Ethanol Valorization Towards C₄s Including 1-Butanol over Metal Modified Alumina and Zeolite Catalysts [Book]. - Åbo : Åbo Akademi University, 2014.
- RIITTONEN T., ETA, V., HYVÄRINEN, S., et al.** Engineering Aspects of Bioethanol Synthesis [Article] // Advances in Chemical Engineering - Chemical engineering for renewables conversion. - 2013. - 1. - pp. 1-73 : Vol. 42.
- RIOUX R. M. and VANNICE M. A.** Dehydrogenation of isopropyl alcohol on carbon-supported Pt and Cu–Pt catalysts [Article] // Journal of Catalysis. - 2005. - 1. - 147-165 : Vol. 233.
- RODGERS S. [et al.]** enewable butadiene: A case for hybrid processing via bio- and chemocatalysis [Article] // Journal of Cleaner Production. - 2022. - 132614 : Vol. 364.
- RYASHENTSEVA M. A. [et al.]** Hydrogenation Activity and Surface Composition of Perovskite-Type Mixed Rhenium Oxides [Article] // Journal of Catalysis. - 1990. - pp. 1-8 : Vol. 125.

- SCALBERT J. [et al.]** Ethanol condensation to butanol at high temperatures over a basic heterogeneous catalyst: How relevant is acetaldehyde self-aldolization? [Article] // *J Catal.* - 2014. - pp. 28-32 : Vol. 311.
- SELIGMAN R. B.** Production of Diacetone Alcohol [Patent] : 2879298. - U. S., 1957.
- SHANG Z [et al.]** Numerical research on effect of hydrogen blending fractions on idling performance of an n-butanol ignition engine with hydrogen direct injection [Article] // *Fuel.* - 2019. - 116082 : Vol. 258.
- SHEN J., TU M. and HU C.** Structural and Surface Acid/Base Properties of Hydrotalcite-Derived MgAlO Oxides Calcined at Varying Temperatures [Article] // *J. Solid State Chem.* - 1998. - 295-301 : Vol. 137.
- SHIMIZU K. [et al.]** Oxidant-Free Dehydrogenation of Alcohols Heterogeneously Catalyzed by Cooperation of Silver Clusters and Acid-Base Sites on Alumina [Article] // *Chem. Eur. J.* - 2009. - 2341-2351 : Vol. 15.
- SHIMIZU K. [et al.]** Oxidant-Free Dehydrogenation of Alcohols Heterogeneously Catalyzed by Cooperation of Silver Clusters and Acid-Base Sites on Alumina [Article] // *Chem. Eur. J.* - 2009. - 15. - 2341-2351.
- SHTYKA O. [et al.]** Steam reforming of ethanol for hydrogen production: influence of catalyst composition (Ni/Al₂O₃, Ni/Al₂O₃-CeO₂, Ni/Al₂O₃-ZnO) and process conditions [Article] // *Reaction Kinetics, Mechanisms and Catalysis.* - 2021. - 132. - 907-919.
- SHYLESH S. [et al.]** From Sugars to Wheels: The Conversion of Ethanol to 1,3-Butadiene over Metal-Promoted Magnesia-Silicate Catalysts [Article] // *ChemSusChem.* - 2016. - 9. - 1462-1472 : Vol. 12.
- SILVA C. C. C. M. [et al.]** Biodiesel production from soybean oil and methanol using hydrotalcites as catalyst [Article] // *Fuel Processing Technology.* - 2010. - 2. - 205-210 : Vol. 91.
- SING K. S. W. [et al.]** Reporting physisorption data for gas/solid systems with special reference to the determination of surface area and porosity [Article] // *Pure & Appl. Chem.* - 1985. - 4. - 603-619 : Vol. 57.
- SOUZA E. F. [et al.]** Computational and Experimental Mechanistic Insights into the Ethanol-to-Butanol Upgrading Reaction over MgO [Article] // *ACS Catalysis.* - 2020. - pp. 15162-15177 : Vol. 10.
- SUN H. N. and WRISTERS J. P.** Kirk-Othmer Encyclopedia of Chemical [Article] // Wiley-Interscience. - 2004. - 5. - pp. 365-392 : Vol. 4.
- SUN J. and WANG Y.** Recent Advances in Catalytic Conversion of Ethanol to Chemicals [Article] // *ACS Catalysis.* - 2014. - 4. - pp. 1078-1090 : Vol. 4.
- SUSHKEVICH V. L. [et al.]** Design of a metal-promoted oxide catalyst for the selective synthesis of butadiene from ethanol [Article] // *ChemSusChem.* - 2014. - 9. - 2527-2536 : Vol. 7.
- SUSHKEVICH V. L. and IVANOVA I.** Mechanistic study of ethanol conversion into butadiene over silver promoted zirconia catalysts [Article]. - 2017. - 36-49 : Vol. 215.

- SUSHKEVICH V. L., IVANOVA I. I. and TAARNING E.** Mechanistic Study of Ethanol Dehydrogenation over Silica-Supported Silver [Article] // ChemCatChem. - 2013. - 8. - 2367-2373 : Vol. 5.
- SUSHKEVICH VL [et al.]** Design of a metal-promoted oxide catalyst for the selective synthesis of butadiene from ethanol [Article] // ChemSusChem. - 2014. - pp. 2527-2536 : Vol. 7.
- TAHIR M. [et al.]** Thermodynamic and experimental analysis on ethanol steam reforming for hydrogen production over Ni-modified TiO₂/MMT nanoclay catalyst [Article] // Energy Conversion and Management. - 2017. - 25-37 : Vol. 154.
- TAIFAN W. E., BUCKO T. and BALTRUSAITIS J.** Catalytic conversion of ethanol to 1,3-butadiene on MgO: A comprehensive mechanism elucidation using DFT calculations [Article] // Journal of Catalysis. - 2017. - 78-91 : Vol. 346.
- TAIFAN W. E., YAN G. X. and BALTRUSAITIS J.** Surface chemistry of MgO/SiO₂ catalysts during the ethanol catalytic conversion to 1,3-butadiene: in situ DRIFTS and DFT study [Article] // Catalysis Science & Technology. - 2017. - 7. - 4648-4668 : Vol. 20.
- TAKAHARA I [et al.]** Dehydration of Ethanol into Ethylene over Solid Acid Catalysts [Article] // Catalysis Letters volume. - 2005. - 105. - pp. 249-252.
- TAMURA H. [et al.]** Formation of hydrotalcite in aqueous solutions and intercalation of ATP by anion exchange [Article] // Journal of Colloid and Interface Science. - 2006. - 300. - 648-654 : Vol. 2.
- TANAKA Y. and UTSUNOMIYA M.** [Patent] : 20100298613A1. - U. S., 2010.
- Technology Lummus** Lummus and Synthos Advance Bio-Butadiene Technology Development to Produce Sustainable Rubber [Online] // PR News Wire. - Cision, 29, 2022. - 7 5, 2022. - <https://www.prnewswire.com/news-releases/lummus-and-synthos-advance-bio-butadiene-technology-development-to-produce-sustainable-rubber-301478286.html>.
- TIAN P. [et al.]** Methanol to Olefins (MTO): From Fundamentals to Commercialization [Article] // ACS Catal.. - 2015. - 3. - 1922-1938 : Vol. 5.
- TICHIT D. [et al.]** The aldol condensation of acetaldehyde and heptanal on hydrotalcite-type catalysts [Article] // J Catal. - 2003. - pp. 167-175 : Vol. 219.
- TICHIT D. and COQ B.** Catalysis by hydrotalcites and related materials [Article] // Cattech. - 2003. - 6. - 206-217 : Vol. 7.
- TOMISHIGUE K., NAKAGAWA Y. and TAMURA M.** Taming heterogeneous rhenium catalysis for the production of biomass-derived chemicals [Article] // Chinese Chemical Letters. - 2020. - 5. - pp. 1071-1077 : Vol. 31.
- TOUSSAINT W. J., DUNN J. T. and JACKSON D. R.** Production of Butadiene from Alcohol [Article] // Ind. Eng. Chem.. - 1947. - pp. 120-125 : Vol. 39.
- TSUCHIDA T. [et al.]** Reaction of ethanol over hydroxyapatite affected by Ca/P ratio of catalyst [Article] // J. Catal.. - 2008. - pp. 183-189 : Vol. 259.
- TSUCHIDA T., KUBO, J., YOSHIOKA, T., et al.** Reaction of ethanol over hydroxyapatite affected by Ca/P ratio of catalyst [Article] // Journal of Catalysis. - 2008. - 2. - pp. 183-189 : Vol. 259.

- TUR M. V., ANISOMOVA S. B. and PLATANOV M. S.** Obs. Chim [Book]. - 1937. - 2895.
- U.S. Energy Information Administration** Monthly Energy Review [Online] // U.S. Energy Information Administration (EIA). - Independent Statistics and Analysis, 12 2024. - 12 2024. - <https://www.eia.gov/totalenergy/data/monthly/pdf/mer.pdf>.
- US Research Nanomaterials, Inc** Alumina Nanoparticles [Online] // US Research Nanomaterials, Inc. - US Research Nanomaterials, Inc. - 6 2023. - <https://www.us-nano.com/inc/sdetail/13136>.
- VALTER M. [et al.]** Electrooxidation of Glycerol on Gold in Acidic Medium: A Combined Experimental and DFT Study [Article] // J. Phys. Chem.. - 2018. - 19. - pp. 10489-10494 : Vol. 122.
- VARGHESE J. J. [et al.]** Synergistic Contribution of the Acidic Metal Oxide–Metal Couple and Solvent Environment in the Selective Hydrogenolysis of Glycerol: A Combined Experimental and Computational Study Using ReOx–Ir as the Catalyst [Article] // ACS Catal.. - 2019. - 9. - 485–503 : Vol. 1.
- VIEIRA J. L. [et al.]** MgO/SiO₂ prepared by wet-kneading as a catalyst for ethanol conversion to 1,3-butadiene: Prins condensation as the predominant mechanism [Article] // Molecular Catalysis. - 2022. - 112718 : Vol. 532.
- VSHWANATHAN V. [et al.]** Alkylation of catechol with methanol to guaiacol over sulphate-modified zirconia solid acid catalysts [Article] // Reaction Kinetics and Catalysis Letters . - 2007. - 311-317 : Vol. 92.
- WANG C. [et al.]** Low-Temperature Dehydrogenation of Ethanol on Atomically Dispersed Gold Supported on ZnZrOx [Article] // ACS Catal.. - 2016. - 6. - 210–218 : Vol. 1.
- WANG K [et al.]** Hierarchical nano-sized ZnZr-Silicalite-1 multifunctional catalyst for selective conversion of ethanol to butadiene [Article] // Applied Catalysis B: Environmental. - 2022. - 120822 : Vol. 301.
- WANG Q. [et al.]** Morphology and composition controllable synthesis of Mg–Al–CO₃ hydrotalcites by tuning the synthesis pH and the CO₂ capture capacity [Article] // Applied Clay Science. - 2012. - 18-26 : Vol. 55.
- WANG T. [et al.]** Preparation of Highly Active Monometallic Rhenium Catalysts for Selective Synthesis of 1,4-Butanediol from 1,4-Anhydroerythritol [Article] // ChemSusChem. - 2019. - 12. - 3615-3626 : Vol. 15.
- WANG X [et al.]** The influence of zinc loadings on the selectivity control of bio-ethanol transformation over MgO-SiO₂ catalysts [Article] // Applied Catalysis A, General. - 2020. - 117565 : Vol. 598.
- WANG X. [et al.]** The influence of zinc loadings on the selectivity control of bio-ethanol transformation over MgO-SiO₂ catalysts [Article] // Applied Catalysis A, General. - 2020. - 586. - 117565.
- WANG Z. [et al.]** Active and stable Cu doped NiMgAlO catalysts for upgrading ethanol to n-butanol [Article] // Journal of Energy Chemistry. - 2022. - 306-317 : Vol. 72.
- WEI H. [et al.]** Renewable bio-jet fuel production for aviation: A review [Article] // Fuel. - 2019. - 15. - 115599 : Vol. 254.

- WHITE W. C.** Butadiene production process overview [Article] // *Chemico-Biological Interactions*. - 2007. - 1-3. - pp. 10-14 : Vol. 166.
- XU G. Q. [et al.]** Direct self-condensation of bio-alcohols in the aqueous phase [Article] // *Green Chem.* - 2014. - pp. 3971-3977 : Vol. 16.
- YAN T. [et al.]** Mechanistic Insights into One-Step Catalytic Conversion of Ethanol to Butadiene over Bifunctional Zn–Y/Beta Zeolite [Article] // *ACS Catal.* - 2018. - 8. - 2760–2773 : Vol. 4.
- YANG C. and MENG Z. Y.** Bimolecular Condensation of Ethanol to 1-Butanol Catalyzed by Alkali Cation Zeolites [Article] // *J Catal.* - 1993. - pp. 37-44 : Vol. 142.
- YOUNG Z. D. and DAVIS R. J.** Hydrogen Transfer Reactions Relevant to Guerbet Coupling of Alcohols over Hydroxyapatite and Magnesium Oxide Catalysts [Article] // *Catalysis Science & Technology*. - 2018. - pp. 1722-1729 : Vol. 8.
- YOUNG Z. D., HANSPAL S. and DAVID R. J.** Aldol condensation of acetaldehyde over titania, hydroxyapatite, and magnesia [Article] // *ACS Catalysis*. - 2016. - pp. 3193-3202 : Vol. 6.
- YU D. [et al.]** Stabilizing copper species using zeolite for ethanol catalytic dehydrogenation to acetaldehyde [Article] // *Chinese Journal of Catalysis*. - 2019. - 1375-1384 : Vol. 40.
- YUAN B. [et al.]** Atomic Ru catalysis for ethanol coupling to C4+ alcohols [Article] // *Applied Catalysis B: Environmental*. - 2022. - 121271 : Vol. 309.
- ZANCANER A. and WRIGHT C.** *The Energy Series: The Brazilian Ethanol Market*. - [s.l.] : CZARNIKOW, 2020.
- ZHANG M. [et al.]** Study on key step of 1,3-butadiene formation from ethanol on MgO/SiO₂ [Article] // *RSC Adv*. - 2015. - pp. 25959-25966 : Vol. 5.
- ZHANG W., FAN D. and YU Y.** A DFT study of the aldol condensation reaction in the processing of ethanol to 1,3-butadiene on a MgO/SiO₂ surface [Article] // *New Journal of Chemistry*. - 2022. - 559-571 : Vol. 46.
- ZHANG Z [et al.]** Investigation on the combustion and emission characteristics of diesel engine fueled with diesel/methanol/n-butanol blends [Article] // *Fuel*. - 2022. - 314. - 123088.